Astronomy & Astrophysics manuscript no. toi175
July 13, 2021

A warm terrestrial planet with half the mass of Venus transiting a nearby star*

Olivier D. S. Demangeon[1,2†], M. R. Zapatero Osorio[10], Y. Alibert[6], S. C. C. Barros[1,2], V. Adibekyan[1,2], H. M. Tabernero[10,1], A. Antoniadis-Karnavas[1,2], J. D. Camacho[1,2], A. Suárez Mascareño[7,8], M. Oshagh[7,8], G. Micela[15], S. G. Sousa[1], C. Lovis[5], F. A. Pepe[5], R. Rebolo[7,8,9], S. Cristiani[11], N. C. Santos[1,2], R. Allart[19,5], C. Allende Prieto[7,8], D. Bossini[1], F. Bouchy[5], A. Cabral[3,4], M. Damasso[12], P. Di Marcantonio[11], V. D'Odorico[11,16], D. Ehrenreich[5], J. Faria[1,2], P. Figueira[17,1], R. Génova Santos[7,8], J. Haldemann[6], N. Hara[5], J. I. González Hernández[7,8], B. Lavie[5], J. Lillo-Box[10], G. Lo Curto[18], C. J. A. P. Martins[1], D. Mégevand[5], A. Mehner[17], P. Molaro[11,16], N. J. Nunes[3], E. Pallé[7,8], L. Pasquini[18], E. Poretti[13,14], A. Sozzetti[12], and S. Udry[5]

1 Instituto de Astrofísica e Ciências do Espaço, CAUP, Universidade do Porto, Rua das Estrelas, 4150-762, Porto, Portugal
2 Departamento de Física e Astronomia, Faculdade de Ciências, Universidade do Porto, Rua Campo Alegre, 4169-007, Porto, Portugal
3 Instituto de Astrofísica e Ciências do Espaço, Faculdade de Ciências da Universidade de Lisboa, Campo Grande, PT1749-016 Lisboa, Portugal
4 Departamento de Física da Faculdade de Ciências da Universidade de Lisboa, Edifício C8, 1749-016 Lisboa, Portugal
5 Observatoire de Genève, Université de Genève, Chemin Pegasi, 51, 1290 Sauverny, Switzerland
6 Physics Institute, University of Bern, Sidlerstrasse 5, 3012 Bern, Switzerland
7 Instituto de Astrofísica de Canarias (IAC), Calle Vía Láctea s/n, E-38205 La Laguna, Tenerife, Spain
8 Departamento de Astrofísica, Universidad de La Laguna (ULL), E-38206 La Laguna, Tenerife, Spain
9 Consejo Superior de Investigaciones Cientícas, Spain
10 Centro de Astrobiología (CSIC-INTA), Crta. Ajalvir km 4, E-28850 Torrejón de Ardoz, Madrid, Spain
11 INAF - Osservatorio Astronomico di Trieste, via G. B. Tiepolo 11, I-34143 Trieste, Italy
12 INAF - Osservatorio Astrofisico di Torino, via Osservatorio 20, 10025 Pino Torinese, Italy
13 Fundación G. Galilei – INAF (Telescopio Nazionale Galileo), Rambla J. A. Fernández Pérez 7, E-38712 Breña Baja, La Palma, Spain
14 INAF - Osservatorio Astronomico di Brera, Via E. Bianchi 46, I-23807 Merate, Italy
15 INAF - Osservatorio Astronomico di Palermo, Piazza del Parlamento 1, I-90134 Palermo, Italy
16 Institute for Fundamental Physics of the Universe, Via Beirut 2, I-34151 Miramare, Trieste, Italy
17 European Southern Observatory, Alonso de Córdova 3107, Vitacura, Región Metropolitana, Chile
18 European Southern Observatory, Karl-Schwarzschild-Strasse 2, 85748, Garching b. München, Germany
19 Department of Physics, and Institute for Research on Exoplanets, Université de Montréal, Montréal, H3T 1J4, Canada

Received date / Accepted date

ABSTRACT

In recent years, the advent of a new generation of radial velocity instruments has allowed us to detect lower and lower mass planets, breaking the one Earth-mass barrier. Here we report a new milestone in this context, by announcing the detection of the lightest planet measured so far using radial velocities: L 98-59 b, a rocky planet with half the mass of Venus which is part of a system composed of three known transiting terrestrial planets (planets b to d). We announce the discovery of a fourth non-transiting planet with a minimum mass of $3.06^{+0.33}_{-0.37}$ $M_\oplus$ and an orbital period of $12.796^{+0.020}_{-0.019}$ days and report hints for the presence of a fifth non-transiting terrestrial planet. If confirmed, with a minimum mass of $2.46^{+0.66}_{-0.82}$ $M_\oplus$ and an orbital period $23.15^{+0.60}_{-0.17}$ days, this planet would sit in the middle of the habitable zone of the L 98-59 system.

L 98-59 is a bright M-dwarf located 10.6 pc away. Positioned at the border of the continuous viewing zone of the James Webb space telescope, this system is destined to become a corner stone for comparative exoplanetology of terrestrial planets. The three transiting planets have transmission spectrum metrics ranging from 49 to 255 which undoubtedly make them prime targets for atmospheric characterization with the James Webb space telescope, the Hubble space telescope, Ariel or ground-based facilities like NIRPS or ESPRESSO. With equilibrium temperature ranging from 416 to 627 K, they offer a unique opportunity to study the diversity of warm terrestrial planets without the unknowns associated with different host stars.

L 98-59 b and c have densities of $3.6^{+1.4}_{-1.5}$ and $4.57^{+0.77}_{-0.85}$ g.cm^{-3} respectively and have very similar bulk compositions with a small iron core, representing only 12 to 14 % of the total mass, and a small amount of water. However, with a density of $2.95^{+0.79}_{-0.51}$ g.cm^{-3} and despite a similar core mass fraction, up to 30 % of L 98-59 d's mass could be made of water.

Key words. Planetary systems – Stars: individual: L 98-59 – Techniques: radial velocities, high precision photometry

1. Introduction

Over the last years, radial velocity (RV) instruments like HARPS (Mayor et al. 2003), HARPS-N (Cosentino et al. 2012) and more recently CARMENES (Quirrenbach et al. 2014) and ESPRESSO (Pepe et al. 2021) have demonstrated that it's now possible to detect planets with masses similar to the mass of the Earth using radial velocities (e.g. Astudillo-Defru et al. 2017a; Rice et al. 2019; Zechmeister et al. 2019; Suárez Mascareño et al. 2020). These results represent an important achievement in the quest for life outside the Solar system. However, it is important to keep pushing towards smaller masses and longer periods to ensure our capacity to measure the mass of a transiting Earth analog in the habitable zone of a bright host star.

The detection of biosignatures on an exoplanet depends on our capability to study its atmosphere which currently relies on transit spectroscopy (e.g. Kaltenegger 2017). Space-based transit surveys like Kepler/K2 (Borucki et al. 2010; Howell et al. 2014), TESS (Ricker et al. 2015) and even ground based surveys like TRAPPIST (Gillon et al. 2011) have revealed hundreds of transiting terrestrial planets (e.g. Batalha et al. 2013). However the community is yet to detect and study the atmosphere of one of them (Kreidberg et al. 2019). A large fraction of the known terrestrial planets are part of multi-planetary system (Lissauer et al. 2011). Multi-planetary systems are laboratories for a variety of studies: Planet-planet interactions (e.g. Barros et al. 2015), planetary formation and migration (e.g Rein 2012; Albrecht et al. 2013; Delisle 2017) and/or comparative planetology (e.g. Mandt et al. 2015; Millholland et al. 2017). The discovery and accurate characterisation of a system with multiple transiting terrestrial planets amenable to transit spectroscopy would thus represent a crucial milestone.

The L 98-59 system, alias TESS Object of Interest 175 (TOI-175) system, is a multi-planetary system announced by Kostov et al. (2019, hereafter K19) as composed of three transiting exoplanets with radii ranging from 0.8 to 1.6 Earth Radii ($R_\oplus$). The host star is a bright (magK = 7.1, Cutri et al. 2003, magV=11.7, Zacharias et al. 2012) nearby (10.6194 pc, Gaia Collaboration 2018; Bailer-Jones et al. 2018) M dwarf star (Gaidos et al. 2014). One interesting particularity of this system is its location, right ascension (RA) of 08:18:07.62 and declination (DEC) of -68:18:46.80, at the border of the continuous viewing zone ($\sim$ 200 days per year) of the James Webb space telescope (JWST, Gardner et al. 2006). This system is thus a prime target for comparative study of rocky planet atmospheres within the same system (Greene et al. 2016; Morley et al. 2017).

The HARPS spectrograph (Mayor et al. 2003) was used to carry out a RV campaign to measure the masses of these three planets (Cloutier et al. 2019, hereafter C19). The masses of the two outer planets were constrained to 2.36 ± 0.36 and 2.24 ± 0.53 Earth masses ($M_\oplus$), leading to bulk densities of 5.3 ± 1.2 and 3.2 ± 1.2 g.cm^{-3} for planet c and d respectively. C19 could not constrain the mass of the inner planet b and delivered an upper limit of 1.01 $M_\oplus$ (with a 95% confidence level). The PFS spectrograph (Crane et al. 2006, 2008, 2010) was also used to attempt the mass measurement of the three planets. With only 14 PFS measurements, Teske et al. (2020) derived masses of 1.32 ± 0.73, 1.24 ± 0.95 and 2.11 ± 0.72 $M_\oplus$ for planet b, c and d respectively. These mass estimates are non surprisingly less precise, but roughly compatible with C19's. Due to the low number and the lower precision of the PFS data, we do not include these measurements in our analysis.

We report here the results of a follow-up RV campaign with the ESPRESSO (Echelle SPectrograph for Rocky Exoplanets and Stable Spectroscopic Observations) spectrograph (Pepe et al. 2021) aimed at refining the mass of the planets in the L 98-59 system.

In Section 2, we present the RV and photometric data sets. In Section 3, we perform the characterization of the host star. We describe our analysis of the data sets in Section 4. Finally in Section 5 and 6, we discuss the particularities and the importance of this system.

2. The datasets

2.1. High-resolution spectroscopy

2.1.1. HARPS

C19 obtained 165 spectra with HARPS installed at the 3.6 telescope of the ESO La Silla Observatory (programmes 198.C-0838, 1102.C-0339, and 0102.C-0525) between October 17, 2018 (barycentric Julian date, BJD = 2458408.5) and April 28, 2019 (BJD = 2458601.5). HARPS is a fiber-fed cross-dispersed echelle spectrograph operating in a temperature and pressure regulated vacuum chamber. It covers wavelengths from 380 to 690 nm with an average spectral resolution of $R = 115\,000$. We obtained the RVs from C19 and refer the reader interested in the details of the observations and their processing to this publication. However, we warn the reader that in order to reproduce the results presented by C19, in particular the RV time series and its generalized Lomb-Scargle periodogram (GLSP, Zechmeister & Kürster 2009), we had to exclude 4 measurements obtained at 2 458 503.795048, 2 458 509.552019, 2 458 511.568314 and 2 458 512.581045 BJD. We identified these measurements with a 4-sigma iterative sigma clipping. These measurements were excluded from all the analyses in this paper. All measurements were obtained with fiber B pointed at the sky (no simultaneous observation of a calibration source). 140 measurements were obtained with an exposure time of 900 s resulting in an average signal-to-noise ratio (SNR) of 41 per resolution element at 650 nm. For the remaining 21 measurements, the exposure time varied from 500 to 1800 s, resulting in a median SNR of 49. The RVs were extracted from the spectra via template matching (Astudillo-Defru et al. 2017b). Their median precision (1 sigma uncertainty) is 2.08 m s^{-1}.

In addition to the RV measurements, C19 provide the measurement of several stellar activity indicators: the full width at half maximum (FWHM) of the cross-correlation function (CCF), the bisector span of the CCF (BIS), the depth of the H_α, H_β, H_γ lines, the depth of the sodium doublet *NaD* and the S-index based on the depth of the *Ca II H & K* doublet. All these indicators are sensitive to chromospheric or photospheric activity.

2.1.2. ESPRESSO

We obtained 66 spectra with ESPRESSO installed at the VLT telescopes of the ESO Paranal Observatory between November 14, 2018 (BJD = 2458436.5) and March 04, 2020 (BJD = 2458912.5) as part of the ESPRESSO Guaranteed Time Observation (programmes 1102.C-0744, 1102.C-0958, and 1104.C-0350). ESPRESSO (Pepe et al. 2021) is also a fibre-fed high-resolution echelle spectrograph operating in a temperature and

* Based in part on Guaranteed Time Observations collected at the European Southern Observatory under ESO programme(s) 1102.C-0744, 1102.C-0958, and 1104.C-0350 by the ESPRESSO Consortium.

† e-mail: olivier.demangeon@astro.up.pt

pressure regulated vacuum chamber. It covers wavelengths from 380 to 788 nm with an average spectral resolution of R = 140 000 in its single UT high-resolution mode (HR21, slow readout mode) used for these observations. All measurements were obtained with the sky on fiber B. All measurements were obtained with a 900 s exposure time resulting in an average SNR of 70 per resolution element at 650 nm. The RVs were extracted from the spectra using the version 2.2.1 of the ESPRESSO pipeline Data-Reduction Software (DRS)[1]. It computes the CCF of the sky-subtracted spectra with a stellar line mask to estimate the RV (Baranne et al. 1996). In this case, the mask is optimized for stars of spectral type M2 V. The CCF is then fitted with an inverted Gaussian model. The parameters of the profile are the continuum level, the center of the Gaussian profile, which provides the measurement of the RV, and its FWHM. Finally, the amplitude provides a measure of the contrast of the CCF. The uncertainties on the measured RVs are computed using the algorithms described in Bouchy et al. (2001) and reflect the photo-noise limited precision. The uncertainties on the FWHM are estimated as the double of RV uncertainties. From the 66 measurements, we discarded three measurements, obtained at 2 458 645.496, 2 458 924.639, 2 458 924.645 $\mathrm{BJD_{TDB}}$, due to their high RV uncertainties (identified through an iterative 4-sigma clipping). An inspection of the night reports indicates that these measurements were obtained under bad observing conditions: Strong wind, bad seeing and cirri and bright moon for the first measurement. The last measurement was even interrupted due to high winds. The median precision (1 sigma uncertainty) obtained on the ESPRESSO RVs is 0.8 $\mathrm{m\,s^{-1}}$ (a factor 2.6 better than the HARPS RVs).

In addition to the RV, FWHM and contrast measurements, we computed several activity indicators: the BIS (Queloz et al. 2001) , the depth of the H_α line, the sodium doublet (*NaD*, Díaz et al. 2007) and the S-index (Lovis et al. 2011; Noyes et al. 1984).

Around the middle of our RV campaign, in June 2019, the fiber-link of ESPRESSO was replaced. This resulted in an increased throughput, but requires us to consider an RV offset between the data taken before and after this intervention (Pepe et al. 2021).

2.2. High precision photometry with TESS

L 98-59 (TIC 307210830, TOI-175) was observed by TESS in short cadence (2 min) during 9 sectors (2, 5, 8, 9, 10, 11, 12, 28 and 29) with Camera 4 and 3. These observations correspond to $\sim$ 243 days of non-continous observations taken between August 22, 2018 (BJD = 2458352.5) and September 22, 2020 (BJD = 2459114.5). We downloaded the light-curves (LC) from the Mikulski Archive for Space Telescopes (MAST) using the python package `astroquery`. The LC data products provided by the TESS pipeline (Jenkins et al. 2016) provide two LCs, the simple aperture photometry SAP LC and the pre-search data conditioned simple aperture photometry PDCSAP LC (Smith et al. 2012; Stumpe et al. 2014). Contrary to the SAP LC, the PDCSAP LC is detrended using common basis vectors computed over all stars observed on the same CCD. For our analyses, we used exclusively the PDCSAP LC. From the LC, we removed the data points whose quality flags where showing the bits 1, 2, 3, 4, 5, 6, 8, 10, 12 following the example provided by the TESS team. Following a procedure inspired from K19, we detrended the LC from the residual stellar activity signal and instrument noise using a gaussian process (GP). We masked all the transits of the three planets using the ephemerides and transit durations provided by K19 and fitted the resulting LC with a GP model using the `celerite` Python package (Foreman-Mackey et al. 2017; Foreman-Mackey 2018) and a mean shift between sectors. The functional form of the kernel used was the one of a damped harmonic oscillator chosen for its flexibility and smooth variations allowing to model the unknown mixture of stellar activity and residual instrumental noise. Its equation is

$$S(\omega) = \sqrt{\frac{2}{\pi}} \frac{S_0\,\omega_0^4}{(\omega^2 - \omega_0^2)^2 + \omega^2\,\omega_0^2/Q^2}, \tag{1}$$

where Q, the quality factor, is fixed to $\frac{1}{\sqrt{2}}$, S_0 is the amplitude and ω_0 is the angular frequency corresponding to the break-point in the power spectral density of this kernel.

The fit was performed using an affine-invariant ensemble sampler for MCMC (Goodman & Weare 2010) implemented in the Python package `emcee` (Foreman-Mackey et al. 2013) which samples the *posterior* probability density function. We used a multi-dimensional Gaussian distribution for the likelihood. For the *prior*s, we used a uniform *prior* between -20 and 15 on $\ln S_0$ and we obtain a *posterior* providing an estimate of S_0 = $82.38^{+6.59}_{-5.77}$ ppm, using the median and the 68 % confidence interval. For ω_0, we used a uniform *prior* between -20 and 15 on $\ln\omega_0$ and we obtain an estimate of $\ln\omega_0 = 1.17^{+0.08}_{-0.09}$ (in $\ln \mathrm{day}^{-1}$). We did not attribute *prior*s to the offset between sectors and the retrieved values are compatible with the values provided in Table C.1. We used 32 walkers (for 11 free parameters) and performed a first run of 500 iterations as burn-in. The initial positions for this first run were drawn from the prior for S_0 and ω_0 and set to 0 for the offset between sectors. After this first run, we reset the `emcee` sampler and performed a second run of 2000 iterations which started from the last positions of the previous run. After this second run, we examined the histogram of the acceptance fraction of the chains to identify chains that had significantly lower acceptance fractions than the others. A lower acceptance fraction implies a stronger correlation between consecutive iterations which will increase the sampling error of the *posterior* PDF inferred from the histograms of the chains. We also examined the histogram of the logarithm of the *posterior* probability of the chain (estimated by the average of this value computed over the last 1 % of the iterations of each chains). The objective was to understand if all the chains have converged toward regions of the parameter space that have similar *posterior* probability density values. In this case both histograms are monomodal indicating that all chain have similar acceptance fraction and sample regions of the parameter space with similar *posterior* probability density values. We checked that all the chains were converged and converged to the same region of the parameter space using the Geweke criterion (Geweke 1992). All the chains indeed converged to the same region of the parameter space after the first 750 iterations of the second run. We further confirmed that the remaining parts of the chains were converged and long enough by computing the integrated auto-correlation time using the method implemented in `emcee` and checking that it was 10 times shorter than the remaining number of iterations.

Finally, we normalized the LC dividing it by the "best GP model", whose parameters values are the median values of the converged MCMC chains. Finally, we cut the LC to keep only data points within 1.5 transit durations on both sides of each mid-transit time. This reduced the number of data points and the computation time.

[1]A detailed description of the ESPRESSO DRS can be found in the ESPRESSO pipeline user manual available at espresso-pipe-recipes

3. Characterisation of the M-Dwarf L 98-59 A

According to K19, L 98-59 A is a M3V star. The derivation of accurate stellar properties through high-resolution spectroscopy for M stars is complicated due to the prevalence of blended lines which makes the derivation of individual lines properties and abundance ratios difficult. We thus applied several approaches to characterize L 98-59 A in order to assess and discuss the homogeneity and the accuracy of their outcomes. This analysis is presented in details in Appendix A and we summarize the results in this section.

3.1. Stellar atmospheric parameters

For the derivation of the stellar parameters, effective temperature ($T_{\rm eff}$), surface gravity (log g), and metallicity ([Fe/H]), we chose to fit the combined spectrum of L 98-59 A constructed using 61 ESPRESSO spectra (SNR = 1063 at 7580 Å) with the latest version of the spectral synthesis code SteParSyn (Tabernero et al. 2018; Tabernero et al. 2021, see Appendix A.1.1 for more details). We adopted the estimates provided by SteParSyn at the exception of the uncertainty on the $T_{\rm eff}$ that we identified as underestimated (see Appendix A.1). We enlarged this uncertainty to encompass the best values provided by the other methods within one sigma. The set of adopted estimates is provided in Table 3.

3.2. Stellar modeling: mass, radius and age

Thanks to the high precision and accuracy of Gaia parallactic distances (10.6194 ± 0.0032 pc inferred from the Gaia-DR2 parallax by Bailer-Jones et al. 2018) and the well sampled photometric spectral energy distribution (SED, see Appendix A.1.3), we can derive a reliable estimate of L 98-59 A's absolute bolometric luminosity: 0.01128 ± 0.00042 $L_\odot$. Added to our estimate of the $T_{\rm eff}$ (see Section 3.1, Appendix A.1 and Table 3), we infer the radius of L 98-59 A to be $0.303^{+0.026}_{-0.023}$ $R_\odot$ using the Stefan-Boltzmann law. This is in good agreement (better than one sigma) with the literature value derived by K19 from the mass-radius relations for M and K dwarfs of Boyajian et al. (2012).

We derived the mass of L 98-59 A using the Virtual Observatory SED Analyzer online tools[2] (VOSA, Bayo et al. 2008, see Appendix A.2 for more details). VOSA derives the mass by comparing the measured $T_{\rm eff}$ and bolometric luminosity to BT-Settl evolutionary tracks (Allard et al. 2012).

Finally, we determined the age of L 98-59 A using the photometry and distance provided by Gaia (see Appendix A.2 for more details). We compared the location of L 98-59 A in the color-magnitude diagram (see Fig 1) to mean sequences of stellar members of the β Pictoris moving group (∼20 Myr, Miret-Roig et al. 2020), Tucana-Horologium moving group (∼45 Myr, Bell et al. 2015), the Pleiades open cluster (∼120 Myr, Gossage et al. 2018), and the field (possible ages in the range 0.8–10 Gyr). This comparison allowed to infer that L 98–59 has an age consistent with that of the "field". This age estimate is confirmed by our kinematics analysis which indicates that L 98–59 A is a thin disk star which does not belong to any known young moving group (see Appendix A.2 and Table A.4).

The adopted radius, mass and ages of L 98-59 A are provided in Table 3.

[2] VOSA is publicly available online http://svo2.cab.inta-csic.es/theory/vosa/

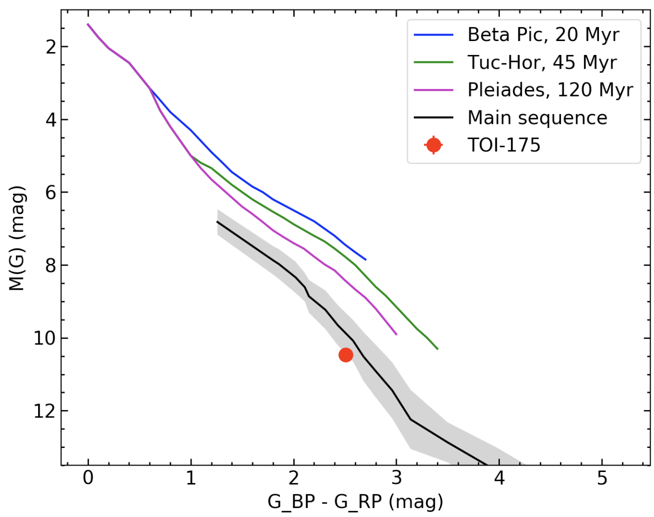

Fig. 1: Absolute magnitude (in the G Gaia band pass) versus color (magnitude difference between the Gaia bands G_{BP} and G_{RP}): L 98–59 A (alias TOI-175) is located in the Gaia color-magnitude diagram together with the mean sequences of young clusters and moving groups (Luhman 2018) and the main sequence of stars (Cifuentes et al. 2020). The error bars of L 98–59 A are smaller than the symbol size. The gray area represents the 1-σ dispersion of field M dwarfs.

3.3. Stellar Mg and Si abundances

Stellar abundances of Mg and Si are valuable constraints to model the interior of planets (see Section 5.3). However deriving individual abundances of M dwarfs from visible spectra is a very difficult task (e.g. Maldonado et al. 2020). In this work we estimated the abundances of Mg and Si following the procedure described in Adibekyan et al. (2017). From the APOGEE DR16 (Jönsson et al. 2020), we selected cool stars ($T_{\rm eff}$ < 5500 K, the choice of this temperature limit does not have a significant impact) with metallicities similar to L 98-59 A within 0.05 dex. We considered only stars with the highest signal-to-noise ratio (> 500) spectra to guarantee the high-quality of the extracted parameters and abundances of these stars. Since L 98-59 A is a member of the Galactic thin disk population (see Table A.4) only stars belonging to the thin disk population have been selected. The selection of the thin disk stars was based on the [Mg/Fe] abundance of the APOGEE stars (see e.g. Adibekyan et al. 2012). With these constraints, we ended up with a sample of about 1000 thin disk stars with properties similar to our target. The mean abundances of Mg and Si of these stellar analogs were adopted as proxy for the 'empirical' abundances and their standard deviation (star-to-star scatter) was adopted as the uncertainty (see Table 3).

3.4. Stellar rotation and activity periods

As mentioned in Section 2.1.1 and 2.1.2, the HARPS and ESPRESSO instruments give access to the time series of several activity indicators. These activity indicators are sensitive to variations of the stellar chromosphere, but not to the presence of planets in the system. As such, they are ideal to identify periodicities that arise from stellar chromospheric activity. To identify these periods, we computed the GLSP of all available activity indicators, see Fig 2. This figure also includes the GLSP of the RV measurements.

The GLSPs of the ESPRESSO activity indicators suggest that the rotation period ($P_{\rm rot}$) of L 98-59 A is $80.9^{+5.0}_{-5.3}$ days, measured on the highest peak of the FWHM GLSP, in agreement with C19. The GLSPs of the FWHM, the contrast of the CCF and the S-index all show peaks at this period with a false alarm probability (FAP) below 0.1 %. The FAP levels were computed using the analytical relation described in Zechmeister & Kürster (2009) for the Z-K normalisation. Our GLSPs of the HARPS activity indicators are consistent with the ones presented by C19. The GLSPs of the BIS, the S-index and H_α show peaks with FAP below 0.1 %, but not at the same period. However, as noticed by C19, the peak with the highest significance, which is found in the GLSP of H_α, is close to 80 days. This period is used by C19 as an estimate of the rotation period.

Photometric time series can also provide insight on the stellar rotation periods. The appearance and disappearance of dark and bright active regions like spots and plages due to stellar rotation produce a modulation in the light-curve. To investigate the presence of rotational modulation in the TESS LC, we first fitted the PDCSAP TESS LC with a GP and an offset for each sector. Using the retrieved offsets between the sectors, we computed the GLSP of the TESS LC presented in Fig 3 (see also Appendix C). The three highest peaks in this periodogram are, by order of decreasing amplitudes, at 93, 115 and 79 days. The presence of the 79 days periodicity is a confirmation of the 80 days period identified in the GLSPs of the spectroscopic time series presented in Fig 2. However the 93 and 115 days periodicities are not present in these periodograms.

Overall, the spectroscopic and photometric time series all exhibit power at a period of 80 days. This is thus our best guess for the rotation period of L 98-59. However the power spectrum of all these stellar activity indicators depict a complex activity pattern that does not seem to be fully described by only one periodicity and its harmonics.

4. Radial velocity and light-curve modeling

4.1. Search for additional planets in the L 98-59 system

K19 and C19 confirmed the presence of three transiting planets in the L 98-59 system. In this work, using the new sectors from TESS and the new RV data from ESPRESSO, we want to improve the precision of the planetary parameters and search for additional planets.

The GLSP of the HARPS RV data (see Fig 2-b) shows 6 peaks above a FAP of 10% around 3.7 (orbital period of planet c), 7.6 (orbital period of planet d), 13, 15, 23 and 40 ($\sim P_{\rm rot}/2$) days. The GLSP of the ESPRESSO RV data (see Fig 2-a) shows 2 narrow peaks above a FAP of 10% around 13 and 23 days. The fact that the two peaks identified in the ESPRESSO data are also present in the HARPS data and are not obvious fraction of the stellar rotation period indicates that there might be two additional planets in the system.

Due to the high computational cost linked to the analysis of the 9 TESS sectors, we divided our analysis in three steps. In the first step (Section 4.1.1), we analyze the TESS LC alone in order to refine the properties of the three known transiting planets and in particular their ephemerides. In the second step (Section 4.1.2), we use these ephemerides as *prior* for the analysis of the high-resolution spectroscopy data. The main objective of this second step is to assess the presence of additional planets in the L 98-59 system (Section 4.1.3). Finally in a third step (Section 4.2), we perform a final joint analysis of the RVs and the LC to obtain the final parameters of the system.

4.1.1. LC analysis

To model the planetary transits, we used a modified version[3] of the Python package `batman`[4] (Kreidberg 2015). The parameters used for each planets are: the orbital period P, the time of inferior conjunction ($t_{\rm ic}$), the products of the planetary eccentricity by the cosine and sine of the stellar argument of periastron ($e\cos\omega$ and $e\sin\omega$), the ratio of the planet's radius to that of the star (R_p/R_*) and the cosine of the planetary orbital inclination ($\cos i_p$). The model also included the stellar density (ρ_*). For the limb darkening law, we used the four coefficients of the non-linear model ($u_{1,TESS}$, $u_{2,TESS}$, $u_{3,TESS}$ and $u_{4,TESS}$). To this set of parameters, we added one additive jitter term ($\sigma_{\rm TESS}$) for the photometry all TESS sectors to account for a possible underestimation of the error bars (Baluev 2009).

To infer the values of these parameters, we maximized the *posterior* probability density function (PDF) of the model as prescribed by the Bayesian inference framework (e.g. Gregory 2005). The likelihood functions used were multi-dimensional Gaussians. To obtain robust error bars, we explored the parameter space thanks to an affine-invariant ensemble sampler for MCMC implemented in the Python package `emcee` (Foreman-Mackey et al. 2013). We adapted the number of walkers to the number of free parameters in our model. As a compromise between speed and efficiency, we used $\lceil n_{\rm free} \times 2.5 \times 2 \rceil / 2$ walkers, where $n_{\rm free}$ is the number of free parameters and $\lceil\ \rceil$ the ceiling function. This allowed us to have an even number of walkers which is at least twice ($\sim$ 2.5 times) the number of free parameters, as suggested by the authors of `emcee`. The initial values of each walkers were obtained from the output of a maximization of the *posterior* PDF done with the Nelder-Mead simplex algorithm (Nelder & Mead 1965) implemented in the Python package `scipy.optimize`. The initial values for the Nelder-Mead simplex maximization were drawn from the *prior*s of the parameters. The objective of this pre-maximization was to start the `emcee` exploration closer to the best region of the parameter space and thus reduce its convergence period. Our experience is that this usually results in a reduction of the overall computational time since the Nelder-Mead simplex algorithm is usually faster to converge than `emcee`.

The *prior* PDF assumed for the parameters were non-informative and given in Table 3 (column *prior*), along with references justifying their use when needed (column Source *prior*). Along with the *posterior* PDF provided in the same table, it allows for a qualitative assessment of the impact of the *prior* on the *posterior* (inferred values). A detailed description of the reasons behind the choice of each *prior* is given in Appendix D.

To choose the initial values for the analysis, the ones used to start the pre-minimization, we usually use values drawn from the *prior*s. However, here, we did not analyze the full TESS LC, only small portions of it around the location of the tran-

[3] The modified version of `batman` is available at https://github.com/odemangeon/batman. It prevents the code to stay trapped in an infinite loop for highly eccentric orbits.

[4] Several of the Python packages used for this work are publicly available on Github: `radvel` at https://github.com/California-Planet-Search/radvel, `george` at https://github.com/dfm/george, `batman` at https://github.com/lkreidberg/batman, `emcee` at https://github.com/dfm/emcee, `ldtk` at https://github.com/hpparvi/ldtk.

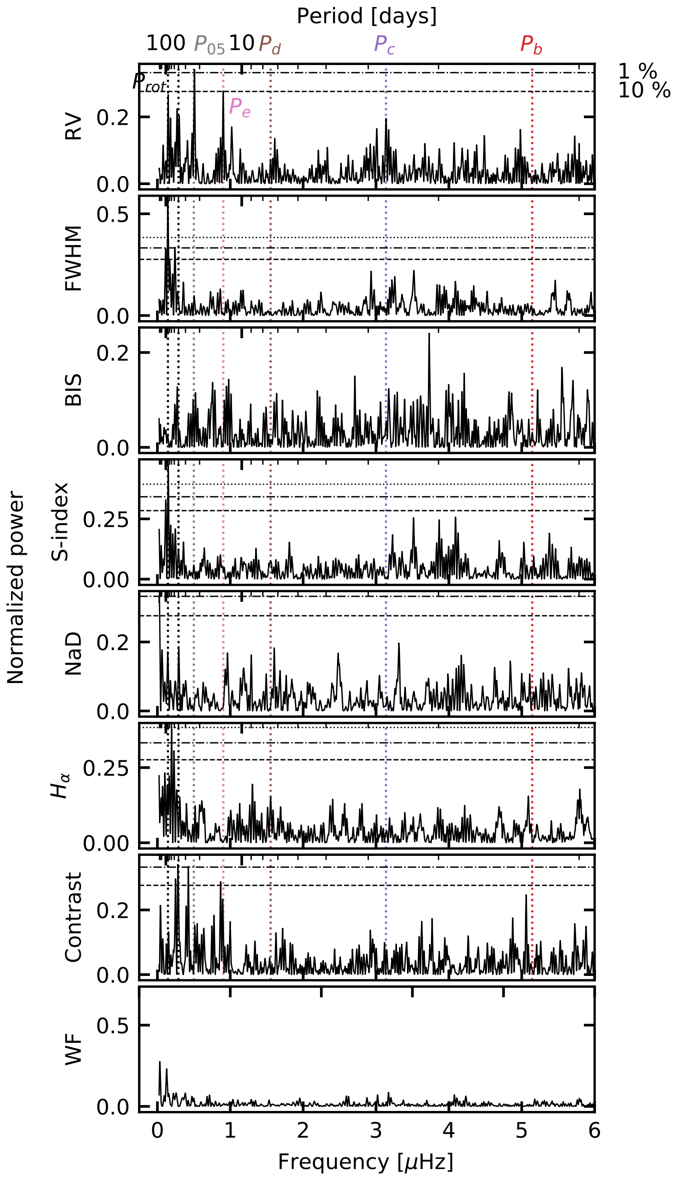

(a) ESPRESSO

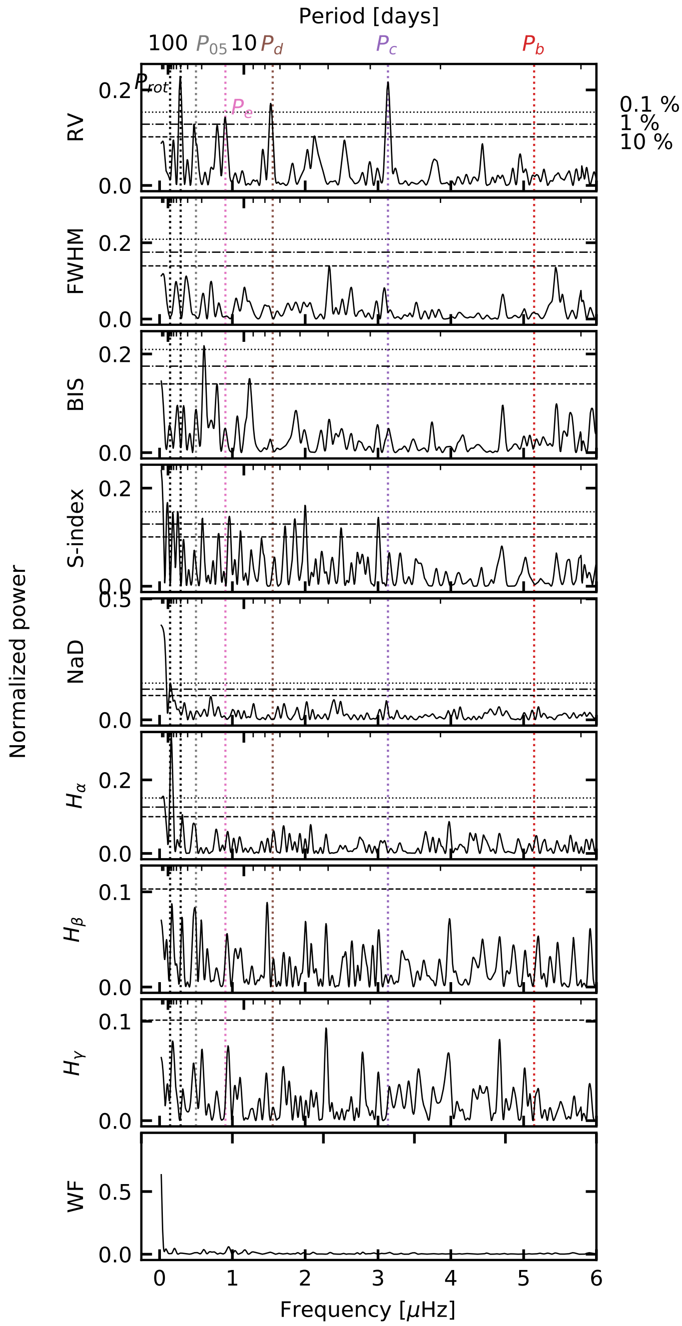

(b) HARPS

Fig. 2: . GLSP of the RV and activity indicators from ESPRESSO (a) and HARPS (b) data. The last row for both instruments presents the window function. The vertical dotted lines indicate from right to left the orbital period of the planets b, c, d, e, the planetary candidate 05, half and the full stellar rotation period (assumed here to be 80 days). The horizontal lines indicate the amplitude levels corresponding to 10 (dashed line), 1 (dot-dashed line) and 0.1 % (dotted line) of FAP. The amplitudes of the GLSPs are expressed using the Zechmeister-Kürster (ZK) normalisation described in Zechmeister & Kürster (2009, eq. 5). The FAP levels are computed using the analytical relation also described in Zechmeister & Kürster (2009) for this normalisation. We display the GLSP of the BIS for completness and comparison with C19, however we caution the reader regarding the reliability of BIS measurements from CCFs for M dwarfs (Rainer et al. 2020).

sits (see Section 2.2). Consequently, drawing initial values from non-informative *prior*s would very likely results in the simulated transits falling outside of the selected portions of the LC making the optimization impossible. To prevent this, we drew the initial values for P, $t_{\rm ic}$, R_p/R_* and $\cos i_p$ from the *posterior* PDFs obtained by K19.

We used 50,000 MCMC iterations and analyzed the chains using the same procedure than the one described in Section 2.2.

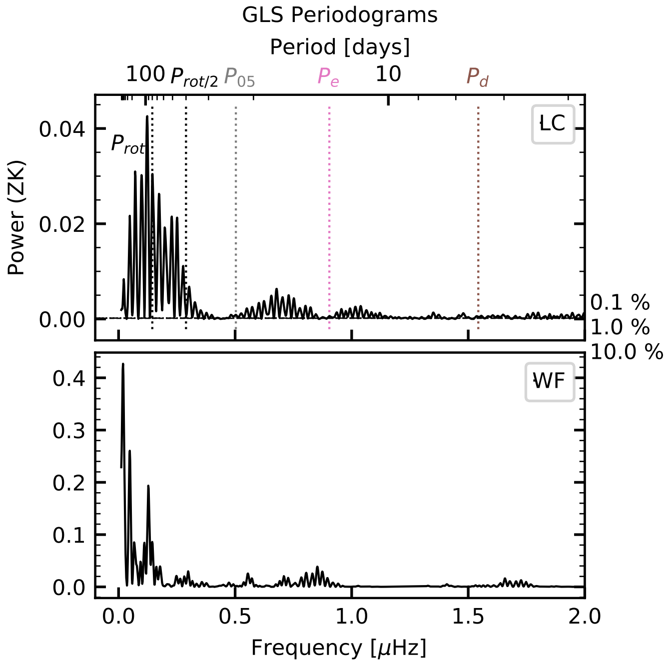

Fig. 3: . GLSP of the TESS LC. The format of the this figure is identical to Fig 2. In particular, the power of the GLSP is normalized using the Zechmeister-Kürster (ZK) normalisation normalisation. The highest peak in this periodogram is for a period of 93 days.

The *posterior* distributions of the parameters of the three transiting planets are then used as *prior*s for the analysis of the RVs.

4.1.2. RV analysis

Our model of the RVs is composed of three main components: The planetary model, the stellar activity model and the instrumental model.

C19, in their analysis of the HARPS data, demonstrated the importance of stellar activity mitigation for this system. They inferred an amplitude of $\sim 7\,\mathrm{m\,s^{-1}}$ for the stellar activity signal compared to $\lesssim 2\,\mathrm{m\,s^{-1}}$ for the semi-amplitude of the three planetary Keplerians. We thus paid particular care to the stellar activity mitigation and used two different approaches. The first approach is similar to the one used by C19. We fitted the RV data using Keplerians for the planetary signals and a GP with a quasi-periodic kernel for the stellar activity. The mathematical expression of the kernel of this GP is

$$K_{RV}(t_i, t_j) = {A_{RV}}^2 \exp\left[-\frac{(t_i - t_j)^2}{2\tau_{\mathrm{decay}}^2} - \frac{\sin^2\left(\frac{\pi}{P_{\mathrm{rot}}}|t_i - t_j|\right)}{2\gamma^2}\right] \quad (2)$$

where A_{rv} is the amplitude of the covariance, τ_{decay} is the decay time scale, P_{rot} is the period of recurrence of the covariance and γ is the periodic coherence scale (e.g. Grunblatt et al. 2015). We used the Python package `george`[4] (Ambikasaran et al. 2015) for the implementation. For the interpretation of the results, it is valuable to understand what is the impact of these hyper-parameters on the stellar activity model that this kernel produces (e.g. Angus et al. 2018; Haywood et al. 2014). A_{rv} scales with the amplitude of the stellar activity signal. P_{rot} indicates its main periodicity and is considered as a measure of the stellar rotation period (Angus et al. 2018). τ_{decay} and γ are two indicators of the coherence of the stellar activity signals. τ_{decay} governs the aperiodic coherence, the coherence between one period and the next ones. It is considered as a measure of the timescale of growth and decay of the active regions (Haywood et al. 2014). If it is longer than P_{rot}, the stellar activity pattern will change slowly from one rotation period to the next. γ controls the periodic coherence, the coherence of the signal within a stellar rotation period. It is considered as an indicator of the number of active regions. The larger γ is, the lower is the correlation between two points within a rotation period. γ governs the complexity of the harmonic content of the stellar activity signal (Angus et al. 2018).

For the second approach, we used the same model, but we jointly fitted the RVs and the FWHM values which accompany each RV measurement. The FWHM is fitted with a GP with a quasi-periodic kernel. This kernel is independent from the one used for the RV, but it uses the same hyper-parameters except for the amplitude (A_{FWHM}). This approach, inspired by Suárez Mascareño et al. (2020) and subsequently Lillo-Box et al. (2020), relies on the assumption that the variations of the FWHM are solely due to stellar activity and that their periodicity and coherence are the same as the stellar activity component of the RV. Under these assumptions, the joint fit of the RV and FWHM data sets allows to constrain better the hyper-parameters of the quasi-periodic kernel. Contrary to a first fit of the FWHMs followed by a second fit of the RVs using the marginalized *posterior* of the first fit as *prior* for the second, this approach preserves the correlation between the hyper-parameters.

For the planetary model, we used a constant systemic velocity (v_0) and one Keplerian function per planet in the system. The parameters of each Keplerians are: the semi-amplitude (K) of the RV signal, and similarly to Section 4.1.1 the orbital parameters P, t_{ic}, $e\cos\omega$ and $e\sin\omega$. The Keplerians were implemented using the Python packages `radvel`[4] (Fulton et al. 2018).

For the instrumental model, as mentioned in Section 2.1.2, due to the fiber-link change of ESPRESSO, we considered three instruments in our model: HARPS, ESPRESSO before (pre) and ESPRESSO after the intervention (post). We used $\mathrm{ESPRESSO_{pre}}$ as RV reference, meaning that v_0 is measured with the data coming from this instrument. We modeled the RV offsets with the other two instruments with two offset parameters ($\Delta\mathrm{RV}_{HARPS/\mathrm{pre}}$ and $\Delta\mathrm{RV}_{\mathrm{post/pre}}$). The FWHM is also subject to offsets between instruments and our model includes a constant level for each instrument (C_{pre}, C_{post}, C_{HARPS}). Finally, both for the RV and FWHM and for each instrument, we considered one additive jitter parameter to account for a potential underestimation of the measurement errors due to underestimated or even non-considered noise sources (Baluev 2009) ($\sigma_{RV,\mathrm{pre}}$, $\sigma_{RV,\mathrm{post}}$, $\sigma_{RV,HARPS}$, $\sigma_{FWHM,\mathrm{pre}}$, $\sigma_{FWHM,\mathrm{post}}$, $\sigma_{FWHM,HARPS}$).

To infer the values of these parameters, we performed a preminimization followed by an MCMC exploration as described in Section 4.1.1. The only difference is that this time the initial values are all drawn from the *prior*s. The *prior* PDFs assumed for the parameters are given in Table 3 except for the *prior* of P and t_{ic} of the three transiting planets. For these, we used the *posterior* PDFs of our analysis of the TESS LC (provided in a footnote of Table 3). A detailed description of the reasons behind the choice of each *prior* is given in Appendix D.

4.1.3. Evidence for additional planets in the L 98-59 system

We analyzed our RV data with six different models varying the number of planets in the system from three to five and the stellar mitigation approach including or not the FWHM data (see

Section 4.1.2). After each analysis, we inspected the output of the fit using plots like the one provided in Fig 4 and 5. Fig 4 shows the RV time series including the data from both instruments, the best planetary plus activity model and the residuals of this model. Fig 5 displays the GLSP of the combined RV data, the residuals, the planetary and stellar activity models sampled at the same times as the RV data and the window function (WF).

Extensive outputs are shown and discussed in Appendix F. From the fit of the three planets model (see Fig F.1 and F.2), the GLSP of the residuals displays a narrow peak at 13 days which we consider to be a strong insight for the presence of a 4th planet in the L 98-59 system at this period. For the analysis with four planets, we adopted a non-informative *prior* for the orbital period of the potential 4th planet (see Table 3). However to speedup convergence, we drew its initial values from a Gaussian distribution with a mean of 13 days and a standard deviation of 1 day. As shown in Fig 5, the GLSP of the residuals of the four planets model shows two narrow peaks around 1.743 and 2.341 days. These two peaks are aliases of one another. Due to the absence of transit signals in the TESS LC at these periods, we did not explore the possibility of a planet at these periods. However the peak at 23 days in the GLSP of the RVs appears to be absorbed by the stellar activity model despite the absence of signal at 23 days in the GLSPs of the FWHM and other activity indicators. We thus performed another analysis with five planets. We put again a non-informative *prior* for the orbital period of the potential 5th planet (see Table 3), but we drew its initial values from a Gaussian distribution with a mean of 23 days and standard deviation of 1 day. The fit converged towards a significant detection of the semi-amplitude of a 5th Keplerian signal.

Table 1 regroups the Bayesian Information Criterion (BIC) values computed for all the models tested. However, the BIC is not necessarily adapted for our analysis since our models are non-linear and our *prior*s uninformative, but relatively complex (see Appendix D). Consequently, we also computed the Bayesian evidence ($\mathcal{Z}$) of our models using the perrakis algorithm (Perrakis et al. 2014) using the Python implementation `bayev`[5] (Díaz et al. 2014). We computed the logarithm of $\mathcal{Z}$ thanks to 5000 sets of parameters values and repeated the process 150 times. From this 150 computations, we extracted the median and the 68 % confidence interval (using the 16th and 84th percentiles) and report these values in Table 1. The Bayesian evidences are in agreement with the BIC values. According to both criteria, the four planets model is favored and obtains the best values (minimum for the BIC and maximum for the Bayesian evidence). The only difference is in the absolute difference between the four and the five planets models. The BIC values of the five planets model is significantly higher ($\Delta BIC = 3$ for the RV+FWHM analysis), while the Bayesian evidences of these two models are very similar ($\Delta \ln \mathcal{Z} = 0.4$).

We thus conclude that our additional ESPRESSO RV campaign allows to identify one additional planet in the L 98-59 system: a fourth planet, hereafter planet e, with an orbital period of 12.80 days. We also identify a planetary candidate, a potential fifth planet, hereafter planet 05 with an orbital period of 23.2 days. We will see in Section 4.3 that these two additional planets do not transit.

Finally, retrieving the relevant information on L 98-59 from the new Gaia Early Data Release 3 (EDR3), we notice that an astrometric excess noise of 0.171 mas is reported, and the reduced unit weight error (RUWE) statistics has a value of 1.27. At G = 10.6 mag, the star is not so bright to be strongly affected by unmodeled systematics due to limited calibration. The Gaia EDR3 astrometry information (particularly RUWE) can thus be interpreted as providing weak evidence for the possible existence of an unresolved, massive outer companion (e.g. Belokurov et al. 2020; Penoyre et al. 2020). However, no long term trend is observed in our RV analysis.

[5] `bayev` is available at https://github.com/exord/bayev.

Table 1: Comparison of different models of the RVs of the L 98-59 system.

Nb planets	Types of data modeled	ΔBIC	$\Delta \ln \mathcal{Z}$
3	RV	0	$0^{0.23}_{-0.18}$
4	RV	-12.0	$7.08^{0.20}_{-0.15}$
5	RV	-6.2	$6.27^{0.48}_{-0.43}$
3	RV + FWHM	0	$0^{0.19}_{-0.13}$
4	RV + FWHM	-24.6	$11.9^{0.25}_{-0.17}$
5	RV + FWHM	-21.6	$11.5^{0.64}_{-0.29}$

Notes. ΔBIC and $\Delta \ln \mathcal{Z}$ indicate the difference between a given model and the value of the three planets model. For $\Delta \ln \mathcal{Z}$, our value for the three planets model is 0 affected by error bars, because our evidence estimates have quantified uncertainties and we use the best value of the three planets model to perform the difference.

4.2. Joint analysis of RV and photometry data

For the joint analysis of the RV and photometry data, due to the much higher computational time associated with the data of the 9 TESS sectors, we only fitted the best model identified by the RV only analysis: The four planets plus stellar activity model on the RV and FWHM data sets.

The model of the RV, FWHM and LC data as well as the inference process is similar to the ones used Section 4.1.2 and 4.1.1. The *prior* PDF assumed for the parameters are given in Table 3 and discussed in Appendix D. The initial values were drawn from the *prior* PDFs with a few exceptions. For P, t_{ic}, R_p/R_* and $\cos i_p$ of the three transiting planets, we used the *posterior* PDF obtained by K19 to draw the initial values. For P of the two exterior planets, we used Gaussian *prior*s with standard deviation of 1 day and a mean value of 13 and 23 days for planet e and planetary candidate 05 respectively.

From our MCMC exploration, we extracted the estimates of the model parameters using the median of the converged iterations as best model values and their 16th and 84th percentiles as the boundaries of the 68 % confidence level intervals. We also derived estimates for secondary parameters. As opposed to the model parameters (also called main or jumping parameters) described in the previous sections, secondary parameters are not used in the parametrization chosen for our modeling and are not necessary to perform the MCMC exploration. However, they provide quantities that can be computed from main parameters' values and are of interest to describe the system. The secondary parameters that we computed are: $\Delta F/F$ the transit depth, i the orbital inclination, e the eccentricity, ω the argument of periastron, a the orbital semi-major axis, $M_{\rm ref}$ the mean anomaly at a given reference time (set as BTJD = 1354, the time of the first TESS measurement), b the impact parameter, $D14$ the outer transit duration (duration between the 1$^{\rm st}$ and 4$^{\rm th}$ contact), $D23$ the inner transit duration (duration between the 2$^{\rm nd}$ and 3$^{\rm rd}$ contact), R_p the planetary radius, M_p the planetary mass, F_i the incident flux on the top of the planetary atmosphere, $T_{\rm eq}$ the equilibrium temperature of the planet (assuming an albedo of 0). After the full

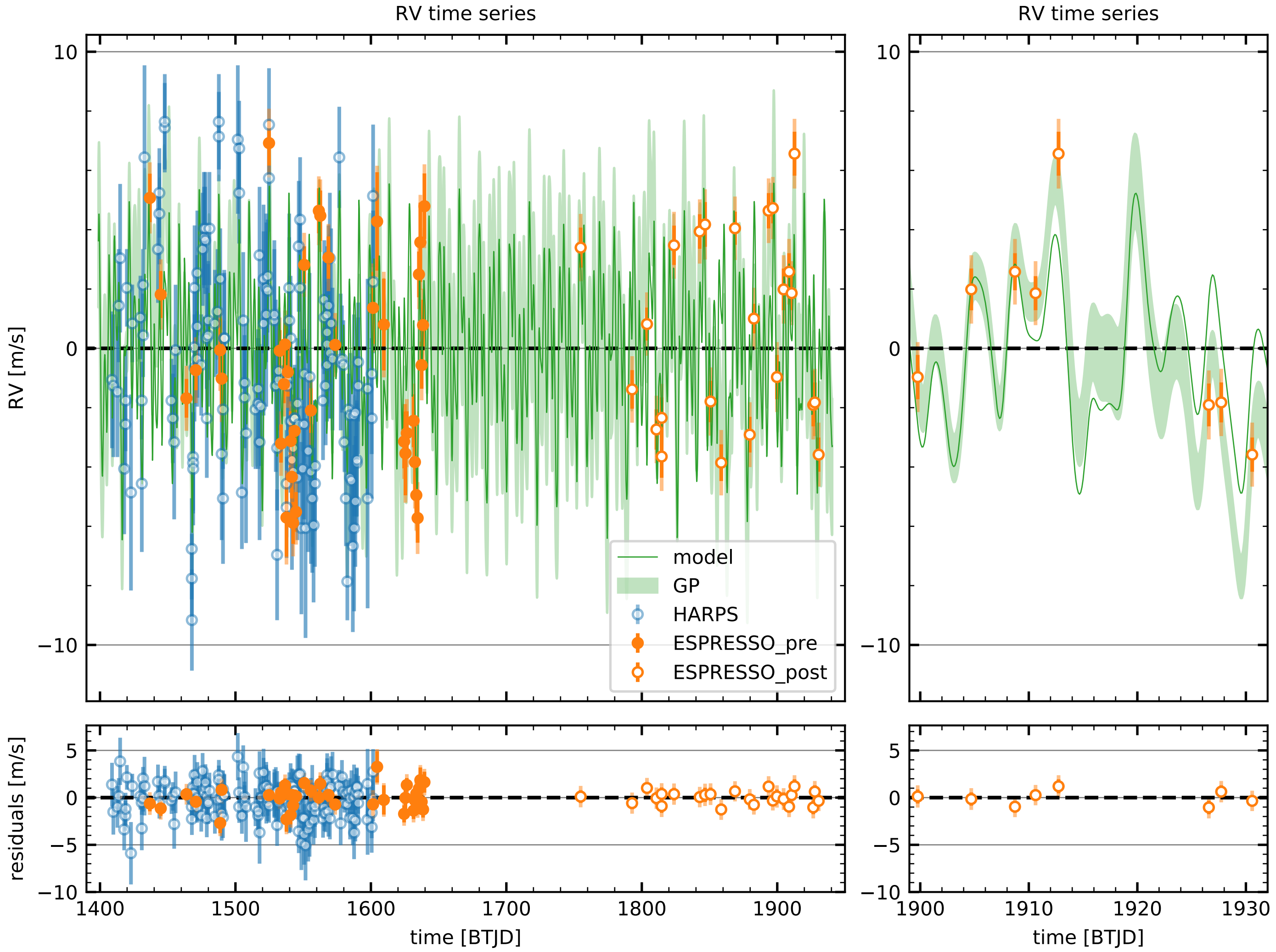

Fig. 4: Outcome of the fit of the four planets model: (Top-Left) RV time series along with the best model (solid green line) which include the planetary signals and best prediction from the GP stellar activity model. The one sigma uncertainties from the GP prediction are also displayed (shaded green area). For this plot, we subtract from the RV data the systemic velocity and the instruments offsets (see values in Table 3). (Bottom-left) Time series of the residuals of the best model. (Right) Zoom on a small portion of the time series for a better visualization of the short time-scale variations.

mcmc analysis, we drew, for each iteration a mass, a radius and an effective temperature value for the star using Gaussian distributions whose mean and standard deviation were set according the results of our stellar analysis (see Section 3 and Table 3). We then computed consistently the value of all the secondary parameters at each iteration of the `emcee` exploration which provided us with chains for the secondary parameters. Finally, we estimated their best model values and 68 % confidence intervals with the same method as the main parameters.

4.2.1. Dynamical Stability and parameters of the L 98-59 system

In compact multi-planetary systems like L 98-59, the assumption of long-term stability of the system can bring strong constraints on the planetary masses and orbital properties. Both K19 and C19 performed N-body dynamical simulations with the objective of constraining the orbital eccentricity of the planets in this system. Both studies provide compatible conclusions: The eccentricity of planets c and d should be 0.1 or less. As only the three inner planets were known at the time, the discovery of a fourth planet in this system requires to revisit this question. To do so, we used the framework implemented in the `spock` Python package (Tamayo et al. 2021, 2020, 2016). `spock` has been developed specifically to assess the stability of compact multi-planetary systems. It performs a short, and thus relatively inexpensive, N-body simulations (10^4 orbits of the inner planet) using the Python package `rebound` (Rein & Liu 2012). This simulation is then used to compute metrics based on established stability indicators (see Tamayo et al. 2020, and references therein). These metrics are then provided to a machine learning algorithm which estimates the probability that the simulated system is stable on the long term (typically 10^9 orbits of the inner planet). According to `spock`, the probability that the system described by the best model parameters inferred from our joint analysis of the RV, FWHM and photometry data is stable is 0. This means that the simulated system becomes unstable during the short N-body simulation (within 10^4 orbits of the inner planet). This stresses the importance of considering the dynamical stability for this system.

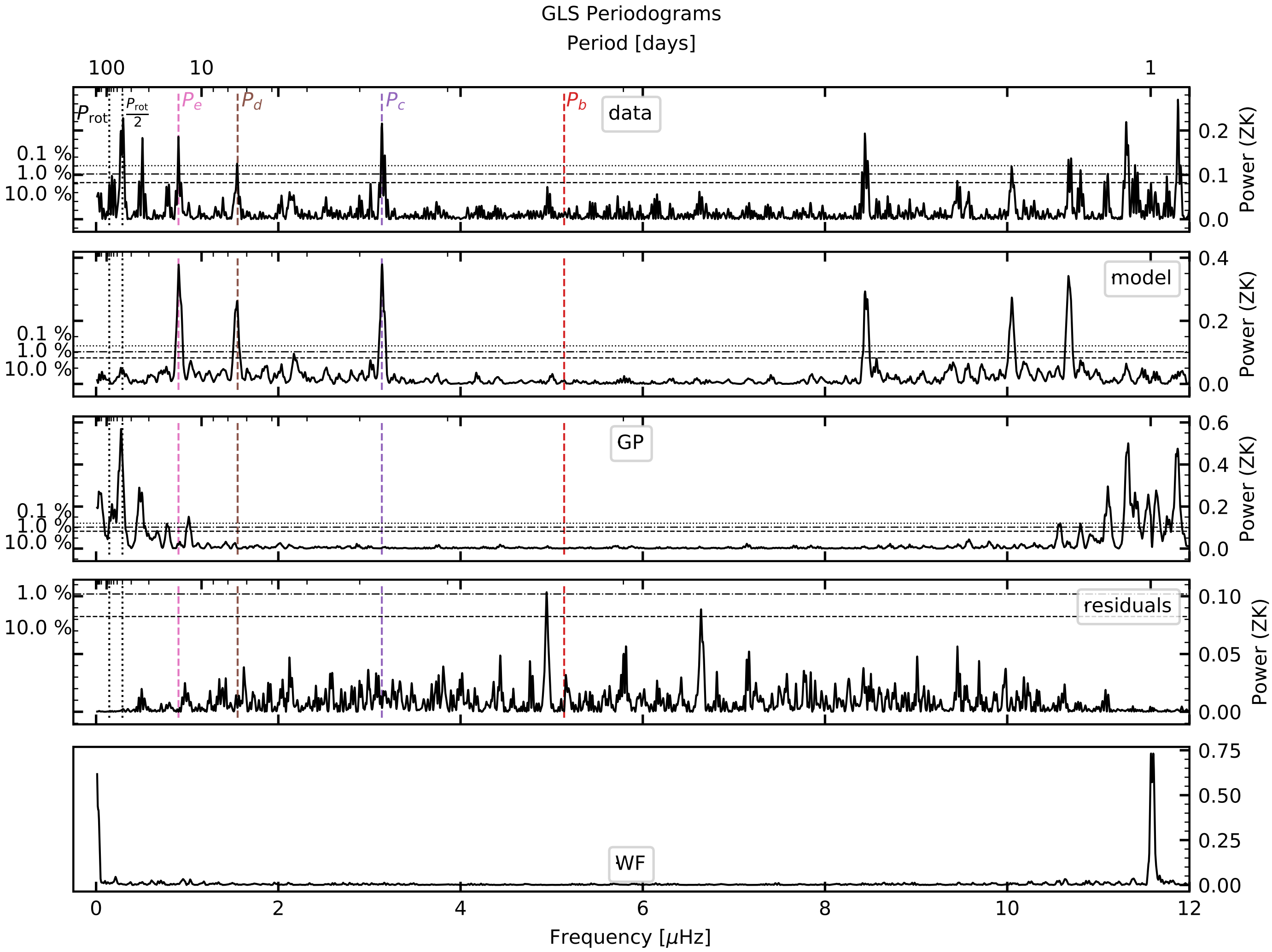

Fig. 5: Outcome of the fit of the four planets model: GLSPs of the RV time series (top) and of the planetary (second) and stellar activity (third) models sampled at the same times than the RV data, GLSP of the time series of the residuals (fourth) and the window function (bottom). The vertical lines on the GLSPs correspond to the orbital periods of planets b, c, d, e, half and the full rotation period (estimated at 80 days) from right to left.

Following the procedure described in Tamayo et al. (2021), we used `spock` to compute the probability of stability of the 10^5 versions of the L 98-59 systems described by the last 10^5 converged MCMC iterations of our joint analysis. For these computations, we used the `WHFast` symplectic integrator (Rein & Tamayo 2015) of `rebound`. We set a maximum distance of 0.4 AU ($\sim$ 6 times the semi-major axis of planet e) meaning that all simulations which led to one of the planets travelling 0.4 AU away from the barycenter of the system were stopped and their probability of stability were set to 0. For each MCMC iteration considered, we provided to the N-body simulation the mass of the star, the masses of the planets and their orbital elements: orbital period, semi-major axis, inclination, eccentricity, argument of periastron passage, mean anomaly at the beginning of the simulation (set as 1354 BTJD, the time of the first TESS measurement where BTJD = BJD - 2,457,000) and the longitude of ascending node. All these quantities, except the longitude of the ascending node, are either main or secondary parameters of the model (see Section 4.2). Their values were thus taken directly from the MCMC chains or their associated secondary parameters chains. For the longitudes of the ascending node, we drew values from a uniform distribution between 0 and 2 π.

With the probability of long term stability estimated for the last 10^5 iterations of our MCMC analysis of the joint fit of the data, we selected the iterations for which the probability of stability is above 40 % (as in Tamayo et al. 2020). This left us with only 1588 iterations. From these iterations and using their probability of stability as weight, we computed the weighted median and the weighted 16th and 84th percentile that we used as the best model values and the boundaries of the 68 % confidence interval respectively, as suggested by Tamayo et al. (2021). These estimates now describe a system with a high probability of long term stability and are reported in Table 3. The phase folded data (RV and photometry) and the best model are displayed in Fig 6 and 7. The main impact of the long term dynamical stability condition is on the eccentricity of planet c which decreases from $0.147^{+0.044}_{-0.048}$ to $0.103^{+0.045}_{-0.058}$. The eccentricities of the other planets stay unchanged or slightly decrease but well within one sigma of the previous estimates. The other parameters of the system are all compatible with their previous estimates at better than one sigma. With these updated estimates, the eccentricities of the three transiting planets satisfy the constraints derived by both K19 and C19 from their respective N-body simulations.

Finally, in order to assess if planets c and d are actually in mean motion resonance, we performed an additional N-body simulation for each iteration of the system with a probability of long term stability larger than 40 %. Like previously, for each iteration, we started the simulation using the parameter values found in the MCMC chains or the associated secondary parameters chains. We used `rebound` and the `WHFast` symplectic integrator with a time step of 10^{-4} year/2π (which corresponds to $\sim 10^3$ time steps per orbits of planet c). We integrated each simulation for the duration of our observations, 560 days between the beginning of the TESS observations and the last ESPRESSO point. For each time step, we calculated the 2:1 resonant angles (θ) of planet c and d, whose equation is (e.g. Quillen & French 2014, Eq. 1):

$$\theta_i = 2\lambda_d - \lambda_c - \omega_i\,,\ i \in [\mathrm{c},\mathrm{d}],$$

where λ is the mean longitude. As explained in Delisle (2017), if planet c and d are in mean motion resonance, their resonant angles should librate around a constant value. Following a procedure already used by Hara et al. (2020), we computed the derivative of the resonant angles using the finite difference approximation and averaged their value over the duration of the simulation. The normalized histogram of the 1588 values of the average derivatives of the resonant angles obtained is not compatible with zero and indicates that planet c and d are not in mean motion resonance.

4.3. Three transiting planets

Our RV analysis (see Section 4.1.3) concluded with the existence of a fourth planet and a planetary candidate which were not previously reported. Assuming that all planets in the system are coplanar, we can infer an orbital inclination of $88.21^{+0.35}_{-0.27}$ degrees and predict the impact parameter of planet e ($1.47^{+0.27}_{-0.30}$) and candidate 05 ($2.27^{+0.46}_{-0.43}$). From these impact parameter distributions, we estimate a probability of 4.8 and 0.11 % respectively that planet e and planetary candidate 05 transit their host star.

Using the 9 TESS sectors and the best ephemerides inferred from our analysis, we do not detect any sign of transit from either planet e or planetary candidate 05 (see Fig E.1 and Appendix E for more details on the analysis performed).

5. Discussion

5.1. Stellar activity modeling and mitigation

Stellar activity mitigation is a current focus of the exoplanet community due to its impact on the detection and characterization of low mass planets, both in RV (e.g. Dumusque et al. 2017) and transit photometry (e.g. Barros et al. 2020). For this analysis, we used a GP with a quasi-periodic kernel to account for the important stellar activity imprint on the RV data already identified by C19. We have analyzed the data with two slightly different approaches (see Section 4.1.2): one uses a GP on the RV data alone and the other uses the time series of a stellar activity indicator (here the FWHM) fitted simultaneously with the RV. The motivation for the latter approach is to put stronger constraints on the hyper parameters of the GP. In the case of L 98-59, we have already shown in Section 4.1.3 that the two approaches provide similar answers for the preferred model. A comparison of the *posterior* PDF of all common parameters to the two approaches shows that they also provide compatible estimates (within one sigma).

5.2. A four planets system hosting the smallest planet measured via RV

Thanks to the 6 additional sectors analyzed compared to K19, our analysis improves the characterization of the three transiting planets presented by K19 and C19 (see Table 3). The ephemerides of the three planets are improved by a factor ~ 2 and ~ 10 for the time of transit and the orbital period respectively. The relative precisions on the radius ratios (R_p/R_*) are also improved by a factor ~ 2 for the two inner planets and a factor ~ 4 for planet d.

We also improve the masses determination for these three planets. We derive the mass of planet b with 40 % of relative precision (C19 only provided an upper limit). With a RV semi-amplitude of $0.46^{+0.20}_{-0.17}$, m s^{-1} and a mass of $0.40^{+0.16}_{-0.15}$ M$_\oplus$(half the mass of Venus), L 98-59 b is currently the lightest exoplanet measured via RV[6]. It represents a new milestone which illustrates the capability of ESPRESSO to yield the mass of planets with RV signatures of the order of 10 cm.s^{-1} in multi-planetary systems even with the presence of stellar activity. The relative precision on the RV semi-amplitude of the other two previously known planets is also improved by a factor ~ 1.5 for planet c and ~ 2 for planet d. We obtain a relative mass precision of 11 and 14 % for planets c and d respectively which is the state-of-the-art for the mass measurement of super-Earths around M-dwarfs (Suárez Mascareño et al. 2020; Lillo-Box et al. 2020).

For the three transiting planets, we achieve bulk densities with relative precision of 46, 21 and 24 % for planet b, c and d respectively. Given the size and mass of these planets and the difficulties associated with a precise characterization of the mass and radius of M dwarfs, such density measurements are references for the field. The Fig 8 shows these three planets in the mass-radius diagram and in the context of the known exoplanet population. These three planets are located below the radius gap (Fulton et al. 2017; Fulton & Petigura 2018; Cloutier & Menou 2020) and appear to be mostly rocky (see Section 5.3).

We also expand the view of this system with the discovery of a fourth planet and a planetary candidate. These planets do not transit, but with minimum masses of $3.06^{+0.33}_{-0.37}$ and $2.46^{+0.66}_{-0.82}$ M$_\oplus$, they are probably both rocky planets or water worlds (also called ocean worlds, e.g. Adams et al. 2008). If confirmed, with an equilibrium temperature of 285^{+18}_{-17} K, the planetary candidate 05 would orbit in the habitable zone of its parent star.

5.3. Internal composition of three transiting super-Earths

We performed a Bayesian analysis to determine the *posterior* distribution of the planetary internal structure parameters. The method follows the one of Dorn et al. (2015) and Dorn et al. (2017), and has already been used in Mortier et al. (2020), Leleu et al. (2021) and Delrez et al. (2021). The model consists of two parts, the first is the forward model, which provides the planetary radius as a function of the internal structure parameters (iron molar fraction in the core, Si and Mg molar fraction in the mantle, mass fraction of all layers, age of the planet, irradiation from the star), the second is the Bayesian analysis which provides the *posterior* distribution of the internal structure parameters, given the

[6] Confirmed planets with lower masses which can be found in exoplanet.eu and the NASA exoplanet archive were all measured via transit timing variations.

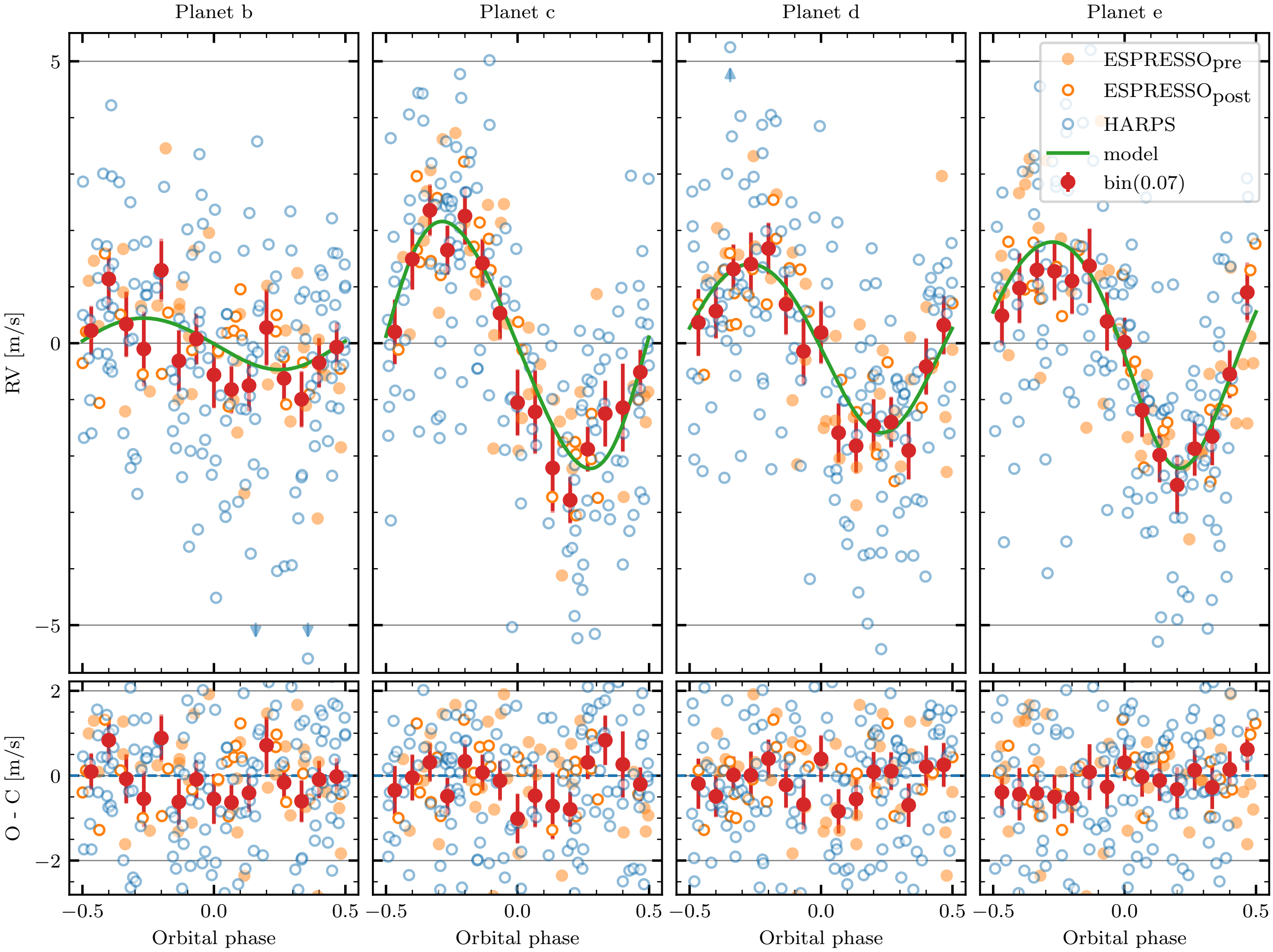

Fig. 6: Phase folded HARPS and ESPRESSO RVs, best model (top) and residuals (bottom) for the four planets. The HARPS data, presented in Section 2.1.1, are displayed with empty blue circles and the ESPRESSO data, presented in Section 2.1.2, are displayed with orange circles. The filled orange circles are for the data taken before the fiber change of ESPRESSO. The empty orange circles are for data taken after. For the clarity of the figures the error bars of the HARPS and ESPRESSO data points are not displayed. For this plot, the stellar activity model has been subtracted from each data point. The points with error bars in red correspond to averages of the data within evenly spaced bins in orbital phase whose size is 0.07 orbital period. The best model is shown with a green line. Before the subtraction of the stellar activity model the RMS of the RV data is 3.5, 3.4 and 3.2 m s^{-1} for HARPS, ESPRESSO$_{pre}$ and ESPRESSO$_{post}$ respectively. After the subtraction of the stellar activity model it is 2.9, 2.5 and 2.3 m s^{-1} for HARPS, ESPRESSO$_{pre}$ and ESPRESSO$_{post}$ respectively. Finally after subtraction of the planetary model the RMS of the residuals is 1.8, 1.2, 0.7 m s^{-1} for HARPS, ESPRESSO$_{pre}$ and ESPRESSO$_{post}$ respectively.

observed radii, masses, and stellar parameters (in particular its composition). The details of the analysis performed along with additional outputs are provided in Appendix G.

Fig 9 provides the ternary diagrams representing the *posterior* distributions of the composition of the three transiting planets in the L 98-59 system. Furthermore Fig G.1 to G.3 in Appendix G provide the detailed *posterior* distributions of the most important parameters (mass fractions, composition of the mantle) of each planets. The three planets are characterized by small iron cores (12 to 14 % in mass), which reflects the small iron abundance (compared to Si and Mg) in the star. According to the Bayesian analysis, the two innermost planets are likely to have a small mass fraction of water (the mode of the distribution is at 0) and a small mass of gas, if at all. Interestingly, the internal structure parameters of L 98-59 d are, according to the Bayesian analysis, substantially different: the mode of the water mass fraction distribution is at ~ 0.3 whereas the one of the gas mass peaks at $\sim 10^{-6} M_{\oplus}$. Since the Bayesian analysis provides the joint distribution of all planetary parameters, we can easily compute the probability that the mass fraction of gas and water is larger in L 98-59 d than in L 98-59 b and L 98-59 c. Using our model, the values are respectively 79.3 % and 72.0 % for gas and water for planet d *versus* planet b. It's 79.6 % and 79.1 % for gas and water respectively for planet d *versus* planet c. Planet d seems therefore likely more gas and water rich. On the other hand, planets b and c are very similar in composition. We emphasize finally the fact that these numbers result from the Bayesian analysis, and as such they depend on the assumed *prior*s that we took as un-informative as possible.

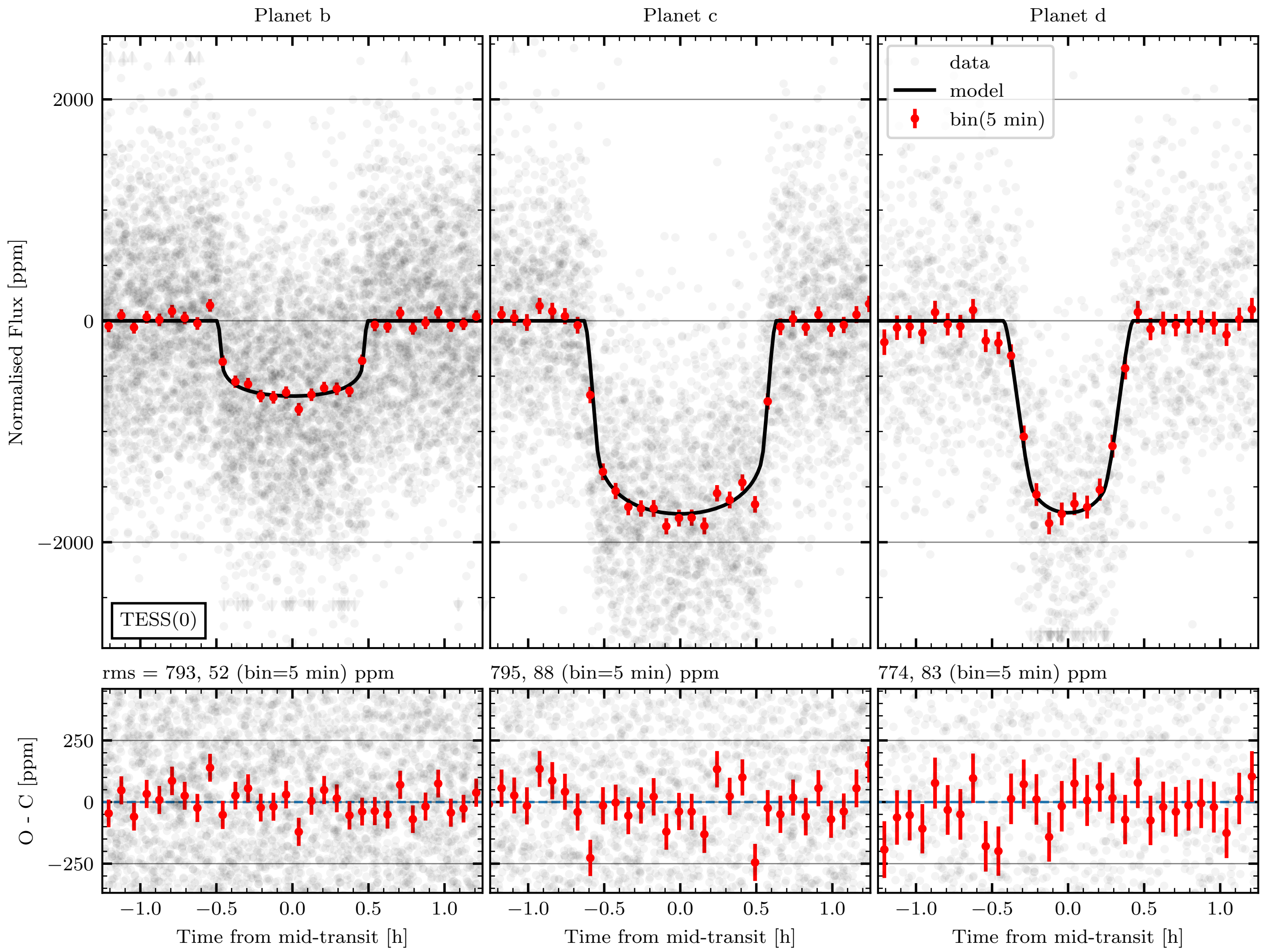

Fig. 7: Phase folded TESS LC, best model (top) and residuals (bottom) for the three transiting planets. The data presented in Section 2.2 are displayed in black. For the clarity of the figures the error bars are not displayed. The points with error bars in red correspond to averages of the data within evenly spaced bins in orbital phase whose size correspond to 5 min. The best model is shown with a black line. The standard deviation of the raw and binned residuals is indicated above each residuals plot.

Our modeling favors a dry and hydrogen/helium free model for planet b and c. The *posterior* distributions of their gas and water content peak at 0, but the three sigma confidence interval still allows for up to $\sim$ 25 % of water mass fraction (see Fig G.1 and G.2). In order to understand how promising planets b, c and even d are for atmospheric characterization, we need to understand if these warm planets ($T_{\rm eq}$ between $\sim$ 400 and $\sim$ 600 K) could retain a water dominated atmosphere. Providing a robust answer to this question requires to model the complex phase diagram of water (e.g. French et al. 2009; Mousis et al. 2020; Turbet et al. 2020), the radiative transfer in a water dominated atmosphere irradiated by an M star including potential runaway greenhouse effects (e.g Arnscheidt et al. 2019) and the hydrodynamic escape of water potentially assisted by ultra-violet photolysis (e.g Bourrier et al. 2017). Such an analysis is out of the scope of this paper. However we can look at the example of the TRAPPIST-1 system (Gillon et al. 2017; Luger et al. 2017) for comparison. Turbet et al. (2020) stressed the impact of irradiation on a water dominated atmosphere. If the irradiation received is above the runaway greenhouse irradiation threshold (e.g. Kasting et al. 1993), which should be the case for TRAPPIST-1 b to d (Wolf 2017), water should be in a steamed phase instead of a condensed phase as classically assumed. In this case the estimated water content of the planets decreases by orders of magnitude. The authors further concluded that planets smaller than 0.5 $M_\oplus$ that are more irradiated than the runaway greenhouse irradiation threshold should be unable to retain more than a few percent of water by mass due to an efficient hydrodynamic escape. Still on the TRAPPIST-1 system, Bourrier et al. (2017), following a theoretical study from Bolmont et al. (2017), attempted to assess the water loss suffered by the planets during their lifetime. The authors concluded that the planets g and those closer in could have lost up to 20 Earth oceans through hydrodynamic escape. However, they noted that depending on the exact efficiency of the photolysis, even TRAPPIST-1 b and c could still harbor significant amounts of water.

L 98-59 b is similar in mass and radius to TRAPPIST-1 d. However, it is significantly more irradiated ($T_{\rm eq}$ = 288 ± 5.6 K for TRAPPIST-1 d Gillon et al. 2017). L 98-59 b might thus undergo or have undergone an efficient hydrodynamic escape. L 98-59 c and d are more massive than any of the TRAPPIST-1 planets, but also more irradiated ($T_{\rm eq}$ = 400.1 ± 7.7 K for

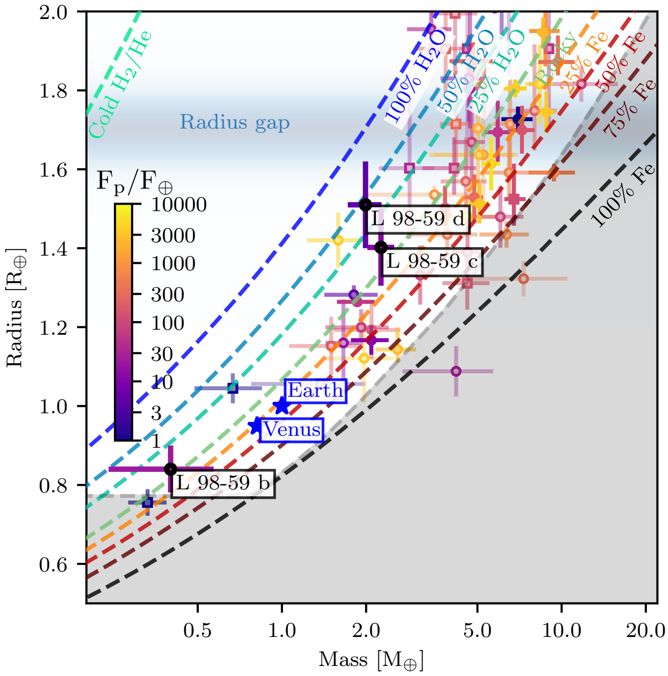

Fig. 8: Mass-radius diagram of the small planets' population. Each point represents a confirmed exoplanets with mass and radius measured with a relative precision better than 50 %. These data have been extracted from exoplanet.eu (Schneider et al. 2011).The shape of the points indicates the technique used to measure the mass of the planet: circles for RV and squares for transit timing variations. The color of the point reflects the intensity of the incident flux. The level of transparency of the error bars indicates the relative precision of the planetary bulk density. The better the precision is, the more opaque the error bars are. The three transiting planets in the L 98-59 system are labeled and appear circled in black. The labeled blue stars indicates the Solar system planets. The colored dashed lines are the mass-radius models from Zeng et al. (2016). The grey region indicates the maximum collision stripping of the mantle. The shaded blue horizontal line represent the radius gap (Fulton et al. 2017). L 98-59 b is in a sparsely populated region of the parameter space and currently the lightest planet whose mass has been measured via RV. Smaller planetary masses have all been measured via transit timing variation, like for Trappist-1 h (Gillon et al. 2017) on the left of L 98-59 b. This plot has been produced using the code available at `https://github.com/odemangeon/mass-radius_diagram`.

TRAPPIST-1 b Gillon et al. 2017) and the comparison is thus less pertinent. They are likely to have undergone runaway greenhouse effect, but their higher masses could inhibit the atmospheric escape. A more detailed study and observational evidence are thus required to assess robustly the nature and content of the atmosphere of the transiting planets in the L 98-59 system.

6. Conclusion: L 98-59, A benchmark system for super-Earth comparative exoplanetology around M-dwarf

Multi-planetary systems are ideal laboratories for exoplanetology since they offer the unique possibility to compare exoplanets formed in the same protoplanetary disc and illuminated by

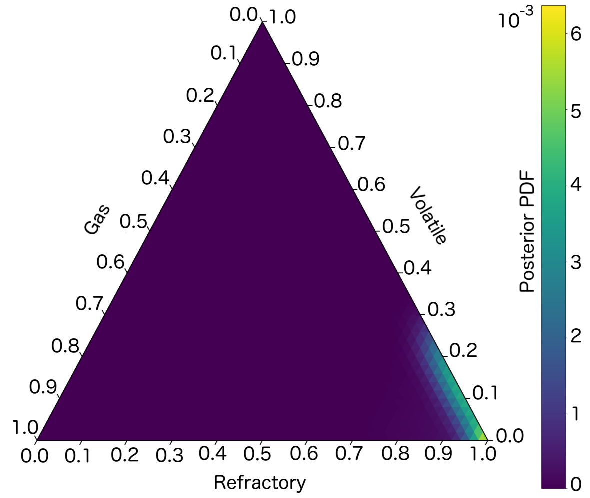

(a) Planet b

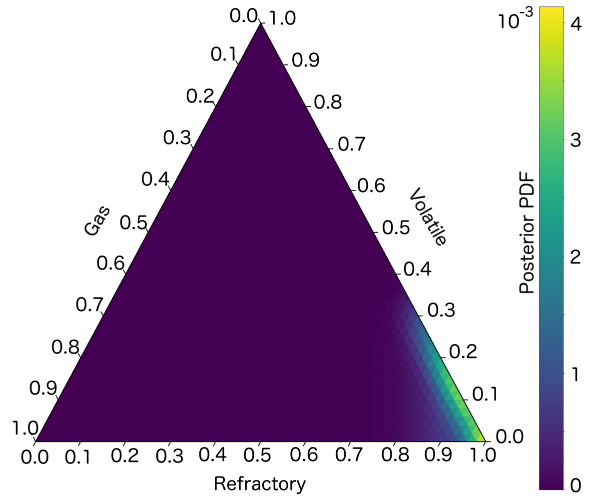

(b) Planet c

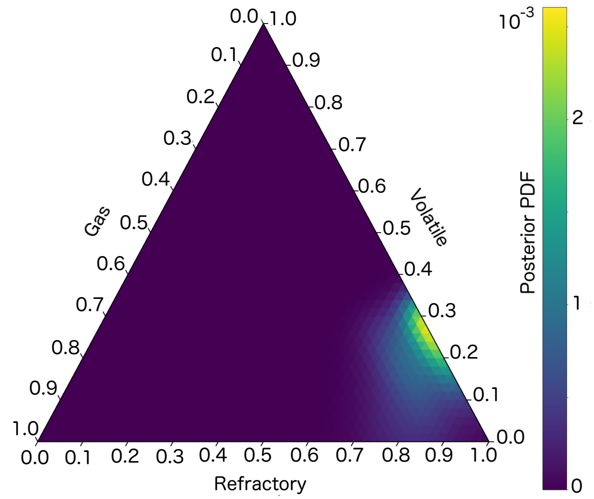

(c) Planet d

Fig. 9: Ternary diagrams showing the internal composition (mass fractions of the gas (H and He), the volatile (water) and the refractory elements) for the three transiting planets in the L 98-59 system.

the same star. According to exoplanet archive[7] (Akeson et al. 2013), we currently know 739 multi-planetary systems. A large fraction of them ($\sim$ 60 %) were discovered by the Kepler survey (Borucki et al. 2010; Lissauer et al. 2011). From a detailed characterization and analysis of the properties of the Kepler multi-planetary systems, Weiss et al. (2018, hereafter W18) extracted the "peas in a pod" configuration. They observed that consecutive planets in the same system tend to have similar sizes. They also appear to be preferentially regularly spaced. The authors also noted that the smaller the planets, the tighter their orbital configuration is. In Table 2, we computed the metrics identified by W18 for the L 98-59 system along with the distributions of these metrics derived by the authors from their sample. From Table 2, we conclude that the L 98-59 system is closely following the "peas in a pod" configuration. Most systems in the W18 sample have FGK host stars. For example, none of the 51 host stars which host 4 or more planets have a mass lower than $0.6 M_{\odot}$. The fact that the L 98-59 system also follows the "peas in a pod" configuration thus further strengthens the universality of this configuration and the constraints that it brings on planet formation theories. The only trend observed by W18 that the L 98-59 system does not display is the positive correlation between the equilibrium temperature difference of consecutive planets and their radius ratio. Furthermore, assuming a $v \sin i_*$ of 1 km/s, the semi-amplitude of the expected Rossiter-McLaughling effect (e.g. Queloz et al. 2000) is 40 cm/s, 1 m/s and 37 m/s for planet b, c and d respectively. Such amplitudes could be, at least for planet c and d, within the reach of high resolution spectrographs like ESPRESSO. This would give us access to the spin-orbital angle in this system constraining further its architecture and the possible mechanisms of its formation and migration.

Table 2: Peas in a pod statistics in the L 98-59 system

Metric from the L 98-59 system	W18 distribution
$R_c/R_b = 1.669$ $R_d/R_c = 1.077$	1.14 ± 0.63 (mean = 1.29)
$(P_d/P_c)/(P_c/P_b) = 1.232$ $(P_e/P_d)/(P_d/P_c) = 0.851$ $(P_{05}/P_e)/(P_e/P_d) = 1.053$	1.00 ± 0.27 (mean = 1.03)
$\Delta(c, b) = 15.260$ $\Delta(d, c) = 18.414$ $\Delta(e, d) = 13.569$ $\Delta(05, e) = 14.389$	Mode between 10 and 20 with long tail towards high values for 4+ planets systems
$T_{\mathrm{eq},b} - T_{\mathrm{eq},c} = 49$ K $T_{\mathrm{eq},c} - T_{\mathrm{eq},d} = 152$ K	$T_{\mathrm{eq},i} - T_{\mathrm{eq},i+1}$ positively correlated with R_{i+1}/R_i

Notes. - $\Delta(i, j)$ is the separation in mutual Hill radius (see Eq. 5 in W18) - In the column "W18 distribution", when the notation $x \pm y$ is used x is the median of the observed distribution and y is its standard deviation.

The fact that L 98-59 A is an M dwarf, sets this system apart amongst multi-planetary systems. According to exoplanet archive and the recent literature, there are currently only seven confirmed multi-planetary systems (including L-98-59) around M dwarfs for which the planetary masses and radius of at least two planets have been measured. The other six are TRAPPIST-1 (Gillon et al. 2017), LTT-3780 (Cloutier et al. 2020), TOI-1266 (Demory et al. 2020), LHS-1140 (Lillo-Box et al. 2020), K2-146 (Hamann et al. 2019) and Kepler-138 (Jontof-Hutter et al. 2015).

[7] https://exoplanetarchive.ipac.caltech.edu/

With a V magnitude of 11.7 and a distance of 10.6 pc, L 98-59 is the brightest and closest of these systems.

Finally, according to the transmission spectrum metric (TSM, Kempton et al. 2018), with values of 49, 37, and 255 for planet b, c and d respectively, the three transiting planets in the L 98-59 system are comfortably above the thresholds proposed by Kempton et al. (2018) for super-Earth atmospheric characterisation with the James Webb space telescope (JWST). This threshold is 12 for planets with radius below 1.5 R$_\oplus$ like planet b and c and 92 for planets with radius between 1.5 and 2.75 R$_\oplus$ like planet d. Fig 10 shows the TSM values for the well characterized small planets population. L 98-59 b and c are the two planets with the highest TSM value below 1.5 R$_\oplus$ and L 98-59 d has the second highest above. These three planets are thus amongst the most favorable warm to temperate ($T_{\rm eq}$ < 650 K) super-Earths (R_p < 1.5$R_\oplus$) for atmospheric characterization. Furthermore, L 98-59 is located at the border of the continuous viewing zone (∼ 200 days per year) of the JWST making it a golden system for atmospheric characterization and comparative planetology. Even if the TSM is specifically tailored to JWST, these planets are also suitable for transmission spectroscopy with other facilities like ESPRESSO, the Hubble space telescope (HST, Sirianni et al. 2005), NIRPS (Bouchy et al. 2017) or Ariel (Tinetti et al. 2016).

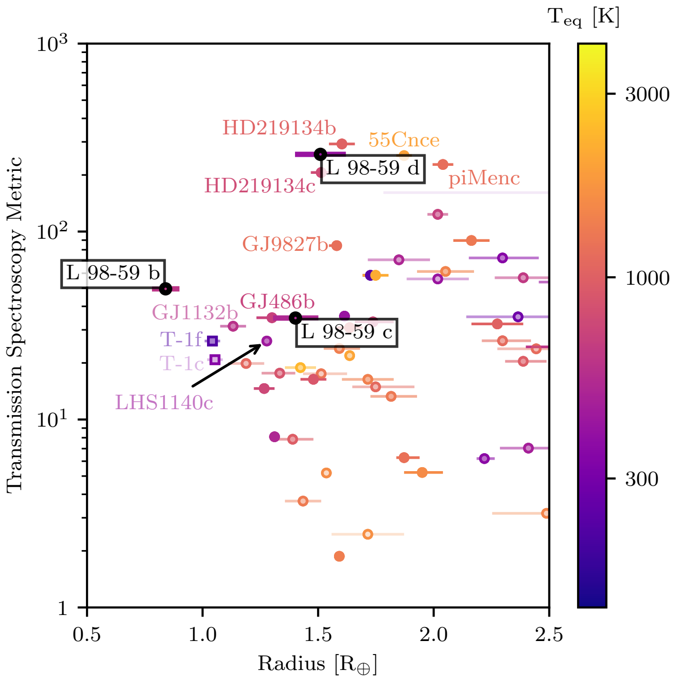

Fig. 10: Transmission spectrum metric versus planetary radius diagram of the small planets population. Each point represents a confirmed exoplanets with mass and radius measured with a relative precision better than 50 %. These data have been extracted from exoplanet archive. The shape of the points indicates the technique used to measure the mass of the planet: circles for RV and squares for transit timing variations. The color of the point reflects the equilibrium temperature of the planet. The level of transparency of the error bars indicates the relative precision of the planetary bulk density. The better the precision is, the more opaque the error bars are. The three transiting planets in the L 98-59 system are labeled and appear circled in black. We also display the names of the other planets with the highest transmission spectrum metrics. This plot has been produced using the code available at https://github.com/odemangeon/mass-radius_diagram.

Acknowledgements. The authors acknowledge the ESPRESSO project team for its effort and dedication in building the ESPRESSO instrument. This research has made use of the NASA Exoplanet Archive, which is operated by the California Institute of Technology, under contract with the National Aeronautics and Space Administration under the Exoplanet Exploration Program. This work has made use of data from the European Space Agency (ESA) mission (*Gaia*), processed by the *Gaia* Data Processing and Analysis Consortium (DPAC). Funding for the DPAC has been provided by national institutions, in particular the institutions participating in the *Gaia* Multilateral Agreement. This research has made use of the NASA/IPAC Infrared Science Archive, which is funded by the National Aeronautics and Space Administration and operated by the California Institute of Technology. This publication makes use of VOSA, developed under the Spanish Virtual Observatory project supported by the Spanish MINECO through grant AyA2017-84089. VOSA has been partially updated by using funding from the European Union's Horizon 2020 Research and Innovation Programme, under Grant Agreement nº 776403 (EXOPLANETS-A) This work was supported by FCT - Fundação para a Ciência - through national funds and by FEDER through COMPETE2020 - Programa Operacional Competitividade e Internacionalização by these grants: UID/FIS/04434/2019; UIDB/04434/2020; UIDP/04434/2020; PTDC/FIS-AST/32113/2017 & POCI-01-0145-FEDER-032113; PTDC/FIS-AST/28953/2017 & POCI-01-0145-FEDER-028953; PTDC/FIS-AST/28987/2017 & POCI-01-0145-FEDER-028987; PTDC/FIS-AST/30389/2017 & POCI-01-0145-FEDER-030389. O.D.S.D. is supported in the form of work contract (DL 57/2016/CP1364/CT0004) funded by FCT. J.I.G.H. acknowledges financial support from Spanish Ministry of Science and Innovation (MICINN) under the 2013 Ramón y Cajal programme RYC-2013-14875. J.I.G.H., A.S.M., R.R., and C.A.P. acknowledge financial support from the Spanish MICINN AYA2017-86389-P. A.S.M. acknowledges financial support from the Spanish Ministry of Science and Innovation (MICINN) under the 2019 Juan de la Cierva Programme. This work has been carried out with the support of the framework of the National Centre of Competence in Research PlanetS supported by the Swiss National Science Foundation (SNSF). The authors acknowledge the financial support of the SNSF and in particular YA and JH acknowledge the SNSF for supporting research through the grant 200020_19203. NJN acknowledges support form the following projects: CERN/FIS-PAR/0037/2019, PTDC/FIS-OUT/29048/2017. R. A. is a Trottier Postdoctoral Fellow and acknowledges support from the Trottier Family Foundation. This work was supported in part through a grant from FRQNT. A.A.K. and S.G.S. acknowledge the support from FCT in the form of the exploratory projects with references IF/00028/2014/CP1215/CT0002, IF/00849/2015/CP1273/CT0003. A.S. acknowledges support from the Italian Space Agency (ASI) under contract 2018-24-HH.0. The financial contribution from the agreement ASI-INAF n.2018-16-HH.0 is gratefully acknowledged. This project has received funding from the European Research Council (ERC) under the European Union's Horizon 2020 research and innovation programme (project FOUR ACES; grant agreement No 724427). Used Simbad, Vizier, exoplanet.eu. Most of the analyses presented in this paper were performed using the Python language (version 3.6) available at python and several scientific packages: Numpy (van der Walt et al. 2011), Scipy (Virtanen et al. 2020), Pandas (McKinney 2010), Ipython (Pérez & Granger 2007), Astropy (Astropy Collaboration et al. 2013, 2018) and Matplotlib (Hunter 2007).

References

Adams, E. R., Seager, S., & Elkins-Tanton, L. 2008, ApJ, 673, 1160

Adibekyan, V., Figueira, P., & Santos, N. C. 2017, in EWASS Special Session 4 (2017): Star-planet interactions (EWASS-SS4-2017)

Adibekyan, V. Z., Sousa, S. G., Santos, N. C., et al. 2012, A&A, 545, A32

Akeson, R. L., Chen, X., Ciardi, D., et al. 2013, PASP, 125, 989

Albrecht, S., Winn, J. N., Marcy, G. W., et al. 2013, ApJ, 771, 11

Allard, F., Homeier, D., & Freytag, B. 2012, Philosophical Transactions of the Royal Society of London Series A, 370, 2765

Ambikasaran, S., Foreman-Mackey, D., Greengard, L., Hogg, D. W., & O'Neil, M. 2015, IEEE Transactions on Pattern Analysis and Machine Intelligence, 38

Angus, R., Morton, T., Aigrain, S., Foreman-Mackey, D., & Rajpaul, V. 2018, MNRAS, 474, 2094

Antoniadis-Karnavas, A., Sousa, S. G., Delgado-Mena, E., et al. 2020, A&A, 636, A9

Arnscheidt, C. W., Wordsworth, R. D., & Ding, F. 2019, ApJ, 881, 60

Astropy Collaboration, Price-Whelan, A. M., Sipőcz, B. M., et al. 2018, AJ, 156, 123

Astropy Collaboration, Robitaille, T. P., Tollerud, E. J., et al. 2013, A&A, 558, A33

Astudillo-Defru, N., Díaz, R. F., Bonfils, X., et al. 2017a, A&A, 605, L11
Astudillo-Defru, N., Forveille, T., Bonfils, X., et al. 2017b, A&A, 602, A88
Bailer-Jones, C. A. L., Rybizki, J., Fouesneau, M., Mantelet, G., & Andrae, R. 2018, AJ, 156, 58
Baluev, R. V. 2009, MNRAS, 393, 969
Baranne, A., Queloz, D., Mayor, M., et al. 1996, A&A Supplement, 119, 373
Barros, S. C. C., Almenara, J. M., Demangeon, O., et al. 2015, MNRAS, 454, 4267
Barros, S. C. C., Demangeon, O., & Deleuil, M. 2016, A&A, 594, A100
Barros, S. C. C., Demangeon, O., Díaz, R. F., et al. 2020, A&A, 634, A75
Batalha, N. M., Rowe, J. F., Bryson, S. T., et al. 2013, ApJ Supplement Series, 204, 24
Bayo, A., Rodrigo, C., Barrado Y Navascués, D., et al. 2008, A&A, 492, 277
Bell, C. P. M., Mamajek, E. E., & Naylor, T. 2015, MNRAS, 454, 593
Belokurov, V., Penoyre, Z., Oh, S., et al. 2020, MNRAS, 496, 1922
Benedict, G. F., Henry, T. J., Franz, O. G., et al. 2016, AJ, 152, 141
Bolmont, E., Selsis, F., Owen, J. E., et al. 2017, MNRAS, 464, 3728
Borucki, W. J., Koch, D., Basri, G., et al. 2010, Science, 327, 977
Bouchy, F., Doyon, R., Artigau, É., et al. 2017, The Messenger, 169, 21
Bouchy, F., Pepe, F., & Queloz, D. 2001, A&A, 374, 733
Bourrier, V., de Wit, J., Bolmont, E., et al. 2017, AJ, 154, 121
Boyajian, T. S., von Braun, K., van Belle, G., et al. 2012, ApJ, 757, 112
Byrd, R. H., Lu, P., Nocedal, J., & Zhu, C. 1995, SIAM Journal on Scientific Computing, 16, 1190
Casagrande, L., Flynn, C., & Bessell, M. 2008, MNRAS, 389, 585
Cifuentes, C., Caballero, J. A., Cortés-Contreras, M., et al. 2020, A&A, 642, A115
Cloutier, R., Astudillo-Defru, N., Bonfils, X., et al. 2019, A&A, 629, A111
Cloutier, R., Eastman, J. D., Rodriguez, J. E., et al. 2020, AJ, 160, 3
Cloutier, R. & Menou, K. 2020, AJ, 159, 211
Cosentino, R., Lovis, C., Pepe, F., et al. 2012, Proceedings of the SPIE: Ground-based and Airborne Instrumentation for Astronomy IV, 8446, 84461V
Crane, J. D., Shectman, S. A., & Butler, R. P. 2006, Proceedings of the SPIE: Ground-based and Airborne Instrumentation for Astronomy, 6269, 626931
Crane, J. D., Shectman, S. A., Butler, R. P., et al. 2010, Proceedings of the SPIE: Ground-based and Airborne Instrumentation for Astronomy III, 7735, 773553
Crane, J. D., Shectman, S. A., Butler, R. P., Thompson, I. B., & Burley, G. S. 2008, Proceedings of the SPIE: Ground-based and Airborne Instrumentation for Astronomy II, 7014, 701479
Cutri, R. M., Skrutskie, M. F., van Dyk, S., et al. 2003, VizieR Online Data Catalog, 2246
Delisle, J.-B. 2017, A&A, 605, A96
Delrez, L., Ehrenreich, D., Alibert, Y., et al. 2021, Nature Astronomy, Advanced Online Publication
Demory, B.-O., Pozuelos, F. J., Gómez Maqueo Chew, Y., et al. 2020, A&A, 642, A49
Díaz, R. F., Almenara, J. M., Santerne, A., et al. 2014, MNRAS, 441, 983
Díaz, R. F., Cincunegui, C., & Mauas, P. J. D. 2007, MNRAS, 378, 1007
Dorn, C., Khan, A., Heng, K., et al. 2015, A&A, 577, A83
Dorn, C., Venturini, J., Khan, A., et al. 2017, A&A, 597, A37
Dubber, S. C., Mortier, A., Rice, K., et al. 2019, MNRAS, 490, 5103
Dumusque, X., Borsa, F., Damasso, M., et al. 2017, A&A, 598, A133
Foreman-Mackey, D. 2018, Research Notes of the American Astronomical Society, 2, 31
Foreman-Mackey, D., Agol, E., Ambikasaran, S., & Angus, R. 2017, AJ, 154, 220
Foreman-Mackey, D., Hogg, D. W., Lang, D., & Goodman, J. 2013, PASP, 125, 306
French, M., Mattsson, T. R., Nettelmann, N., & Redmer, R. 2009, Physical Review B, 79, 054107
Fulton, B. J. & Petigura, E. A. 2018, AJ, 156, 264
Fulton, B. J., Petigura, E. A., Blunt, S., & Sinukoff, E. 2018, PASP, 130, 044504
Fulton, B. J., Petigura, E. A., Howard, A. W., et al. 2017, AJ, 154, 109
Gaia Collaboration. 2018, VizieR Online Data Catalog, 1345
Gaia Collaboration, Brown, A. G. A., Vallenari, A., et al. 2018, A&A, 616, A1
Gaidos, E., Mann, A. W., Lépine, S., et al. 2014, MNRAS, 443, 2561
Gardner, J. P., Mather, J. C., Clampin, M., et al. 2006, Space Science Reviews, 123, 485
Geweke, J. 1992, Bayesian Statistics, 4, 641
Gillon, M., Jehin, E., Magain, P., et al. 2011, EPJ Web of Conferences: Detection and Dynamics of Transiting Exoplanets, St. Michel l'Observatoire, France, Edited by F. Bouchy; R. Díaz; C. Moutou, 11, 06002
Gillon, M., Triaud, A. H. M. J., Demory, B.-O., et al. 2017, Nature, 542, 456
Goodman, J. & Weare, J. 2010, Communications in Applied Mathematics and Computational Science, 5, 65
Gossage, S., Conroy, C., Dotter, A., et al. 2018, ApJ, 863, 67
Greene, T. P., Line, M. R., Montero, C., et al. 2016, ApJ, 817, 17
Gregory, P. C. 2005, Bayesian Logical Data Analysis for the Physical Sciences: A Comparative Approach with 'Mathematica' Support. Edited by P. C. Gregory. ISBN 0 521 84150 X (hardback); QA279.5.G74 2005 519.5'42 – dc22; 200445930. Published by Cambridge University Press
Grunblatt, S. K., Howard, A. W., & Haywood, R. D. 2015, ApJ, 808, 127
Hakim, K., Rivoldini, A., Van Hoolst, T., et al. 2018, Icarus, 313, 61
Haldemann, J., Alibert, Y., Mordasini, C., & Benz, W. 2020, A&A, 643, A105
Hamann, A., Montet, B. T., Fabrycky, D. C., Agol, E., & Kruse, E. 2019, AJ, 158, 133
Hara, N. C., Bouchy, F., Stalport, M., et al. 2020, A&A, 636, L6
Haywood, R. D., Collier Cameron, A., Queloz, D., et al. 2014, MNRAS, 443, 2517
Henden, A. A., Templeton, M., Terrell, D., et al. 2016, VizieR Online Data Catalog, 2336
Hippke, M. & Heller, R. 2019, A&A, 623, A39
Howell, S. B., Sobeck, C., Haas, M., et al. 2014, PASP, 126, 398
Hunter, J. D. 2007, Computing in Science & Engineering, 9, 90
Husser, T.-O., Wende-von Berg, S., Dreizler, S., et al. 2013, A&A, 553, A6
Jenkins, J. M., Twicken, J. D., McCauliff, S., et al. 2016, Proceedings of SPIE: Software and Cyberinfrastructure for Astronomy IV, 9913, 99133E
Jönsson, H., Holtzman, J. A., Allende Prieto, C., et al. 2020, AJ, 160, 120
Jontof-Hutter, D., Rowe, J. F., Lissauer, J. J., Fabrycky, D. C., & Ford, E. B. 2015, Nature, 522, 321
Kaltenegger, L. 2017, A&A Rev., 55, 433
Kasting, J. F., Whitmire, D. P., & Reynolds, R. T. 1993, Icarus, 101, 108
Kempton, E. M.-R., Bean, J. L., Louie, D. R., et al. 2018, PASP, 130, 114401
Kipping, D. M. 2013, MNRAS, 434, L51
Kostov, V. B., Schlieder, J. E., Barclay, T., et al. 2019, AJ, 158, 32
Kovács, G., Zucker, S., & Mazeh, T. 2002, A&A, 391, 369
Kreidberg, L. 2015, PASP, 127, 1161
Kreidberg, L., Koll, D. D. B., Morley, C., et al. 2019, Nature, 573, 87
Leleu, A., Alibert, Y., Hara, N. C., et al. 2021, A&A, 649, A26
Lillo-Box, J., Figueira, P., Leleu, A., et al. 2020, A&A, 642, A121
Lissauer, J. J., Ragozzine, D., Fabrycky, D. C., et al. 2011, ApJ Supplement Series, 197, 8
Lopez, E. D. & Fortney, J. J. 2014, ApJ, 792, 1
Lovis, C., Dumusque, X., Santos, N. C., et al. 2011, arXiv e-prints, arXiv:1107.5325
Luger, R., Sestovic, M., Kruse, E., et al. 2017, Nature Astronomy, 1, 0129
Luhman, K. L. 2018, AJ, 156, 271
Maldonado, J., Micela, G., Baratella, M., et al. 2020, A&A, 644, A68
Mandt, K., Mousis, O., & Chassefière, E. 2015, Icarus, 254, 259
Mann, A. W., Dupuy, T., Kraus, A. L., et al. 2019, ApJ, 871, 63
Mann, A. W., Feiden, G. A., Gaidos, E., Boyajian, T., & von Braun, K. 2015, ApJ, 804, 64
Marboeuf, U., Thiabaud, A., Alibert, Y., Cabral, N., & Benz, W. 2014, A&A, 570, A36
Marfil, E., Tabernero, H. M., Montes, D., et al. 2020, in Contributions to the XIV.0 Scientific Meeting (virtual) of the Spanish Astronomical Society, 156
Mayor, M., Pepe, F., Queloz, D., et al. 2003, The Messenger, 114, 20
McKinney, W. 2010, in Proceedings of the 9th Python in Science Conference (Stéfan van der Walt and Jarrod Millman), 51–56
Millholland, S., Wang, S., & Laughlin, G. 2017, ApJ, 849, L33
Miret-Roig, N., Galli, P. A. B., Brandner, W., et al. 2020, A&A, 642, A179
Morales, J. L. & Nocedal, J. 2011, ACM Transactions on Mathematical Software, 38, 7:1
Morley, C. V., Kreidberg, L., Rustamkulov, Z., Robinson, T., & Fortney, J. J. 2017, ApJ, 850, 121
Mortier, A., Zapatero Osorio, M. R., Malavolta, L., et al. 2020, MNRAS, 499, 5004
Mousis, O., Deleuil, M., Aguichine, A., et al. 2020, ApJ, 896, L22
Nelder, J. A. & Mead, R. 1965, Computer Journal, 7, 308
Neves, V., Bonfils, X., Santos, N. C., et al. 2012, A&A, 538, A25
Noyes, R. W., Weiss, N. O., & Vaughan, A. H. 1984, ApJ, 287, 769
Parviainen, H. & Aigrain, S. 2015, MNRAS, 453, 3821
Pecaut, M. J. & Mamajek, E. E. 2013, ApJ Supplement Series, 208, 9
Penoyre, Z., Belokurov, V., Wyn Evans, N., Everall, A., & Koposov, S. E. 2020, MNRAS, 495, 321
Pepe, F., Cristiani, S., Rebolo, R., et al. 2021, A&A, 645, A96
Pérez, F. & Granger, B. E. 2007, Computing in Science and Engineering, 9, 21
Perrakis, K., Ntzoufras, I., & Tsionas, E. G. 2014, Computational Statistics & Data Analysis, 77, 54
Plez, B. 2012, Turbospectrum: Code for spectral synthesis, Astrophysics Source Code Library
Queloz, D., Eggenberger, A., Mayor, M., et al. 2000, A&A, 359, L13
Queloz, D., Henry, G. W., Sivan, J. P., et al. 2001, A&A, 379, 279
Quillen, A. C. & French, R. S. 2014, MNRAS, 445, 3959
Quirrenbach, A., Amado, P. J., Caballero, J. A., et al. 2014, Proceedings of the SPIE: Ground-based and Airborne Instrumentation for Astronomy V, 9147, 12

Rainer, M., Borsa, F., & Affer, L. 2020, Experimental Astronomy, 49, 73
Rein, H. 2012, MNRAS, 427, L21
Rein, H. & Liu, S.-F. 2012, A&A, 537, A128
Rein, H. & Tamayo, D. 2015, MNRAS, 452, 376
Rice, K., Malavolta, L., Mayo, A., et al. 2019, MNRAS, 484, 3731
Ricker, G. R., Winn, J. N., Vanderspek, R., et al. 2015, Journal of Astronomical Telescopes, Instruments, and Systems, 1, 014003
Ryabchikova, T., Piskunov, N., Kurucz, R. L., et al. 2015, Phys. Scr, 90, 054005
Schneider, J., Dedieu, C., Le Sidaner, P., Savalle, R., & Zolotukhin, I. 2011, A&A, 532, A79
Schweitzer, A., Passegger, V. M., Cifuentes, C., et al. 2019, A&A, 625, A68
Sirianni, M., Jee, M. J., Benítez, N., et al. 2005, PASP, 117, 1049
Skrutskie, M. F., Cutri, R. M., Stiening, R., et al. 2006, AJ, 131, 1163
Smith, J. C., Stumpe, M. C., Van Cleve, J. E., et al. 2012, PASP, 124, 1000
Sotin, C., Grasset, O., & Mocquet, A. 2007, Icarus, 191, 337
Stassun, K. G., Collins, K. A., & Gaudi, B. S. 2017, AJ, 153, 136
Stassun, K. G. & Torres, G. 2016, AJ, 152, 180
Stumpe, M. C., Smith, J. C., Catanzarite, J. H., et al. 2014, PASP, 126, 100
Suárez Mascareño, A., Faria, J. P., Figueira, P., et al. 2020, A&A, 639, A77
Tabernero, H. M., Dorda, R., Negueruela, I., & González-Fernández, C. 2018, MNRAS, 476, 3106
Tabernero, H. M., Dorda, R., Negueruela, I., & Marfil, E. 2021, A&A, 646, A98
Tamayo, D., Cranmer, M., Hadden, S., et al. 2020, Proceedings of the National Academy of Science, 117, 18194
Tamayo, D., Gilbertson, C., & Foreman-Mackey, D. 2021, MNRAS, 501, 4798
Tamayo, D., Silburt, A., Valencia, D., et al. 2016, ApJ, 832, L22
Teske, J., Xuesong Wang, S., Wolfgang, A., et al. 2020, arXiv e-prints, arXiv:2011.11560, accepted for publication in ApJ Supplement Series
Thiabaud, A., Marboeuf, U., Alibert, Y., et al. 2014, A&A, 562, A27
Tinetti, G., Drossart, P., Eccleston, P., et al. 2016, Proceedings of SPIE: Space Telescopes and Instrumentation 2016: Optical, Infrared, and Millimeter Wave, 9904, 99041X
Turbet, M., Bolmont, E., Ehrenreich, D., et al. 2020, A&A, 638, A41
van der Walt, S., Colbert, S. C., & Varoquaux, G. 2011, Computing in Science and Engineering, 13, 22
Virtanen, P., Gommers, R., Oliphant, T. E., et al. 2020, Nature Methods, 17, 261
Weiss, L. M., Marcy, G. W., Petigura, E. A., et al. 2018, AJ, 155, 48
Wolf, E. T. 2017, ApJ, 839, L1
Zacharias, N., Finch, C. T., Girard, T. M., et al. 2012, VizieR Online Data Catalog, 1322
Zechmeister, M., Dreizler, S., Ribas, I., et al. 2019, A&A, 627, A49
Zechmeister, M. & Kürster, M. 2009, A&A, 496, 577
Zeng, L., Sasselov, D. D., & Jacobsen, S. B. 2016, ApJ, 819, 127
Zhu, C., Byrd, R. H., Lu, P., & Nocedal, J. 1997, ACM Transactions on Mathematical Software, 23, 550

Appendix A: Characterisation of the M-dwarf L 98-59 A

Appendix A.1: Atmospheric parameters of L 98-59 A: Detailed description of the different methods

On top of the derivation made by K19, we applied three different methods to derive the $T_{\rm eff}$, $\log g$ and [Fe/H] of L 98-59 A.

Appendix A.1.1: Spectral synthesis with SteParSyn

We employed the BT-Settl model grid (Allard et al. 2012), the radiative transfer code `turbospectrum` (Plez 2012) and a VALD3-based line list (Ryabchikova et al. 2015). Our selected set of synthetic spectra has stellar atmospheric parameters that span between 2600 and 4500 K in $T_{\rm eff}$, 4.0 to 6.0 dex in $\log g$, and -1 to +0.5 dex in [Fe/H]. In addition, we took into account the instrumental broadening by means of a Gaussian kernel (R = 140 000). We used the latest state-of-the-art version of the SteParSyn code (Tabernero et al. 2018; Tabernero et al. 2021) to infer the stellar parameters. We fitted the combined spectrum of L 98-59 A constructed using 61 ESPRESSO spectra (snr = 1063 at 7580 Å). We selected the TiO band system at 7050 Å alongside some Fe i and Ti i lines (see Marfil et al. 2020) to fit the observations. The latest version of SteParSyn relies on `emcee` (Foreman-Mackey et al. 2013), a Markov Chain Monte Carlo (mcmc) method used to fully sample the underlying distribution of the stellar parameters of L 98-59. Besides $T_{\rm eff}$, [Fe/H] and $\log g$ values shown in Table A.2, the method also provides an estimate for the quadratic sum of macroturbulence (ζ) and the stellar equatorial spin velocity projected on the plane of the sky ($v \sin i$): $\sqrt{\zeta^2 + (v \sin i)^2} = 3.78 \pm 0.44$ km s^{-1}.

Appendix A.1.2: Machine learning regression with odusseas

The odusseas software (Antoniadis-Karnavas et al. 2020) receives a 1D spectrum and its resolution as input. The pseudo equivalent widths are measured and used as input for a supervised machine learning algorithm (ridge regression model) which is used to derive the spectroscopic parameters $T_{\rm eff}$ and [Fe/H]. The implementation relies on the machine learning Python package `scikit learn`. The training and testing sets are taken from a reference sample of 65 HARPS spectra with associated $T_{\rm eff}$ and [Fe/H] derived by Casagrande et al. (2008) and Neves et al. (2012). When the spectra provided as input do not have the same resolution as the HARPS spectra from the reference sample, the spectra with the highest resolution are degraded (by convolution) to the lowest of the two resolutions. The estimates of $T_{\rm eff}$ and [Fe/H] result from the average of 100 determinations obtained by randomly shuffling and splitting the training and testing groups. The reported uncertainties are the wide uncertainties of the machine learning models at this resolution, after taking into consideration the intrinsic uncertainties of the reference sample parameters during the machine learning process. The estimates provided by this method are also reported in Table A.2.

Appendix A.1.3: Spectral energy distribution fitting with vosa

The VOSA (Bayo et al. 2008) online tools estimates the $T_{\rm eff}$, [Fe/H], $\log g$, extinction (A_V) and alpha enhancement by fitting the photometric SED with theoretical models. It also computes the total flux ($F_{\rm tot}$) by integrating over the best template and then uses the distance to infer the luminosity (L). VOSA offers a wide variety of stellar models. We chose the BT-Settl model (Allard et al. 2012) for its treatment of dust and clouds which is important for low mass stars. Due to the small distance of 10.6194 pc (inferred from GAIA parallaxes, Bailer-Jones et al. 2018), we fixed the extinction to 0. The photometric measurements used for the photometric SED are listed in Table A.1. The $T_{\rm eff}$, [Fe/H] and $\log g$ provided by this analysis are provided in Table A.2. Additionally, the fitting procedure inferred an alpha elements enhancement ([α/Fe]) of $-0.03^{+0.16}_{-0.13}$ dex and a luminosity of $L = 0.01128 \pm 0.00042\,L_\odot$.

Table A.1: Broad band photometry of L 98-59

Filter ID	Observed Flux [erg/s/cm^2/Å]
APASS.B	$3.139 \cdot 10^{-14} \pm 7.8 \cdot 10^{-16}$
SLOAN/SDSS.g	$5.208 \cdot 10^{-14} \pm 9.1 \cdot 10^{-16}$
GAIA/GAIA2.Gbp	$6.7184044482566 \cdot 10^{-14} \pm 0$
APASS.V	$7.91 \cdot 10^{-14} \pm 1.2 \cdot 10^{-15}$
SLOAN/SDSS.r	$1.08 \cdot 10^{-13} \pm 4.4 \cdot 10^{-15}$
GAIA/GAIA2.G	$1.4670979389511 \cdot 10^{-13} \pm 0$
GAIA/GAIA2.Grp	$2.1402666745903 \cdot 10^{-13} \pm 0$
WISE/WISE.W1	$1.376 \cdot 10^{-14} \pm 7.9 \cdot 10^{-16}$
WISE/WISE.W2	$4.744 \cdot 10^{-15} \pm 9.2 \cdot 10^{-17}$
AKARI/IRC.S9W	$4.95 \cdot 10^{-16} \pm 2.1 \cdot 10^{-17}$
WISE/WISE.W3	$1.357 \cdot 10^{-16} \pm 2.0 \cdot 10^{-18}$
WISE/WISE.W4	$1.190 \cdot 10^{-17} \pm 5.2 \cdot 10^{-19}$

Appendix A.1.4: K19 approach

K19 estimated $T_{\rm eff}$ and $\log g$ from two mostly independent derivations. $T_{\rm eff}$ was derived using the Stefan-boltzman law. The required bolometric luminosity was estimated from V and K band photometry using empirical bolometric correction relations (Pecaut & Mamajek 2013; Mann et al. 2015, erratum). For the radius, they used $0.312 \pm 0.014\,R_\odot$ derived from the mass-luminosity relation of Benedict et al. (2016) and the mass-radius relation of Boyajian et al. (2012). [Fe/H] was derived from sed fitting (Stassun et al. 2017; Stassun & Torres 2016). This procedure also yielded an estimate of $T_{\rm eff}$, which was compatible within one sigma with the previous one, but was not preferred by the authors.

Appendix A.1.5: Choice of the adopted set of atmospheric parameter

Table A.2: Different approaches to the spectroscopic parameters of L 98-59

	$T_{\rm eff}$ [K]	[Fe/H] [dex]	$\log g$
SteParSyn	3415 ± 60	-0.46 ± 0.26	4.86 ± 0.13
ODUSSEAS	3280 ± 65	-0.34 ± 0.10	–
vosa	3362^{+140}_{-47}	-0.24 ± 0.51	4.88 ± 0.64
Stefan-Boltzman law + SED fitting (K19)	3367 ± 150	-0.5 ± 0.5	–

Notes. The adopted estimates are provided in Table 3.
– indicates that $\log g$ is not estimated by these methods.

Table A.2 compiles the four estimates of the spectroscopic parameters of L 98-59 A obtained with the four approaches presented above. It makes sense to separate them in two groups: the VOSA and K19 estimates, which rely on the photometric SED, on one side and the spectral synthesis and machine learning estimates, which rely on the high-resolution ESPRESSO spectra, on the other. For $T_{\rm eff}$, the SED based estimates are similar, both in terms of best values and uncertainties. They are both compatible within one sigma with the two ESPRESSO based estimates. However the latter are 2.5 times more precise. The ESPRESSO based estimates provide similar uncertainties, but are only compatible at 2.25 sigma. We do not currently know of any study that demonstrates the higher accuracy of one of the two ESPRESSO based approaches for M stars. Consequently, we do not exclude any of these estimates as an obvious outlier. However, given the data in hand, the spectral synthesis and machine learning uncertainties appear to be underestimated. For [Fe/H], the four estimates are compatible within 1.6 sigma. As expected, the spectral synthesis and machine learning methods provide more precise estimates with uncertainties up to five times better. Finally, the two $\log g$ estimates provided by the spectral synthesis and VOSA approaches are compatible within 1 sigma. The spectral synthesis method provides a more accurate estimate thanks to the use of high spectral resolution data.

In this paper, which focuses on the characterization of the planets in the L 98-59 system, we need to conclude with one final set of $T_{\rm eff}$, [Fe/H] and $\log g$ estimates. In order to keep a physically self-consistent set of estimates, we decided to use as final best values for the three spectroscopic parameters, the best values inferred by one method. The use of high-resolution spectroscopy data, which offers the possibility to characterize directly the chromospheric lines, is clearly an asset to infer [Fe/H] and $\log g$ compared to the use of the photometric SED. The larger wavelength coverage towards the infra-red offered by the SED can provide important constraints for the inference of $T_{\rm eff}$. However, the $T_{\rm eff}$ estimates provided by the SED based methods include the estimates of the high spectral resolution based methods within 1 sigma. We thus decided to use one of the two high spectral resolution based method to obtain our set of best values. We chose the spectral synthesis method, because of the lack of benchmark analysis demonstrating the accuracy of the relatively recent machine learning approach and the fact that it does not provide an estimate for $\log g$. The only exception is for the uncertainties on the $T_{\rm eff}$ that we identified as underestimated. We chose to enlarge this uncertainty to encompass the best values provided by the other three methods within one sigma leading to the adopted values and uncertainties provided in Table 3.

Appendix A.2: Stellar modeling: mass, radius and age

The derivation of the radius of L 98-59 A is already presented in details in Section 3.2, but for the derivation its mass, we again used several methods. The first method relies on our estimate of $\log g$ (see Section 3.1), which combined with our radius estimates, provides a mass of $0.241^{+0.097}_{-0.069}\,M_\odot$. The second relies on the stellar density retrieved by K19 from the fit of the transits of the three transiting planets. Combined with our radius estimates, it provides a mass of $0.311^{+0.10}_{-0.081}\,M_\odot$. Our third method relies on the mass-luminosity relation in the K band of Mann et al. (2019). From the absolute K magnitude of 6.970 ± 0.019 mag, obtained from the observed magnitude provided by the 2MASS catalog (Cutri et al. 2003) and the distance provided by the Gaia collaboration (Bailer-Jones et al. 2018), we obtain a mass of $0.290 \pm 0.020\,M_\odot$. The fourth approach is based on the recently published studies of M dwarfs by Cifuentes et al. (2020, see in particular Table 6). The authors performed a comprehensive analysis of 1843 nearby, bright low mass star using SED photometry. They derived bolometric luminosities, effective temperature, radius and mass for this sample. The masses are based on Schweitzer et al. (2019). They thus provide an equivalence between absolute bolometric luminosity, effective temperature, radius and mass. Our bolometric luminosity estimate would indicate a radius of $0.343 \pm 0.082\,R_\odot$ and a mass of $0.338 \pm 0.087\,M_\odot$. Our effective temperature estimate would indicate a radius of $0.433 \pm 0.086\,R_\odot$ and a mass of $0.432 \pm 0.090\,M_\odot$. For our fifth approach, we used the VOSA online tools already used in Appendix A.1.3. VOSA derives the stellar mass of $0.273 \pm 0.030\,M_\odot$ by comparing the measured $T_{\rm eff}$ and bolometric luminosity to evolutionary tracks (BT-Settl model Allard et al. (2012) for consistency with our analysis of the photometric SED). Finally, K19 provided an estimate of the mass of $0.313 \pm 0.014\,M_\oplus$ using a mass-luminosity relation for M dwarfs of Benedict et al. (2016). They derived the luminosity from K band observations.

Table A.3: Mass, Radius and density of L 98-59 derived by different approaches

Method	M_* [$M_\odot$]	R_* [$R_\odot$]	ρ_* [$\rho_\odot$]
Stefan-Boltzmann law		$0.303^{+0.026}_{-0.023}$	
$\log g + R_*$	$0.241^{+0.097}_{-0.069}$	//	$8.5^{+4.1}_{-2.1}$
$\rho_* + R_*$	$0.311^{+0.10}_{-0.081}$	//	$11.2^{+2.1}_{-1.7}$
VOSA	0.273 ± 0.030	–	$9.8^{+3.1}_{-1.5}$
Cifuentes+20 ($f(L)$)	0.338 ± 0.087	0.343 ± 0.082	$8.2^{+11}_{-3.1}$
Cifuentes+20 ($f(T_{\rm eff})$)	0.432 ± 0.090	0.433 ± 0.086	$5.3^{+5.2}_{-1.7}$
mass-lum (Mann et al. 2019)	0.290 ± 0.020	–	$10.4^{+3.1}_{-1.5}$
K19	0.313 ± 0.014	0.312 ± 0.014	$10.3^{+1.6}_{-0.89}$

Notes. The adopted estimates are provided in Table 3.
// indicates that the radius estimate used as input of the method is the one provided by the Stefan-Boltzmann law.
– indicates that the radius is not estimated by the method and that we are using the estimate provided by the Stefan-Bolztmann law to compute the stellar density.

Table A.3 gathers all these estimates of the radius and mass of L 98-59 A. From these, we also computed the resulting stellar densities via Monte Carlo simulations. We drew 100,000 samples of stellar mass and radius from normal distributions with mean and standard deviation as provided by the estimates from the corresponding row of Table A.3. When the error bars were asymmetric, we used the average of the upper and lower uncertainties as standard deviation. From these 100,000 samples, we computed 100,000 stellar density values. We then computed the estimate of the stellar density using the 50th, 16th and 84th percentiles. The relative precision on the stellar density provides us with a lower limit on the relative precision that we can achieve for the planetary density (see Table 3). The absolute value of the stellar density will also impact the measured planetary densities and thus is of particular interest for the modeling of their interior (see Section 5.3). All stellar density estimates agree within one sigma. However, when looking at the dispersion of best values, the one inferred from Cifuentes et al. (2020) using the $T_{\rm eff}$ is clearly off. The associated mass and radius are also significantly above all others. This might be due to the scale of the Cifuentes et al. (2020) study. The table from which we derive our estimates is a summary of the properties of around 2000 stars, which might be relevant for a large sample, but might fail to accurately represent a specific case like L 98-59 A. We thus discarded this estimate. We also note that the Cifuentes et al. (2020) estimates based on the bolometric luminosity (instead of the $T_{\rm eff}$) is in good agreement with the others.

The remaining radius estimates agree within 1 sigma, but their uncertainties vary by a factor of up to $\sim$ 6, between the K19 estimate and the one from Cifuentes et al. (2020) based on the bolometric luminosity. As already mentioned in the previous paragraph, due to the scale of the Cifuentes et al. (2020) study, their uncertainties are probably overestimated. The uncertainties of the other two estimates differ by less than a factor two. We adopted the values derived from the Stefan-Boltzmann law since they are based on first principles.

The mass estimates also agree within one sigma, but their uncertainties vary by a factor of up to $\sim$ 10. Compared with the dispersion of the best values, the K19 uncertainty appears to be underestimated. The $\log g$ and stellar density based values and the Cifuentes et al. (2020) uncertainties appear, on the contrary, overestimated. In between the two remaining estimates, VOSA and Mann et al. (2019), we adopted the one derived with VOSA. The VOSA tools provided $T_{\rm eff}$, [Fe/H] and $\log g$ values in good agreement with the one we adopted. We also used VOSA to derive the bolometric luminosity used to derive L 98-59 A radius. The VOSA mass estimate thus provides a physically consistent set of stellar parameters. The final set of adopted values and uncertainties are provided in Table 3.

To determine the age of L 98-59 A, we used the accurate photometry and distance provided by Gaia. We constructed the color-magnitude diagram shown in Fig 1, where we also depicted the well known, empirically determined mean sequences of stellar members of the β Pictoris moving group ($\sim$20 Myr, Miret-Roig et al. 2020), the Tucana-Horologium moving group ($\sim$45 Myr, Bell et al. 2015), the Pleiades open cluster ($\sim$120 Myr, Gossage et al. 2018), and the field (possible ages in the range 0.8–10 Gyr). These sequences were taken from Luhman (2018) and Cifuentes et al. (2020) and were derived by employing Gaia data; therefore, the direct comparison with L 98-59 A is feasible without any systematic effect. From its location in the Gaia color-magnitude diagram, we infer that L 98–59 has a likely age consistent with that of the "field" (our target lies below the mean field sequence of M dwarfs). We did not correct L 98–59 A data for interstellar extinction because from its optical and infrared photometry (Table A.1) and optical HARPS and ESPRESSO spectroscopy there is no evidence of strong or anomalous absorption. The "field" age is consistent with the measured mass and radius of the star, and the actual position of L 98-59 A below the bottom borderline of the 1-σ dispersion of the field sequence also agrees with a slightly sub-solar metallicity. Finally the kinematics of L 98-59 A can also provide indications about its age. Using the RV systemic velocity, the Gaia parallax, the RA/DEC coordinates and proper motions, we derived the UVW velocities of L 98-59 A (see Table A.4). L 98-59 A appears to belong to the thin disk and does not belong to any know young moving group. Therefore, it is kinematically older than the oldest moving group currently known, i.e. its age is above 800 Myr.

Table A.4: Kinematics of L 98-59 A

U	15.42 ± 0.22 km s^{-1}
V	10.31 ± 1.06 km s^{-1}
W	-2.59 ± 0.34 km s^{-1}
P(thick)	2 %
P(thin)	98 %
P(halo)	0 %
Group membership	Thin disk

Notes. U, V, W are the three velocity components in the solar reference frame. P(thin), P(thick) and P(halo) are the probability of L 98-59 A to belong to the thin disk, the thick disk and the galactic halo respectively.

Appendix B: Radial velocities and activity indicators measurements

Table B.1 provides the measurements of the RVs and activity indicators from the ESPRESSO spectrograph used in this paper. For the RVs and activity indicators measurements from the HARPS spectrograph, we refer the reader to C19.

Appendix C: Rotational modulation in photometric time series

In order to address the presence of stellar activity induced modulation in the TESS data, we first attempted to fit the LC with GP and mean offsets for each sector. The GP was implemented with the `celerite` Python package, as in Section 2.2, but this time the functional form of the kernel was designed to model quasi-periodic signal. Its equation is

$$k(\tau) = \frac{B}{2+C} e^{-\tau/L} \left[\cos\left(\frac{2\pi\,\tau}{P_{\rm rot}}\right) + (1+C) \right], \tag{C.1}$$

and is taken from Foreman-Mackey et al. (2017, eq. 56). $P_{\rm rot}$ is an estimator of the stellar rotation period, L is the correlation timescale, B is a positive amplitude term and C is a positive factor. We performed the fit by maximizing the log likelihood with `emcee`. We used 32 walkers. For each walkers, we first maximized the log likelihood using the L-BFGS-B algorithm (Morales & Nocedal 2011; Zhu et al. 1997; Byrd et al. 1995) implemented in the `scipy.optimize` Python package. Then we performed a first exploration of 5000 iterations followed by a second exploration of 10 000 iterations starting at the last positions of the first one.

The *posterior* PDF of the main hyper parameters (B, L and P_{rot}) are presented in Fig C.1. The rotation period is poorly constrained (190^{+189}_{-134} days). It's also worth noticing that the retrieved amplitude and timescales are low: $0.11^{+0.05}_{-0.01}$ ppm for the amplitude and $6.3^{+2.6}_{-1.0}$ days for the timescales. In particular, $\frac{L}{P_{rot}}$ appears too low to be physical, since the timescale is expected to be of the same order of magnitude or higher than the rotation period (Angus et al. 2018; Haywood et al. 2014). The timescale and the amplitude are strongly correlated. The low timescale and amplitude can thus be tentatively explain by a this degeneracy which would results in a strong underestimation of both quantities.

Due to the poor determination of the rotation period, we used the GLSP as a more model independent approach to the question of the presence of rotational modulation in the TESS LC. TESS is designed for high precision relative photometry (as opposed to high precision absolute photometry). The photometry can thus suffer from offsets between each sector which would

Table B.1: ESPRESSO RV, FWHM, BIS, Contrast, S_{index}, H_α, *NaD*, *Ca II H & K* indexes, $\log R'_{\text{HK}}$ and BERV measurements for L 98-59

BJD_{TDB} - 2 400 000 days	RV m s^{-1}	σ_{RV} m s^{-1}	FWHM km s^{-1}	σ_{FWHM} km s^{-1}	BIS m s^{-1}	σ_{BIS} m s^{-1}	Contrast	σ_{Contrast} ...	...	Inst.
58436.80567402998	-5573.322521	0.803703	4499.159260	1.607407	20.138559	1.607407	42.799022	0.015291	...	Pre
58444.83918777015	-5576.670284	0.792801	4498.863898	1.585603	19.679371	1.585603	42.598489	0.015014	...	Pre
58463.82528164983	-5579.975907	0.646632	4507.424364	1.293264	20.459179	1.293264	42.763800	0.012270	...	Pre
58470.77212886	-5578.914555	0.657531	4503.113471	1.315063	16.920078	1.315063	42.714825	0.012474	...	Pre

The full table is available in electronic form at the CDS ....

Notes. σ_X represents the one sigma error bar measured for the quantity X.
Inst. stands for instrument and indicates if a measurement has been taken before or after the technical intervention on ESPRESSO (see Section 2.1.2).

Table C.1: Photometric offset derived for each TESS sectors

Sector	Offset [%]
2	$1.771^{+0.021}_{-0.022}$
5	$0.774^{+0.021}_{-0.022}$
8	$0.303^{+0.021}_{-0.020}$
9	$-0.007^{+0.023}_{-0.020}$
10	$-0.976^{+0.019}_{-0.019}$
11	$-2.170^{+0.017}_{-0.020}$
12	$-0.186^{+0.020}_{-0.020}$
28	$0.736^{+0.019}_{-0.022}$
29	$-0.847^{+0.021}_{-0.023}$

impact strongly the GLSP of the LC. We thus used the offsets derived from our GP fit (see Table C.1) to re-align the different sectors before computing the GLSP. As the retrieved offsets are several orders of magnitude higher than the amplitude of the GP signal, we can assume that they are independent of the exact model used to describe the stellar activity (hyper parameters and choice of kernel). The result of the GLSP analysis is presented in Fig 3 and discussed in Section 3.4.

Appendix D: Choices of priors

The *prior* PDF used for the analyses made in Section 4.1.1, 4.1.2 and 4.2 are provided in Table 3 (column *prior*). In this appendix, we explain the reasons behind the choice of each *prior*.

Appendix D.1: Priors used for the TESS LC analysis (Section 4.1.1)

For the instrumental *prior*, the TESS additive jitter term (σ_{TESS}), we adopted a uniform distribution between zero and five times the median value of the reported error bars.

The orbital parameters $e\cos\omega$ and $e\sin\omega$ were assigned a joint *prior*. A joint *prior* consists in a transformation between two sets of parameters to define the *prior* on the new set of parameters instead. In this case, $e\cos\omega$ and $e\sin\omega$ are converted into e and ω. For the *prior* PDF of e, as recommended by Kipping (2013), we used a Beta distribution with the following values for the two shape parameters: $a = 0.867$ and $b = 3.03$. For the *prior* PDF of ω, we used a uniform distribution between $-\pi$ and π. The remaining planetary parameters, P, t_{ic}, R_p/R_* and $\cos i_p$ werw also assigned a joint *prior*. This joint *prior*, that we call transiting *prior*, also includes the stellar density ρ_*. Its main objective is to exclude regions of the parameter space where the three transiting planets are not transiting. It performs two changes of coordinates. It first compute the impact parameter (b) from P, ρ_* and $\cos i_p$ (assuming a circular orbit), effectively converting the parameter $\cos i_p$ into b. Then it computes the orbital phase (ϕ) from P and t_{ic}. For this conversion, we need to define a reference time which corresponds to $\phi = 0$. We chose this reference time to be the floored value of the first ESPRESSO observation, $t_{\text{ref}} = 1436$ BTJD. Then $t_{\text{ic}} = t_{\text{ref}} + P\phi$. We thus transformed the set of parameters ρ_*, P, t_{ic}, R_p/R_* and $\cos i_p$ into the new set of parameters ρ_*, P, ϕ, R_p/R_* and b. To ρ_*, we assigned as *prior* the *posterior* of the K19 analysis. To P, we assigned a Jeffreys distribution between 0.1 day and the time span of the RV observations (~ 520 days). To avoid degenerate values of t_{ic} separated by a multiple of the period, we chose as *prior* a uniform distribution between zero and one for ϕ. For R_p/R_*, we assigned a uniform distribution between 10^{-3} and 1. For the *prior* of b, we used a uniform distribution between 0 an 2, in order to allow grazing transiting, but we imposed the condition that $b < 1 + R_p/R_*$ to ensure that the configuration is transiting.

Finally, for the *prior* on the limb darkening coefficients, we used Gaussian PDFs whose first two moments were defined using the Python package `ldtk`[11] (Parviainen & Aigrain 2015). Using a library of synthetic stellar spectra, it computes the limb darkening profile of a star, observed in a given spectral bandpass (specified by its transmission curve), and defined by its T_{eff}, $\log g$ and [Fe/H]. Provided the values and error bars for these stellar parameters (see Section 3.1) and the spectral bandpass of TESS, `ldtk` uses a Markov chain Monte Carlo (MCMC) algorithm to infer the mean and standard deviation of the Gaussian PDFs for the coefficients of a given limb-darkening law (non-linear in our case). `ldtk` relies on the library of synthetic stellar spectra generated by Husser et al. (2013). It covers a wavelength range, from 500 Å to 5.5 μm , and a stellar parameter space delimited by: $2\,300\,\text{K} \leqslant T_{\text{eff}} \leqslant 12\,000\,\text{K}$, $0.0 \leqslant \log g \leqslant +6.0$, $-4.0 \leqslant [\text{Fe/H}] \leqslant +1.0$, and $-0.2 \leqslant [\alpha/\text{Fe}] \leqslant +1.2$. This parameter space is well within the requirements of our study (see Table A.2).

Appendix D.2: Priors used for the RV analysis (Section 4.1.2)

Regarding the instrumental *priors*, the *prior* PDF of the offsets between the RV instruments ($\Delta\text{RV}_{HARPS/\text{pre}}$, $\Delta\text{RV}_{\text{post/pre}}$) are Gaussian distributions with means equal to the difference of the median values of the data sets and variances equal to the sum of their variances. The *prior* PDFs of the constant levels of the FWHM (C_{pre}, C_{post}, C_{HARPS}) are Gaussian distributions with means equal to the median values of each data set and variances

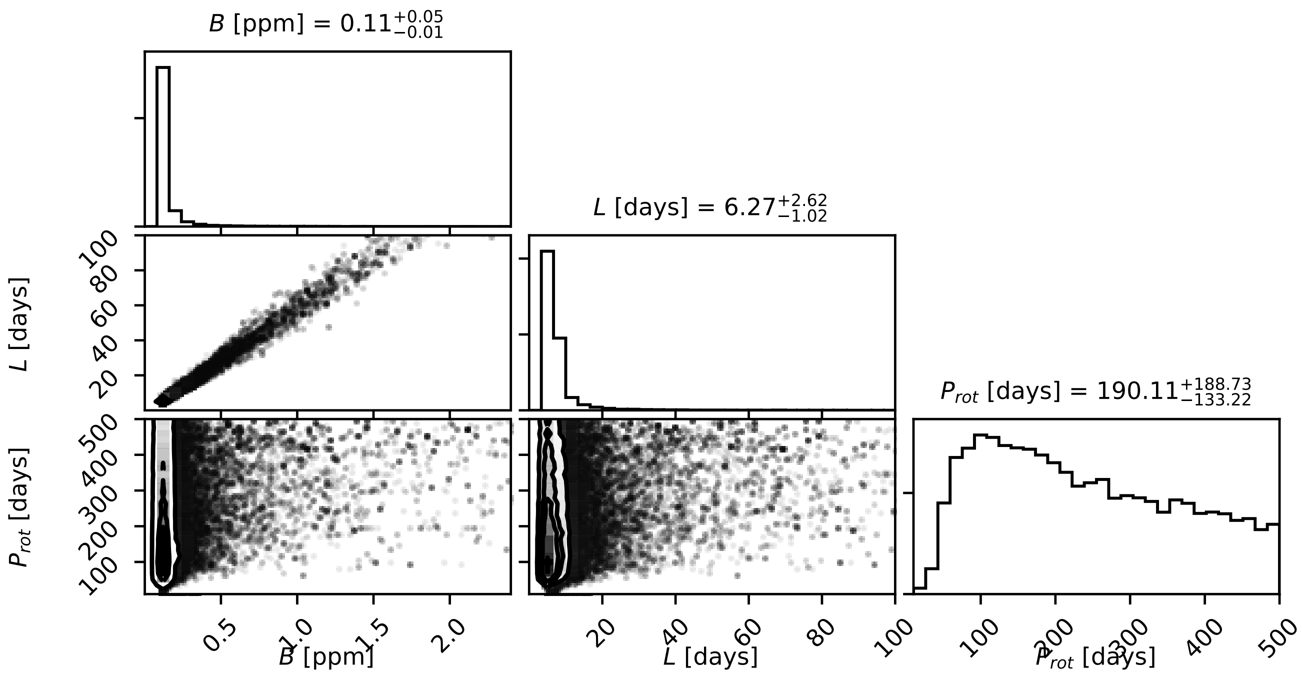

Fig. C.1: *posterior* distributions of the main hyper parameters of the rotational kernel (Equation (C.1))

equal to their variances. The *prior* PDF of the additive jitter parameters ($\sigma_{RV,\mathrm{pre}}$, $\sigma_{RV,\mathrm{post}}$, $\sigma_{RV,HARPS}$, $\sigma_{FWHM,\mathrm{pre}}$, $\sigma_{FWHM,\mathrm{post}}$, $\sigma_{FWHM,HARPS}$) are uniform distributions between zero and five times the median values of the reported error bars for each data set.

Regarding the star related *prior*s, the *prior* PDF of the systemic velocity (v_0) is a Gaussian with the mean equal to the median value of the RV data taken by ESPRESSO before the fiber change and a variance equal to its variance. The other parameters are the hyper-parameters of the quasi-periodic kernels. The *prior* PDFs of the two amplitudes (A_{RV}, A_{FWHM}) are uniform between zero and the maximum of the peak-to-peak values of the joint data sets taken by the three instruments. For the period of recurrence (P_{rot}), the *prior* PDF chosen is a Jeffreys distribution between 5 days and the time span of our observations ($\sim$ 520 days). Given the age and the spectral type of L 98-59, 5 days appears to be a good lower limit for the rotation period. This *prior* encompasses comfortably the estimate of $\sim$ 80 days made by C19 based on the periodogram of the H_α measurements. For the decay time scale (τ_{decay}), we chose a Jeffreys distribution between 2.5 days and five times the time span of observations. This upper limit is set to prevent the GP to produce stellar activity models that would be completely coherent over the time span of our observations. In other words, we imposed that the stellar activity signal is quasi-periodic and not periodic. The objective is to avoid that the GP reproduces planetary signals. Furthermore, we imposed the decay time-scale to be superior to half of the period of recurrence. This condition, suggested by Angus et al. (2018) and Haywood et al. (2014), prevents the GP to produce stellar activity signals that are too incoherent and thus close to white-noise. In such cases, the GP signal and the additive jitter terms starts to become degenerate. The *prior* PDF of the periodic coherence scale (γ) is uniform between 0.05 and 5. The typical value for γ in the literature is thought to be 0.5 (Dubber et al. 2019). This *prior* is designed to explore one order of magnitude below and above this typical values.

Regarding the planetary *prior*s, the *prior* PDF of K is uniform between 0 and the maximum of the peak-to-peak values of the RV data sets taken by the three instruments. For the ephemerides parameters (P and t_{ic}) and for the three known transiting planets, we used as *prior*s the *posterior*s of our analysis of the TESS LC (see notes ‡ at the end of Table 3).

For the non-transiting planets that we identified in the GLSP, we used a joint *prior*. This joint *prior* converts P and t_{ic} into P and ϕ similarly to what was done within the transiting joint *prior* in Appendix D.1. The reference time used, which corresponds to $\phi = 0$, is the same ($t_{\mathrm{ref}} = 1436$ BTJD). We chose a uniform distribution between zero and one for ϕ. For P, we used a Jeffreys distribution between 0.1 day and the time span of the RV observations ($\sim$ 520 days). Finally, the last two parameters are $e \cos \omega$ and $e \sin \omega$. We used the same joint *prior* than in Appendix D.1 which results in a Beta distribution with shape parameters $a = 0.867$ and $b = 3.03$ for the *prior* PDF of e (Kipping 2013), and a uniform distribution between $-\pi$ and π for ω.

Appendix D.3: Priors used for the joint analysis of the RV and LC data (Section 4.2)

The *prior*s used for this analysis are the same than the one used for the analysis of the TESS LC (see Appendix D.1). For the parameters that are not present in this analysis, we used the same *prior*s than the ones used for our analysis of the RV data (see Appendix D.2). All *prior*s are mentioned in Table 3.

Appendix E: Searching for the transits of planet e and planetary candidate 05

We searched the TESS data for previously unreported planetary transit signal including planet e and planetary candidate 05. We used a procedure similar to Barros et al. (2016). For this analysis, we did not use the LC detrended with a GP described in

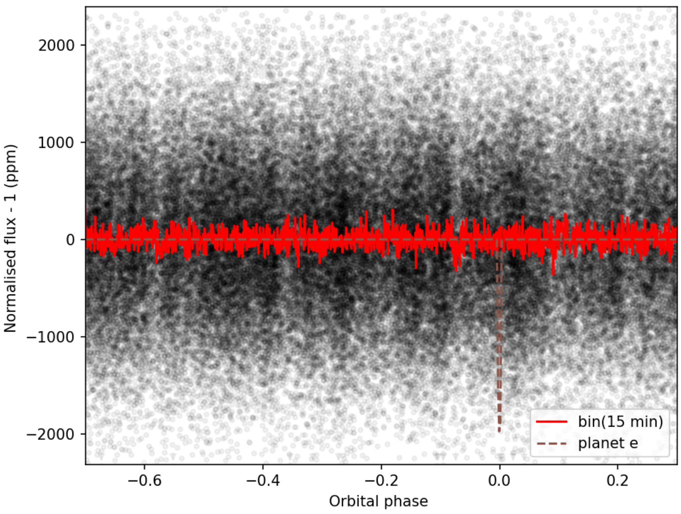

(a) Planet e

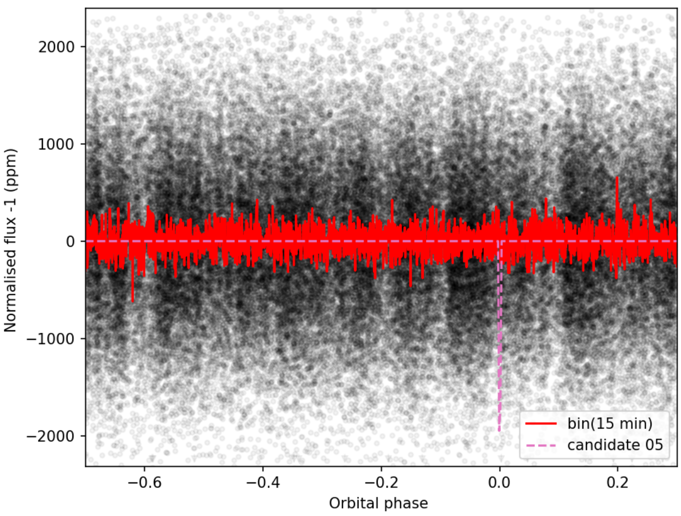

(b) Candidate 05

Fig. E.1: Phase folded TESS LC assuming the best model ephemerides of planet e (a) and planetary candidate 05 (b). The black points are the TESS data point at the original cadence. The red line is the data binned in phase using bins of 15 min. The pink and brown dashed lines are the expected transit signal assuming that the planets have the same radius than planet d (see Table 3).

Section 2.2 since the flexibility of the GP could alter the transit signals. Instead we detrended each sector separately by dividing the LC by a spline interpolation of third degree. We used a knot every 0.5 days. Combined with an iterative 3 sigma clipping to identify outliers, it allows to better preserve unidentified transits signals in the detrended LC (Barros et al. 2016). Then we removed the transits of the three known transiting planets by cutting out data within a window of 2 transit durations centered on the predicted transit time. The extra 0.5 transit duration before and after transit allows to account for errors in the ephemerides or unknown transit timing variations. After, we performed a box least square (BLS) search (Kovács et al. 2002) checking for periodicities between 0.5 and 40 days. The resulting periodogram is shown in Fig E.2 with the highest peak corresponding to 1.049 days which is probably due to aliases linked to earth rotation. Phase folding the light-curve at this period does not show a typical transit signature. No other significant peaks are seen in the BLS periodogram including at the periods of the candidate planets detected in RV (see Section 4.1.3). We also performed a transit search using the TLS software (Hippke & Heller 2019) and obtained the same conclusion.

To confirm the absence of transit signal for planet e and planetary candidate 05, we phase-folded the TESS light-curve using the ephemeris of Table 3. In both cases, we do not observe any transit signal. We show that if the planetary radii are similar to the other transiting planets, the transit signal would have been clear in the TESS LC.

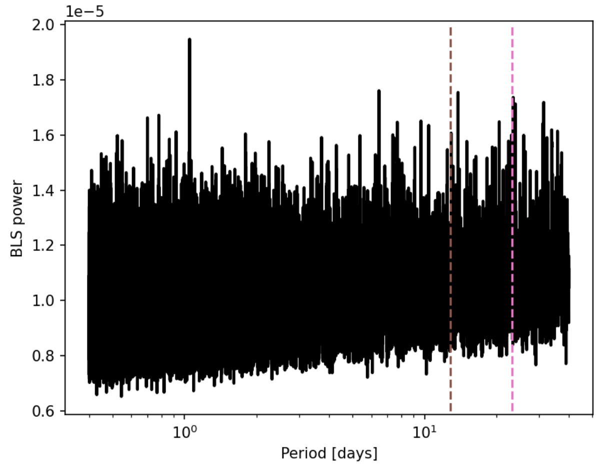

Fig. E.2: Periodogram provided by the BLS search in the TESS-data. The pink and brown dashed vertical linked indicated the orbital period of planet e and planetary candidate respectively. There is no significant power at these periods.

Appendix F: Evidence for additional planets in the L 98-59 system

As mentioned in Section 4.1.3, in order to assess the presence of additional planets in the L 98-59 system, we first performed the two analyses which include only the three previously known planets. Fig F.1 and F.2 follow the same format than Fig 4 and 5. Fig F.1 shows the RV time series including the data from both instruments, the best three planets plus activity model and the residuals of this fit. Fig F.2 displays the GLSP of the combined RV data and the residuals, the GLSPs of the planetary and stellar activity model sampled at the same times as the RV time series and the WF. The GLSP of the combined RVs in Fig F.2 shows two narrow peaks with FAP below 0.1 % at the two periods, 13 and 23 days, previously identified as potential additional planetary signals. The GLSP of the residuals displays a narrow peak at 13 days.

The analyses with four planets converges towards a significant detection of the semi-amplitude of a fourth Keplerian signal. Fig 4 shows, similarly to Fig F.1, the time series, the best model and Fig 5 shows the GLSPs. We also performed an iterative GLSP analysis in Fig F.5. This allows to clearly see the peak on the GLSP corresponding to planet b which is invisible in other figures. The GLSP of the residuals after the subtraction of the model for planet b (also shown in Fig 5) shows two peaks around 1.743 and 2.341 days and no peak around 23 days. The analysis of the TESS LC did not show transit signals at 1.743 or 2.341 days, so we did not pursue the planetary origin for these

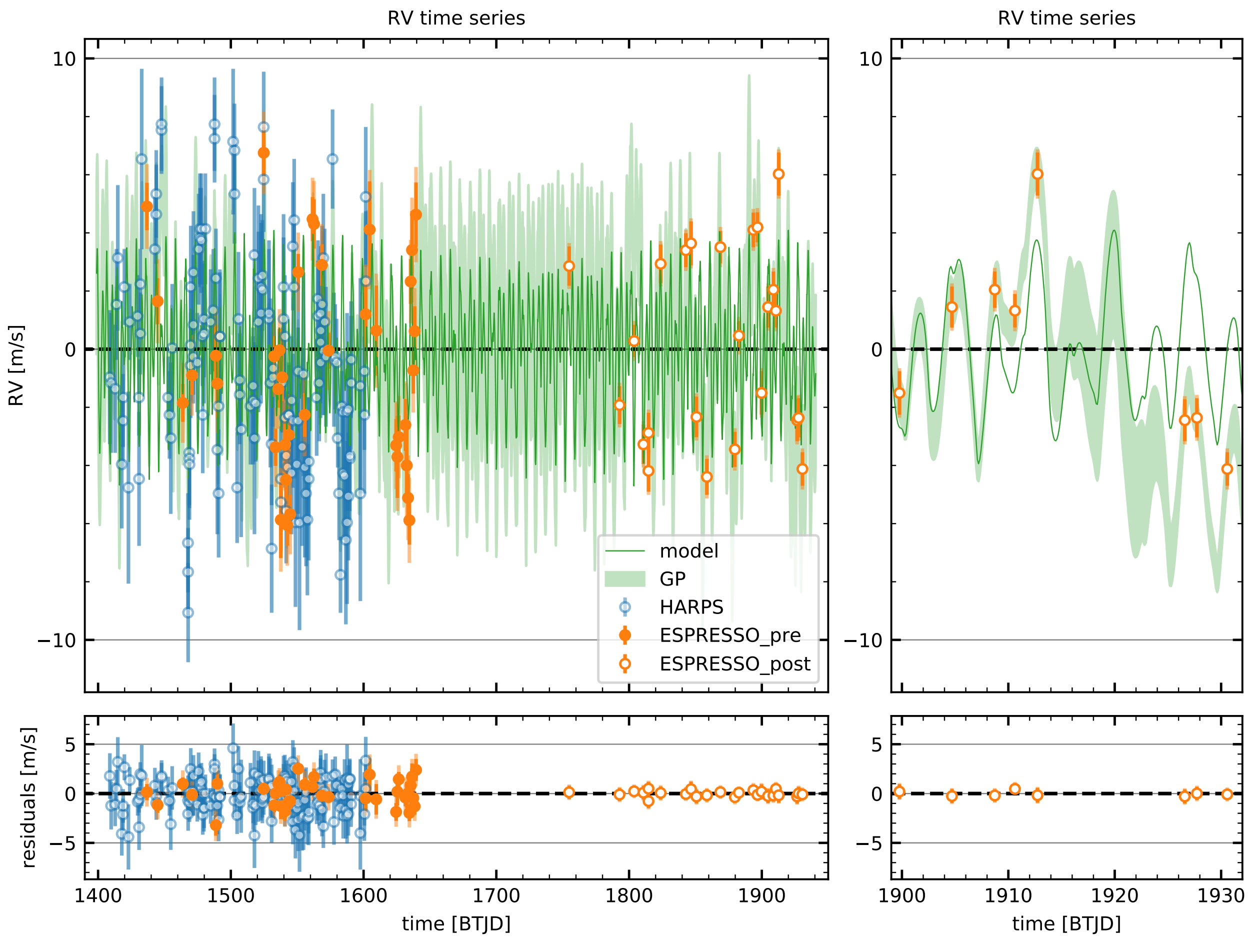

Fig. F.1: Outcome of the fit of the three planets model: The format of this figure is identical to the one used in Fig 4 but is described again here for convenience. (Top-Left) RV time series along with the best model (solid green line) which include the planetary signals and best prediction from the GP stellar activity model. The one sigma uncertainties from the GP prediction are also displayed (shaded green area). For this plot, we subtract from the RV data the systemic velocity and the instruments offsets (see values in Table 3). (Bottom-left) Time series of the residuals of the best model. (Right) Zoom on a small portion of the time series for a better visualization of the short time-scale variations.

peaks. However the GLSP of the activity model does show a peak around 23 days. This indicates that the signal at 23 days might be generated by stellar activity. Thanks to our stellar activity model which analyzes the FWHM data simultaneously with the RV data, we can also analyze the behavior of this activity indicator. Fig F.3 and F.4 show similar information than Fig 4 and 5, but for the FWHM data. There is no significant power around 23 days neither in the GLSP of the combined FWHM data, nor in the ones of the stellar activity model and the residuals. Similarly, the GLSPs of all the other activity indicators (see Fig 2 and Fig 3) do not display significant power around 23 days. The analysis of the activity indicator does not confirm the stellar activity origin of the 23 days signal.

Consequently, we performed other analyses with five planets. The fits converge towards a significant detection of the semi-amplitude of a fifth Keplerian signal. Fig F.6 and F.7 show the time series, the best model and the GLSPs. The GLSP of the stellar activity model still displays power around 23 days, but less significant and a much more flattened profile compared with the four planets analyses (Fig 5).

Appendix G: Internal composition of three transiting super-earths

As explained in Section 5.3, our framework for the modelling of the interior of the three transiting planets is composed a forward model and a Bayesian retrieval.

In the forward model, each planet is made of four layers: an iron/sulfur inner core, a mantle, a water layer and a gas layer. We used for the core the Equation of State (EOS) of Hakim et al. (2018), for the silicate mantle, the EOS of Sotin et al. (2007), and the water EOS is taken from Haldemann et al. (2020). These three layers constitute the 'solid' part of the planets. The thickness of the gas layer (assumed to be made of pure H/He) is computed as a function of the stellar age, mass and radius of the solid part, and irradiation from the star, using the formulas of Lopez & Fortney (2014).

In the Bayesian analysis part of model, we proceed in two steps. We first generated 150000 synthetic stars, their mass, radius, effective temperature, age and composition ([Si/H], [Fe/H] and [Mg/H]), as well as the associated error bars, being taken at random following the stellar parameters quoted above. For each of these stars, we generated 1000 planetary systems, varying the internal structure parameters of all planets, and assuming that the

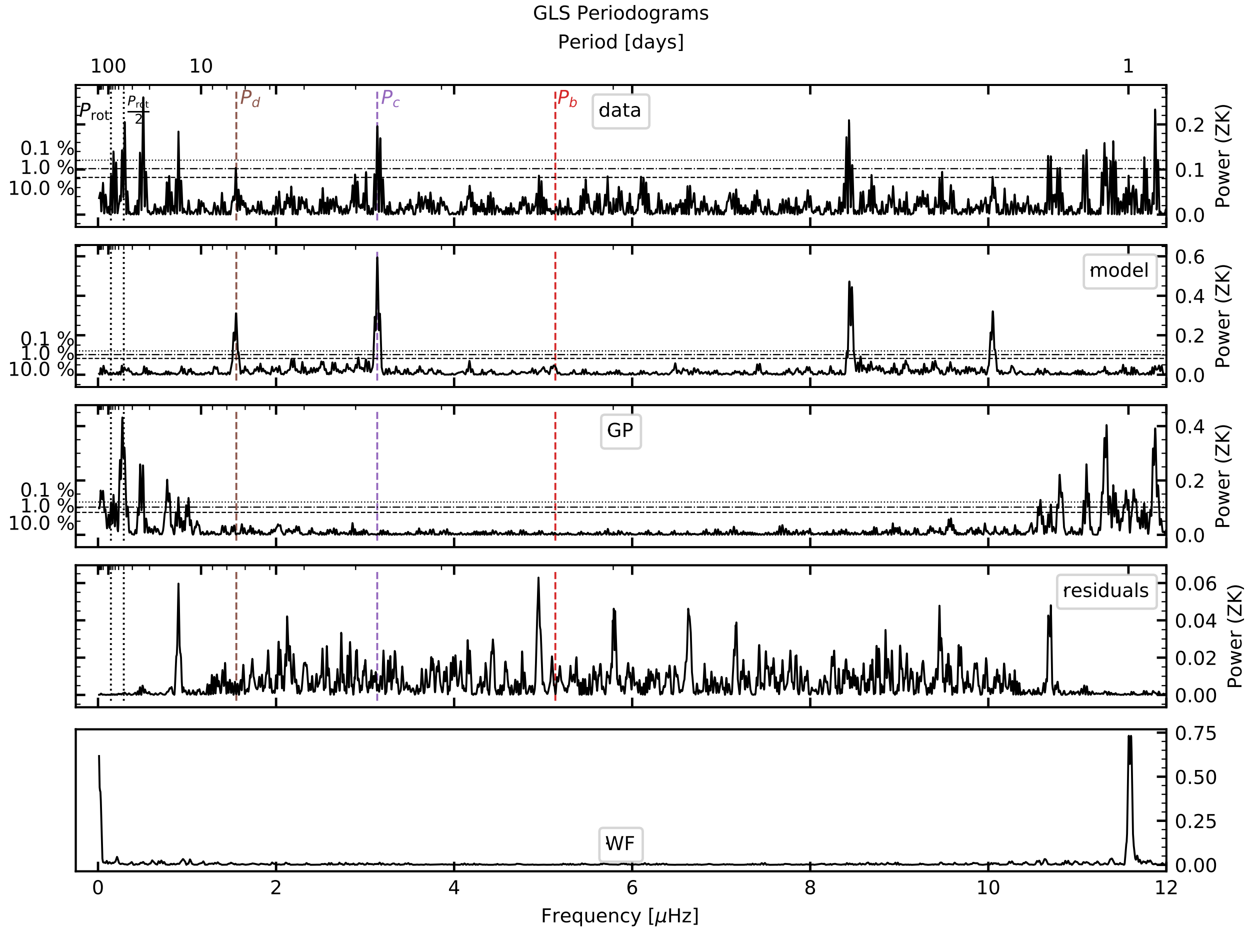

Fig. F.2: Outcome of the fit of the three planets model: The format of this figure is identical to the one used in Fig 5 but is described again here for convenience. GLSPs of the RV time series (top) and of the planetary (second) and stellar activity (third) models sampled at the same times as the RV data. GLSP of the time series of the residuals (fourth) and the window function (bottom). The vertical lines on the GLSPs correspond to the orbital periods of planets b, c, d, half and the full rotation period (estimated at 80 days) from right to left.

bulk Fe/Si/Mg molar ratios are equal to the stellar ones. We then computed the transit depth and RV semi-amplitude for each of the planets, and retained models that fit the observed data within the error bars. With this procedure, we include the fact that all synthetic planets orbit a star with exactly the same parameters. Indeed, planetary masses and radii are correlated by the fact that the fitted quantities are the transit depth and RV semi-amplitude, which depend on the stellar radius and mass. In order to take into account this correlation, it is therefore important to fit the planetary system at once, and not each planet independently.

The *prior*s used in the Bayesian analysis are the following: the mass fraction of the gas envelope is uniform in log, the mass fraction (relative to the solid planet, so excluding the mass of gas) of the inner core, mantle and water layer are uniform on the simplex (the surface on which they add up to one). Finally, we constrain the mass fraction of water to be 50 % at most (Thiabaud et al. 2014; Marboeuf et al. 2014). The molar fraction of iron in the inner core is uniform between 0.5 and 1, and the molar fraction of Si, Mg and Fe in the mantle is uniform on the simplex (they add up to one).

The *posterior* distributions of the most important parameters (mass fractions, composition of the mantle) of each planets in L 98-59 are shown in Fig G.1 to G.3.

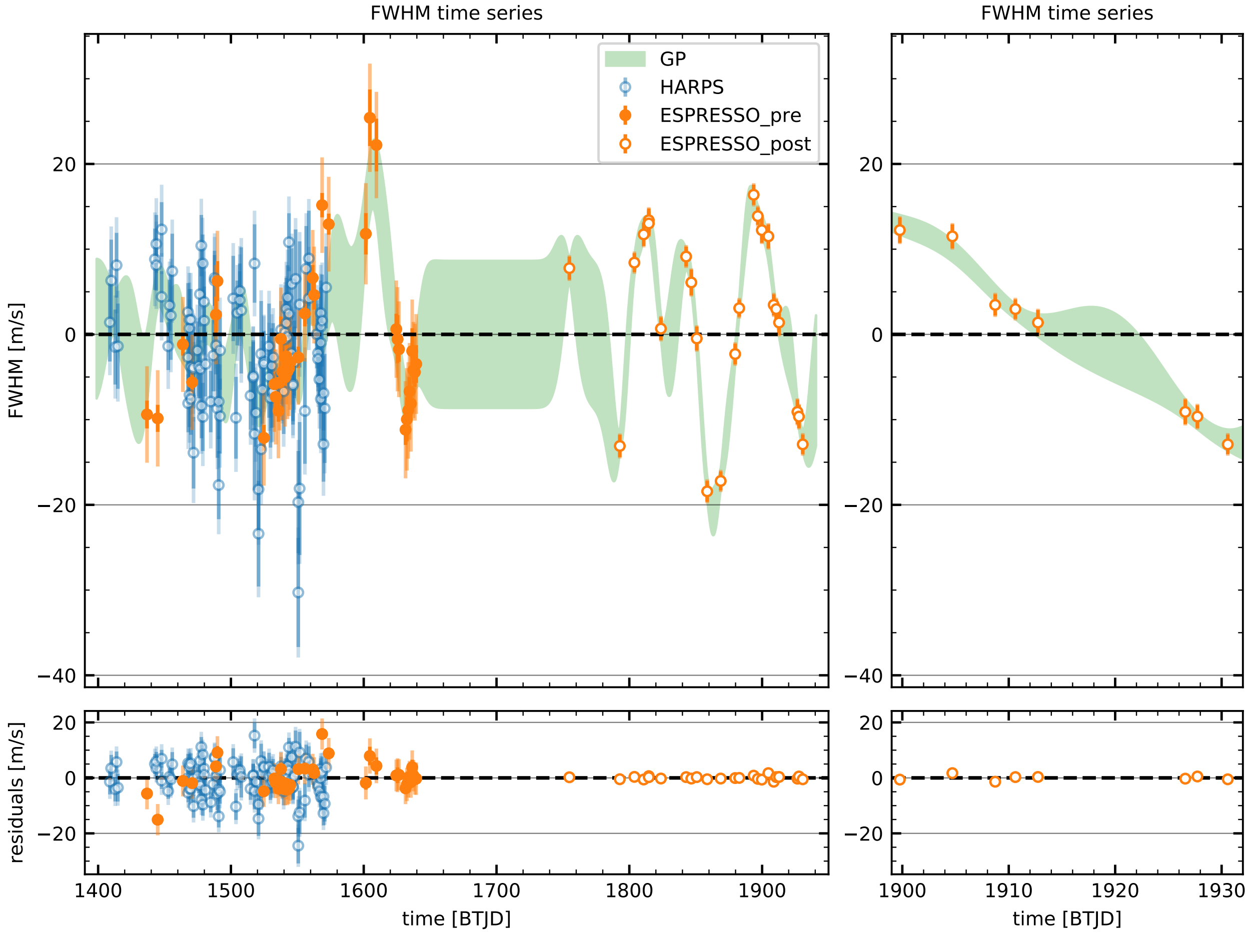

Fig. F.3: Outcome of the fit of the four planets model regarding the FWHM: The structure of this figure is similar to Fig 4 or Fig F.1 except that the FWHM data and model are displayed instead of the RV ones.

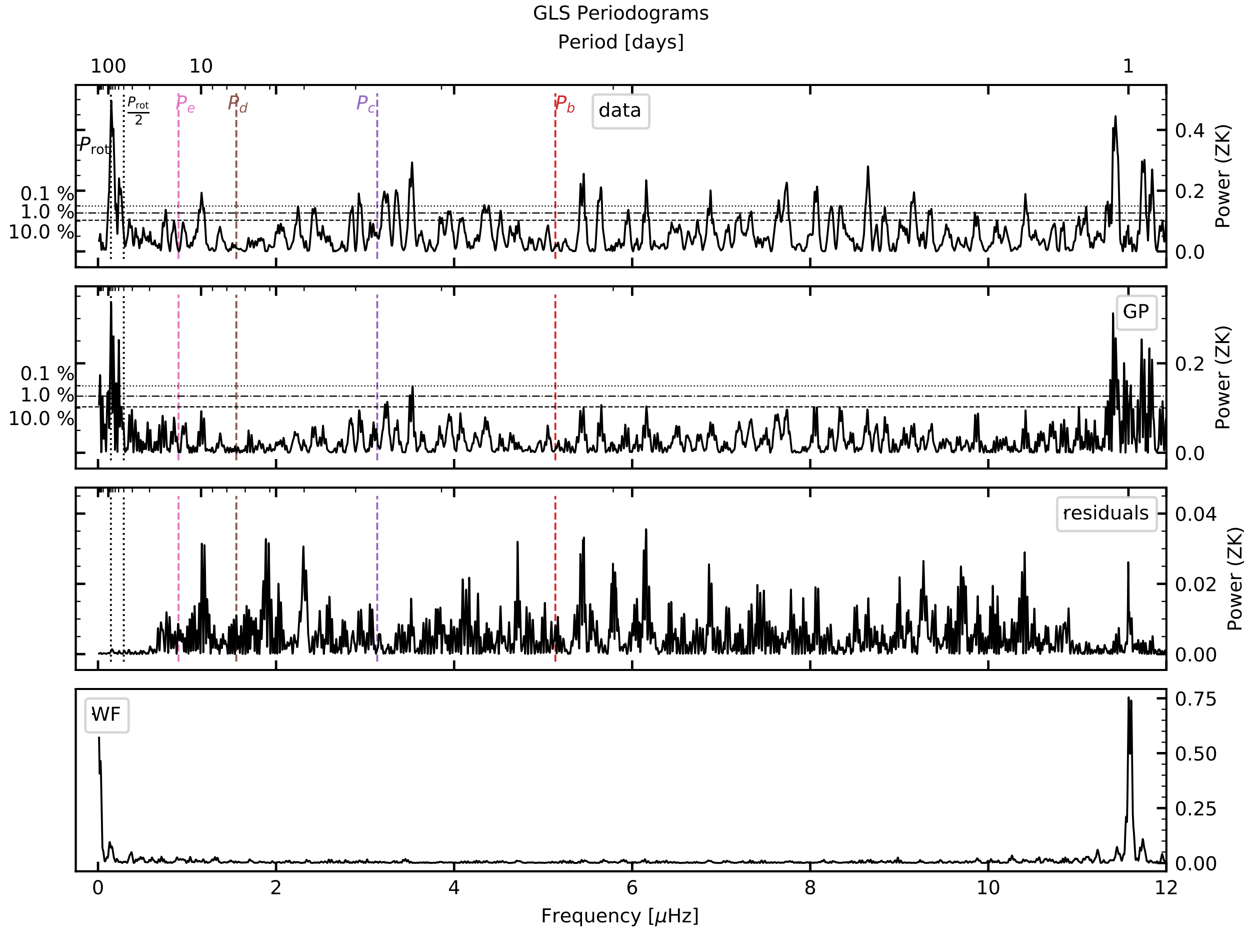

Fig. F.4: Outcome of the fit of the four planets model regarding the FWHM: The structure of this figure is similar to Fig 5 or Fig F.2 except that the FWHM data and model are displayed instead of the RV ones.

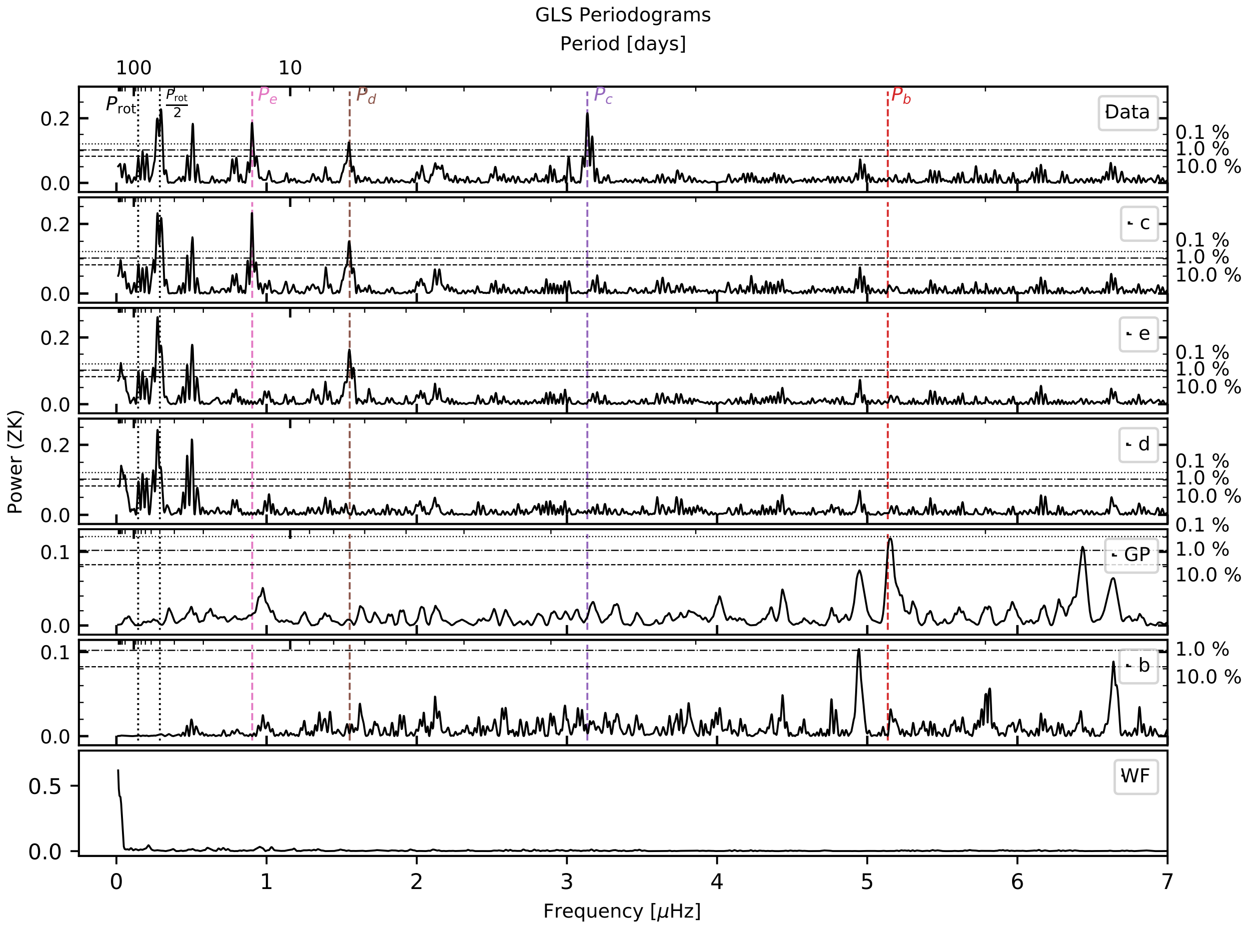

Fig. F.5: Iterative GLSP for the four planets model: GLSP of the RV data (top) and the window function (bottom). The GLSPs of the data shown in the previous row minus the model for planet c, e, d, the stellar activity model and the model for planet b are displayed in the second, third, fourth, fifth and sixth row respectively.

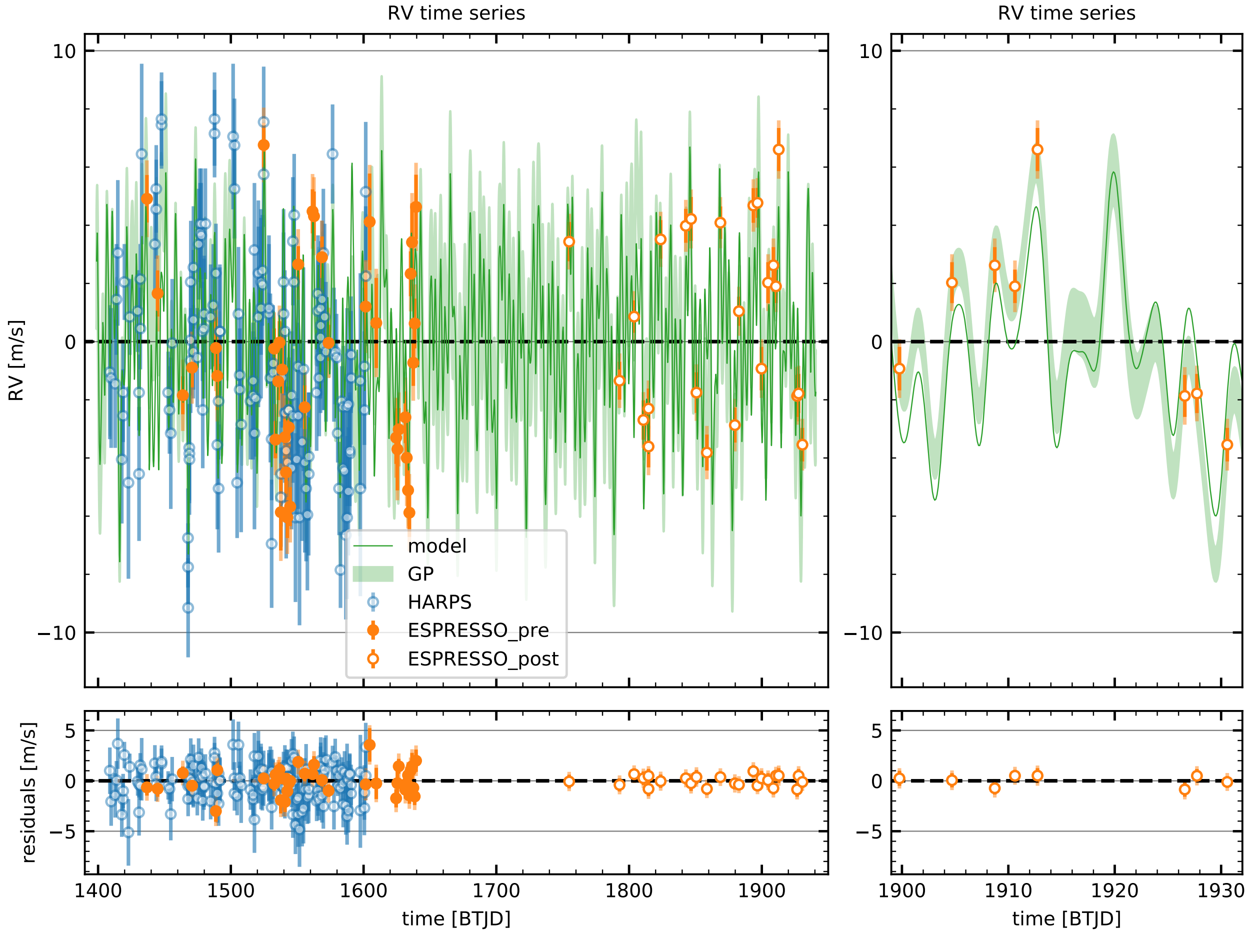

Fig. F.6: Outcome of the fit of the five planets model: The format of this figure is identical to the one used in Fig 4 and Fig F.1.

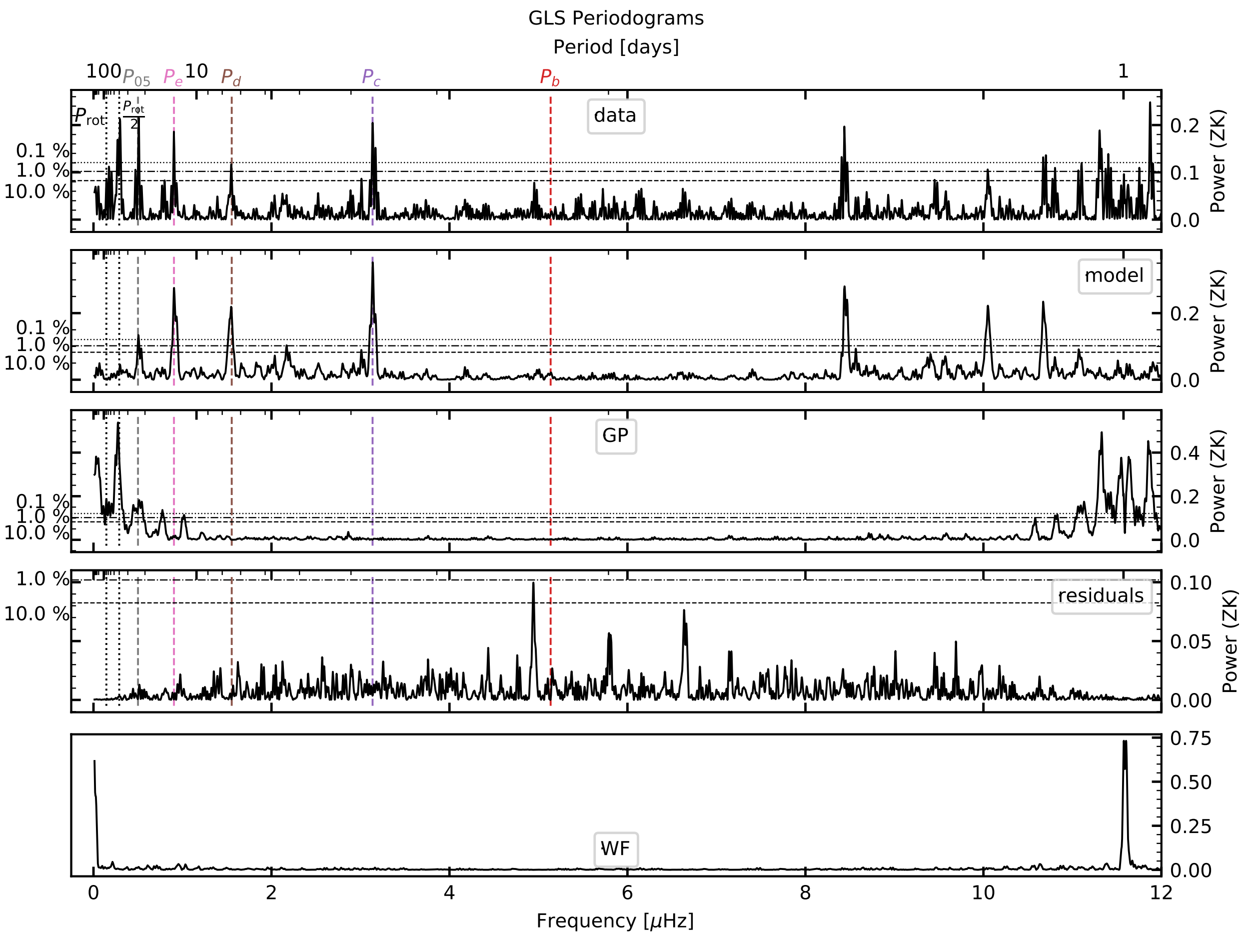

Fig. F.7: Outcome of the fit of the five planets model: The format of this figure is identical to the one used in Fig 5 and Fig F.2.

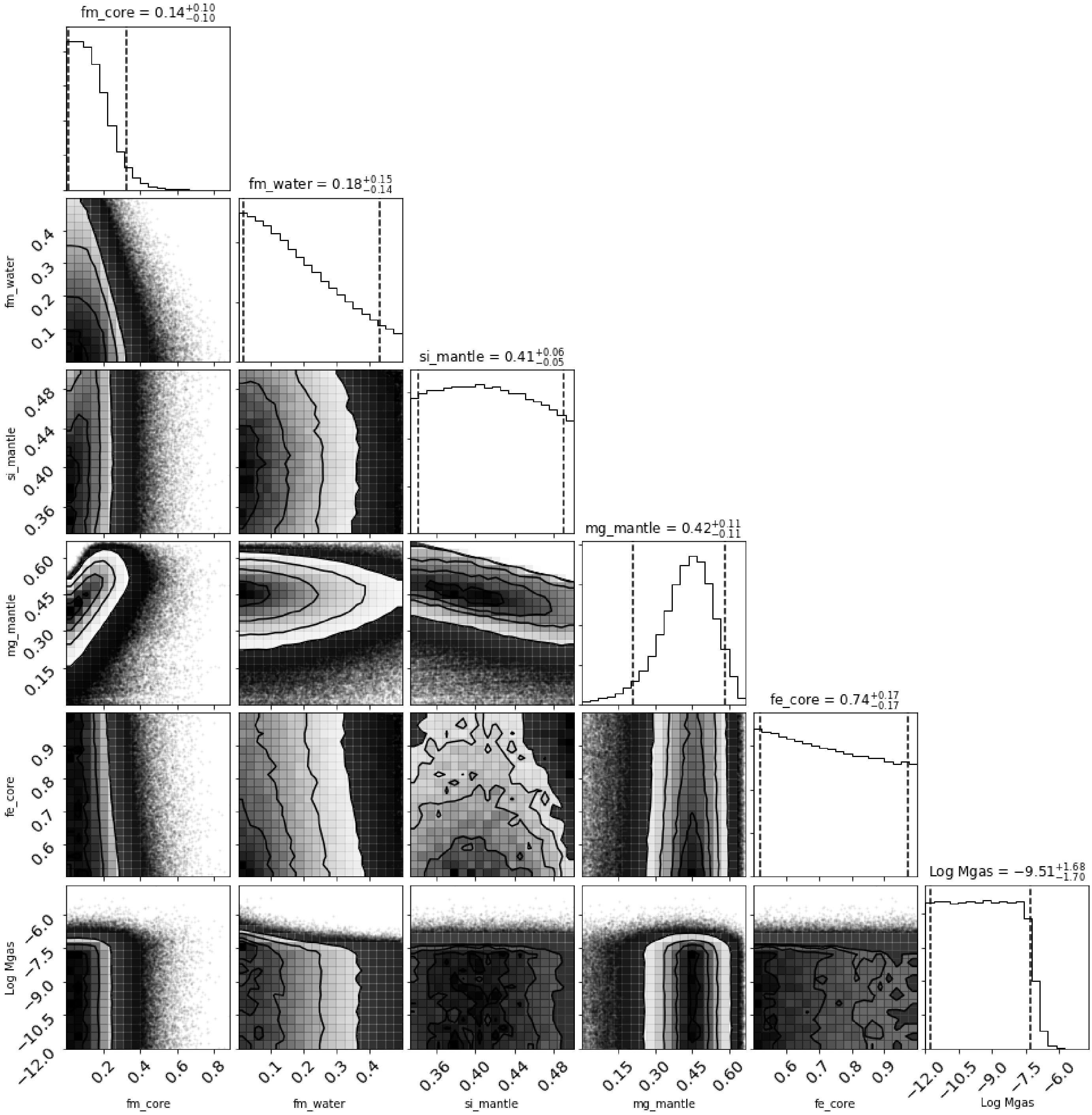

Fig. G.1: Corner plot showing the main internal structure parameters of L 98-59 b. Shown are the mass fraction of the inner core, the mass fraction of water, the Si and Mg mole fraction in the mantle, the Fe mole fraction in the inner core, and the mass of gas (log scale). The values on top of each column are the mean and 5% and 95% quantiles.

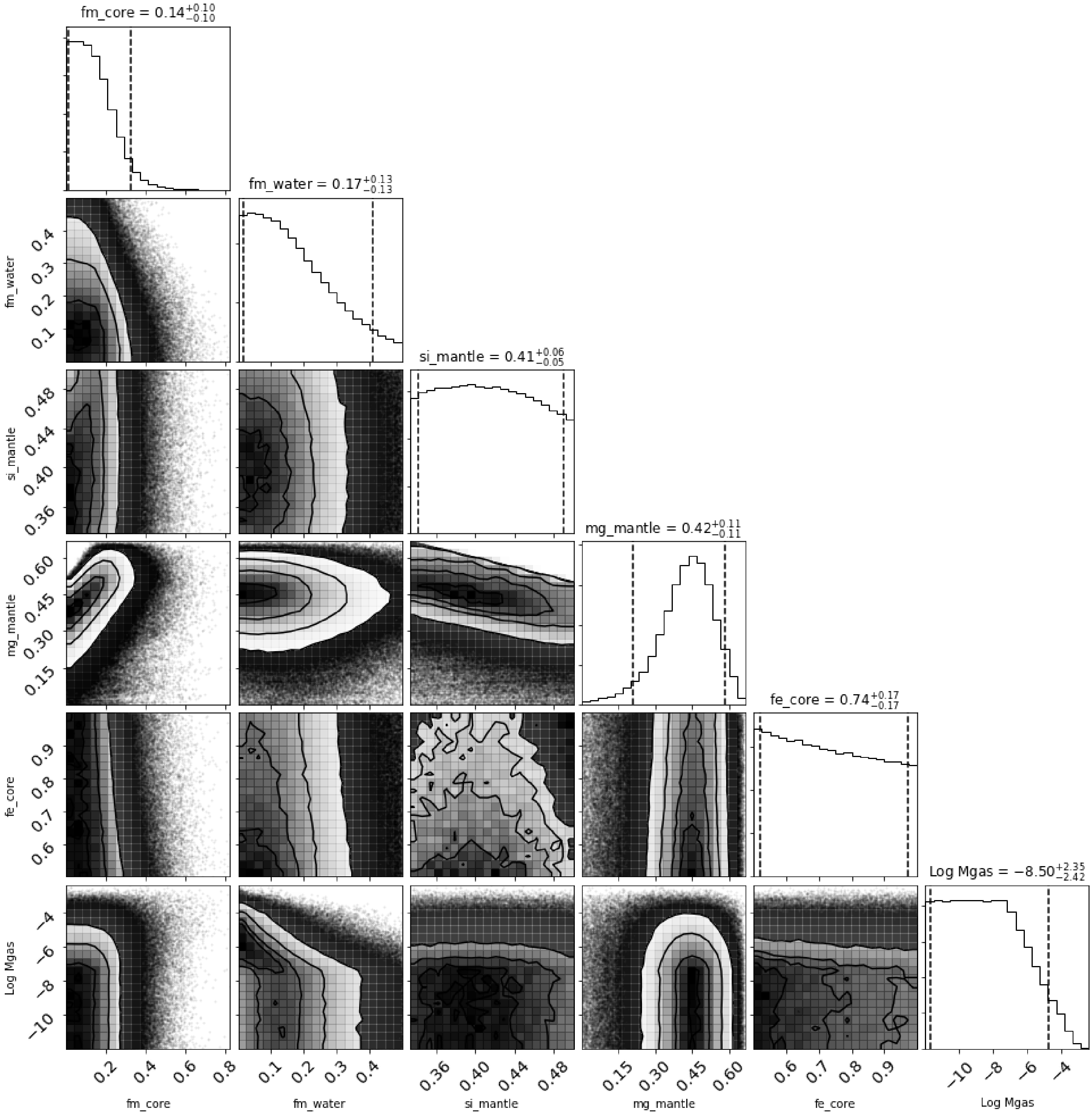

Fig. G.2: Same as Fig. G.1 for L 98-59 c.

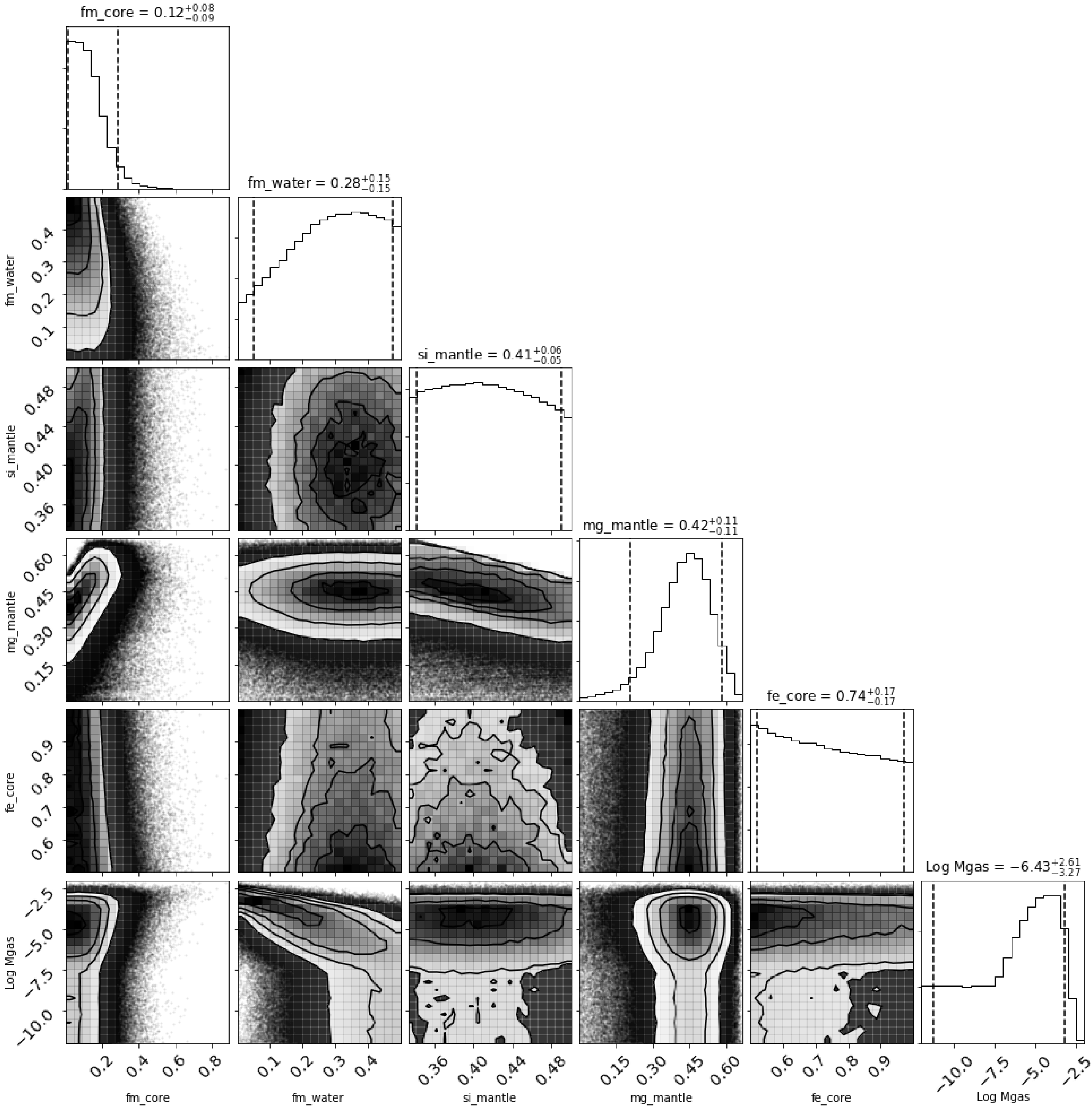

Fig. G.3: Same as Fig. G.1 for L 98-59 d.

Table 3: **Parameters' estimates of the planetary system L 98-59**

	Posterior	Prior	Source
Planetary parameters			
Planet b			
M_p [M$_\oplus$]	$0.40^{+0.16}_{-0.15}$		
R_p [R$_\oplus$]	$0.850^{+0.061}_{-0.047}$		
ρ_p [g.cm^{-3}]	$3.6^{+1.4}_{-1.5}$		
$T_{\rm eq}$ [K]	627^{+33}_{-36}		
$P^\bullet$ [days]	$2.2531136^{+1.2e-06}_{-1.5e-06}$	$\mathrm{JP_{transiting}}(P : \mathcal{J}(0.1, 520))$	
$t_{\rm ic}^\bullet$ [BJD$_{\rm TDB}$ - 2 457 000]	$1366.17067^{+0.00036}_{-0.00033}$	$\mathrm{JP_{transiting}}(\phi : \mathcal{U}(0, 1))$	
a [AU]	$0.02191^{+0.00080}_{-0.00084}$		
e	$0.103^{+0.117}_{-0.045}$		
ω_* [°]	192^{+70}_{-155}		
$M_{\rm ref}$ ¶ [radians]	$2.7^{+1.9}_{-1.7}$		
i_p [deg]	$87.71^{+1.16}_{-0.44}$		
$e\cos\omega_*^\bullet$	$-0.027^{+0.099}_{-0.144}$	$\mathrm{JP}_{e\cos\omega_*, e\sin\omega_*}(e : \beta(0.867, 3.03),$	
$e\sin\omega_*^\bullet$	$-0.028^{+0.090}_{-0.072}$	$\omega_* : \mathcal{U}(-\pi, \pi))$	
$K^\bullet$ [m s^{-1}]	$0.46^{+0.20}_{-0.17}$	$\mathcal{U}(0, 17)$	
$R_p/R_*^\bullet$	$0.02512^{+0.00072}_{-0.00064}$	$\mathrm{JP_{transiting}}(R_p/R_* : \mathcal{U}(10^{-3}, 1))$	
$\cos i_p^\bullet$	$0.0400^{+0.0076}_{-0.0203}$	$\mathrm{JP_{transiting}}(b : \mathcal{U}(0, 2))$	
a/R_*	$15.0^{+1.4}_{-1.0}$		
b	$0.53^{+0.14}_{-0.22}$		
$D14$ [h]	$0.992^{+0.090}_{-0.032}$		
$D23$ [h]	$0.928^{+0.075}_{-0.032}$		
F_i [$F_{i,\oplus}$]	$24.7^{+5.0}_{-4.1}$		
H [km]	430^{+290}_{-110}		
Planet c			
M_p [M$_\oplus$]	$2.22^{+0.26}_{-0.25}$		
R_p [R$_\oplus$]	$1.385^{+0.095}_{-0.075}$		
ρ_p [g.cm^{-3}]	$4.57^{+0.77}_{-0.85}$		
$T_{\rm eq}$ [K]	553^{+27}_{-26}		
$P^\bullet$ [days]	$3.6906777^{+1.6e-06}_{-2.6e-06}$	$\mathrm{JP_{transiting}}(P : \mathcal{J}(0.1, 520))$	
$t_{\rm ic}^\bullet$ [BJD$_{\rm TDB}$ - 2 457 000]	$1367.27375^{+0.00013}_{-0.00022}$	$\mathrm{JP_{transiting}}(\phi : \mathcal{U}(0, 1))$	
a [AU]	$0.0304^{+0.0011}_{-0.0012}$		
e	$0.103^{+0.045}_{-0.058}$		
ω_* [°]	261^{+20}_{-10}		
$M_{\rm ref}$ ¶ [radians]	$5.83^{+0.19}_{-0.65}$		
i_p [deg]	$88.11^{+0.36}_{-0.16}$		
$e\cos\omega_*^\bullet$	$-0.014^{+0.027}_{-0.022}$	$\mathrm{JP}_{e\cos\omega_*, e\sin\omega_*}(e : \beta(0.867, 3.03),$	
$e\sin\omega_*^\bullet$	$-0.099^{+0.056}_{-0.046}$	$\omega_* : \mathcal{U}(-\pi, \pi))$	
$K^\bullet$ [m s^{-1}]	$2.19^{+0.17}_{-0.20}$	$\mathcal{U}(0, 17)$	
$R_p/R_*^\bullet$	$0.04088^{+0.00068}_{-0.00056}$	$\mathrm{JP_{transiting}}(R_p/R_* : \mathcal{U}(10^{-3}, 1))$	

Continued on next page

Table 3 – *Continued from previous page*

	Posterior	Prior	Source
$\cos i_p{}^{\bullet}$	$0.0330^{+0.0028}_{-0.0062}$	$\mathrm{JP}_{\mathrm{transiting}}(b : \mathcal{U}(0, 2))$	
a/R_*	$19.00^{+1.20}_{-0.80}$		
b	$0.601^{+0.081}_{-0.066}$		
$D14$ [h]	$1.346^{+0.122}_{-0.069}$		
$D23$ [h]	$1.167^{+0.125}_{-0.050}$		
F_i [$F_{i,\oplus}$]	$12.8^{+2.6}_{-2.1}$		
H [km]	184^{+43}_{-23}		
Planet d			
M_p [M$_\oplus$]	$1.94^{+0.28}_{-0.28}$		
R_p [R$_\oplus$]	$1.521^{+0.119}_{-0.098}$		
ρ_p [g.cm^{-3}]	$2.95^{+0.79}_{-0.51}$		
T_{eq} [K]	416^{+20}_{-20}		
$P^{\bullet}$ [days]	$7.4507245^{+8.1e-06}_{-4.6e-06}$	$\mathrm{JP}_{\mathrm{transiting}}(P : \mathcal{J}(0.1, 520))$	
$t_{\mathrm{ic}}{}^{\bullet}$ [BJD$_{\mathrm{TDB}}$ - 2 457 000]	$1362.73974^{+0.00031}_{-0.00040}$	$\mathrm{JP}_{\mathrm{transiting}}(\phi : \mathcal{U}(0, 1))$	
a [AU]	$0.0486^{+0.0018}_{-0.0019}$		
e	$0.074^{+0.057}_{-0.046}$		
ω_* [°]	180^{+27}_{-50}		
M_{ref} ¶ [radians]	$3.76^{+0.66}_{-0.61}$		
i_p [deg]	$88.449^{+0.058}_{-0.111}$		
$e\cos\omega_*{}^{\bullet}$	$-0.062^{+0.057}_{-0.061}$	$\mathrm{JP}_{e\cos\omega_*, e\sin\omega_*}(e :$ $\beta(0.867, 3.03),$	
$e\sin\omega_*{}^{\bullet}$	$0.000^{+0.032}_{-0.026}$	$\omega_* : \mathcal{U}(-\pi, \pi))$	
$K^{\bullet}$ [m s^{-1}]	$1.50^{+0.22}_{-0.19}$	$\mathcal{U}(0, 17)$	
$R_p/R_*{}^{\bullet}$	$0.0448^{+0.00106}_{-0.0010}$	$\mathrm{JP}_{\mathrm{transiting}}(R_p/R_* : \mathcal{U}(10^{-3}, 1))$	
$\cos i_p{}^{\bullet}$	$0.0271^{+0.0019}_{-0.0010}$	$\mathrm{JP}_{\mathrm{transiting}}(b : \mathcal{U}(0, 2))$	
a/R_*	$33.7^{+1.9}_{-1.7}$		
b	$0.922^{+0.059}_{-0.059}$		
$D14$ [h]	$0.84^{+0.15}_{-0.20}$		
$D23$ [h]	$0.51^{+0.23}_{-0.18}$		
F_i [$F_{i,\oplus}$]	$5.01^{+1.02}_{-0.83}$		
H [km]	195^{+37}_{-37}		
Planet e			
$M_p \sin i$ [M$_\oplus$]	$3.06^{+0.33}_{-0.37}$		
T_{eq} [K]	342^{+20}_{-18}		
$P^{\bullet}$ [days]	$12.796^{+0.020}_{-0.019}$	$\mathrm{JP}_{P,t_{\mathrm{ic}}}(P : \mathcal{N}(12.8, 1), \phi : \mathcal{U}(0, 1))$	
$t_{\mathrm{ic}}{}^{\bullet}$ [BJD$_{\mathrm{TDB}}$ - 2 457 000]	$1439.40^{+0.37}_{-0.36}$		
a^* [AU]	$0.0717^{+0.0060}_{-0.0048}$		
e	$0.128^{+0.108}_{-0.076}$		
ω_* [°]	165^{+40}_{-29}		
M_{ref} ¶ [radians]	$1.07^{+2.1}_{-0.49}$		
$e\cos\omega_*{}^{\bullet}$	$-0.106^{+0.095}_{-0.095}$	$\mathrm{JP}_{e\cos\omega_*, e\sin\omega_*}(e :$ $\beta(0.867, 3.03),$	
$e\sin\omega_*{}^{\bullet}$	$0.023^{+0.056}_{-0.070}$	$\omega_* : \mathcal{U}(-\pi, \pi))$	

Continued on next page

Table 3 – *Continued from previous page*

	Posterior	Prior	Source
$K^\bullet$ [m s^{-1}]	$2.01^{+0.16}_{-0.20}$	$\mathcal{U}(0, 17)$	
a/R_*	$49.8^{+3.9}_{-3.8}$		
	Planetary candidate 05		
$M_p \sin i$ [M$_\oplus$] §	$2.46^{+0.66}_{-0.82}$		
$T_{\rm eq}$ [K] §	285^{+18}_{-17}		
$P^\bullet$ [days] §	$23.15^{+0.60}_{-0.17}$	$\mathrm{JP}_{P,t_{\rm ic}}\ (P:\mathcal{N}(22.8, 1), \phi:\mathcal{U}(0, 1))$	
$t_{\rm ic}^\bullet$ [BJD$_{\rm TDB}$ - 2 457 000] §	$1435.4^{+2.5}_{-2.5}$		
a^* [AU] §	$0.1034^{+0.0042}_{-0.0044}$		
e §	$0.21^{+0.17}_{-0.11}$		
ω_* [°] §	-23^{+85}_{-76}		
$e\cos\omega_*^\bullet$ §	$0.08^{+0.15}_{-0.16}$	$\mathrm{JP}_{e\cos\omega_*, e\sin\omega_*}(e: \beta(0.867, 3.03),$	
$e\sin\omega_*^\bullet$ §	$-0.04^{+0.17}_{-0.16}$	$\omega_*:\mathcal{U}(-\pi, \pi))$	
$K^\bullet$ [m s^{-1}] §	$1.37^{+0.33}_{-0.43}$	$\mathcal{U}(0, 17)$	
a/R_* §	$73.3^{+7.3}_{-6.4}$		
Stellar parameters			
RA$^{\rm GAIA\text{-}CRF2}$ [hh:mm:ss.ssss]	08:18:07.89		GAIA-DR2
DEC$^{\rm GAIA\text{-}CRF2}$ [dd:mm:ss.ss]	-68:18:52.08		GAIA-DR2
Sp. Type	M3V		K19
V mag	11.685 ± 0.02		APASS DR9
Ks mag	7.101 ± 0.018		2MASS
J mag	7.9		2MASS
parallax [mas]	94.1385 ± 0.0281		GAIA-DR2
distance [pc]	10.6194 ± 0.0032		BJ18
M_* [M$_\odot$]	0.273 ± 0.030		
R_* [R$_\odot$]	$0.303^{+0.026}_{-0.023}$		
age [Myr]	> 800		
$\rho_*^\bullet$ [$\rho_\odot$]	$9.15^{+1.8}_{-1.4}$	$\mathrm{JP}_{\rm transiting}(\rho_*:\mathcal{N}(11.2, 1.9))$	
L_* [L$_\odot$]	0.01128 ± 0.00042		
$T_{\rm eff}$ [K]	3415 ± 135		
$\log g$ [from cm.s^{-2}]	4.86 ± 0.13		
[Fe/H] [dex]	-0.46 ± 0.26		
[Mg/H] [dex] ‖	-0.38 ± 0.11		
[Si/H] [dex] ‖	-0.42 ± 0.13		
$v0^\bullet$ [km s^{-1}]	$-5.57851^{+0.00072}_{-0.00069}$	$\mathcal{N}(-5.5791, 0.0035)$	
$A_{RV}^\bullet$ [m s^{-1}]	$2.44^{+0.43}_{-0.36}$	$\mathcal{U}(0, 17)$	
$A_{FWHM}^\bullet$ [m s^{-1}]	$8.6^{+1.2}_{-1.1}$	$\mathcal{U}(0, 43)$	
$P_{\rm rot}^\bullet$ [m s^{-1}]	33^{+43}_{-19}	$\mathcal{J}(5, 520)$	
$\tau_{\rm decay}^\bullet$ [m s^{-1}]	49^{+14}_{-10}	$\mathcal{J}(2.5, 2600) + \tau_{\rm decay} > P_{\rm rot}/2^\dagger$	
$\gamma^\bullet$ [m s^{-1}]	$3.2^{+1.2}_{-1.6}$	$\mathcal{U}(0.05, 5)$	
$u^\bullet_{1,TESS}$	$0.156^{+0.041}_{-0.042}$	$\mathcal{N}(0.147, 0.044)$	
$u^\bullet_{2,TESS}$	$1.593^{+0.040}_{-0.038}$	$\mathcal{N}(1.583, 0.045)$	
$u^\bullet_{3,TESS}$	$-1.617^{+0.033}_{-0.035}$	$\mathcal{N}(-1.627, 0.036)$	
$u^\bullet_{4,TESS}$	$0.542^{+0.015}_{-0.016}$	$\mathcal{N}(0.539, 0.015)$	
Parameters of instruments			

Continued on next page

Table 3 – *Continued from previous page*

	Posterior	Prior	Source
$\Delta RV^{\bullet}_{post/pre}$ [m s^{-1}]	$1.2^{+1.0}_{-1.1}$	$\mathcal{N}(2.88, 4.8)$	
$\Delta RV_{HARPS/pre}{}^{\bullet}$ [m s^{-1}]	$-99.13^{+0.33}_{-0.34}$	$\mathcal{N}(-99.5, 5.0)$	
$\sigma^{\bullet}_{RV,pre}$ [m s^{-1}]	$0.88^{+0.35}_{-0.31}$	$\mathcal{U}(0, 4.5)$	
$\sigma^{\bullet}_{RV,post}$ [m s^{-1}]	$0.91^{+0.73}_{-0.55}$	$\mathcal{U}(0, 3.6)$	
$\sigma^{\bullet}_{RV,harp}$ [m s^{-1}]	< 0.32	$\mathcal{U}(0, 11)$	
$C^{\bullet}_{pre}$ [km s^{-1}]	$4.5136^{+0.0030}_{-0.0028}$	$\mathcal{N}(4.5057, 0.0089)$	
$C^{\bullet}_{post}$ [km s^{-1}]	$4.5135^{+0.0029}_{-0.0028}$	$\mathcal{N}(4.5171, 0.0099)$	
$C^{\bullet}_{HARPS}$ [km s^{-1}]	$3.0573^{+0.0022}_{-0.0022}$	$\mathcal{N}(3.0552, 0.0075)$	
$\sigma^{\bullet}_{FWHM,pre}$ [m s^{-1}]	$5.42^{+1.04}_{-0.95}$	$\mathcal{U}(0, 9.0)$	
$\sigma^{\bullet}_{FWHM,post}$ [m s^{-1}]	< 1.0	$\mathcal{U}(0, 7.2)$	
$\sigma^{\bullet}_{FWHM,HARPS}$ [m s^{-1}]	$4.16^{+0.77}_{-0.68}$	$\mathcal{U}(0, 21)$	
$\sigma^{\bullet}_{TESS}$ [ppm]	< 25	$\mathcal{U}(0, 4200)$	

Notes.
- The values provided in the column "Posterior" have been derived from this work except when specified otherwise in the column "Source". The references for these external sources are : APASS DR9 (Henden et al. 2016), 2MASS (Skrutskie et al. 2006), GAIA-DR2 (Gaia Collaboration et al. 2018), K19 (Kostov et al. 2019), BJ18 (Bailer-Jones et al. 2018).
- The justifications of the choices of *prior*s can be found in Appendix D. These priors have been used for all the analyses performed in Sect 4.1.1, 4.1.2 and 4.2 with only one exception (see ‡ below).
- $\mathcal{U}(vmin, vmax)$ and $\mathcal{J}(vmin, vmax)$ stand for uniform and Jeffreys probability distributions respectively with *vmin* and *vmax* as the minimum and maximum values. JP stands for joint prior (see Appendix D for more details).

• indicates that the parameter is a main or jumping parameter for the MCMC explorations performed in Section 4.1 to 4.2.1.

* For the non-transiting planets, a is computed from a/R_{*}.

† For the prior of τ_{decay}, "$+\tau_{decay}, \tau_{decay} > P_{rot}/2$" indicates an extra condition impose on the prior of this parameter.

‡ The only exception to the fact that the *prior*s used are the ones provided in the column "Prior" of this table is for the ephemerides parameters P and t_{ic} of the three transiting planets in Section 4.1.2. In these cases the *prior*s used are the *posterior*s obtained for these parameters during the analysis of the TESS LC only (see Section 4.1.1). The *prior*s are $P_b = \mathcal{N}(2.2531135, 1.7e-6)$, $t_{ic,b} = \mathcal{N}(1366.17057, 3.3e-4)$, $P_c = \mathcal{N}(3.6906776, 3.0e-6)$, $t_{ic,c} = \mathcal{N}(1367.27357, 2.8e-4)$, $P_d = \mathcal{N}(7.4507272, 7.8e-6)$, $t_{ic,d} = \mathcal{N}(1362.73972, 4.8e-4)$.

§ The parameters reported for the planetary candidate 05 are obtained from the analysis presented in Section 4.1.2. Contrary to the parameters of the other planets which where obtained via the analysis described in Section 4.2.1, they do not include any condition related to dynamical stability.

¶ M_{ref} is the mean anomaly computed at the reference time 1354 BTJD, the time of the first TESS measurement.

‖ As described in Section 3.3, the abundance ratios [Mg/H] and [Si/H] are not directly measured on the observed spectra. They are statistical estimates obtained from a population of stars to which we believe L 98-59 belongs.